ROMA TRE
UNIVERSITÀ DEGLI STUDI

SVILUPPO DI DISPOSITIVI E CIRCUITI ORGANICI REALIZZATI SU SUBSTRATI PLASTICI FLESSIBILI MEDIANTE TECNICHE DI STAMPA

DEVELOPMENT OF ORGANIC DEVICES AND CIRCUITS REALISED ON PLASTIC FLEXIBLE SUBSTRATES WITH PRINTING TECHNIQUES

PhD Student

Sabrina Calvi

Tutors

Prof. Maria Cristina Rossi

Dr. Luigi Mariucci

Index

Chapter 5

Fully printed thin film transistors

Chapter 6

Fully printed p-mos inverters

Abbreviations

A	Hamaker constant of the solvent
A_V	Gain
BGBC	Bottom Gate Bottom Contact
BGTC	Bottom Gate Top Contact
BHF	Buffered hydrofluoric acid
Bo	Bond number
BT	Benzenethiol
Ca	Capillary number
CAD	Computer Assisted Design
C_i	Dielectric capacitance
d	Dielectric thickness
DMSO	Dimethyl sulfoxide
DOS	Density of states
d_{PEN}	Substrate thickness
EA	Electron affinity
E_g	Energy gap
g	Constant of gravitational acceleration
G^*	Complex modulus
G'	Shear storage modulus
G''	Shear loss modulus
g_m	Transconductance
h	Film thickness
HMDS	Hexamethyldisilazane
HOMO	Highest Occupied Molecular Orbital
I	Current
I_{ds}	Drain-source current
I_g	Leakage current
I_{OFF}	Drain-source current in the OFF state
I_{ON}	Drain-source current in the ON state
I_{ON}/I_{OFF}	Current ratio in the ON/OFF states
IPA	Isopropyl alcohol
l	characteristic length
L	Transistor channel length
LUMO	Lowest Unoccupied Molecular Orbital
MIM	Metal-Insulator-Metal
NM	Noise margin
NM_H	Noise margin high
NM_L	Noise margin low
OGI	Organic Gate Insulator
Oh	Ohnesorge number
OLED	Organic Light Emitting Diode
OSC	Organic Semiconductor
OTFT	Organic Thin Film Transistor
OTS	Octadecyltrichlorosilane

P_{disj}	Disjoining pressure
PEN	Polyethylene-naphthalate
PFBT	Pentafluorobenzenethiol
PVDF	Polyvinylidene fluoride
R	Bending radius
R2R	Roll to roll
R_c	Contact resistance
R_{ch}	Channel resistance
R_D	Drive resistance
RIE	Reactive Ion Etching
R_L	Load resistance
R_T	Total resistance
S/D	Source/drain
SAM	Self Assembled Monolayer
SS	Subthreshold slope
t	Time
t_f	Fall time
TGA	Thermo-gravimetric analysis
TGBC	Top Gate Bottom Contact
TGTC	Top Gate Top Contact
TLM	Transfer Line Method
t_r	Rise time
U	Printing speed
US	Ultrasound
V	Voltage
V^*	Characteristic velocity
V_{DD}	Supply voltage
V_{ds}	Source-drain voltage
V_{FB}	Flat-band voltage
V_g	Gate voltage
$V_{g,stress}$	Gate bias applied as a stress
V_{IH}	High input voltage
V_{IL}	Low input voltage
V_{IN}	Input voltage
V_{MAX}	Maximum output voltage
V_{MIN}	Minimum output voltage
V_{OH}	High output voltage
V_{OL}	Low output voltage
V_{on}	Onset voltage
V_{OUT}	Output voltage
VRH	Variable Range Hopping
V_{TH}	Threshold voltage
W	Transistor channel width
We	Weber number
X	Distance of the fluid meniscus at the nip to where the cliché touches the substrate
β	Dispersion parameter
γ [%]	Strain percentage during recovery

γ	Surface tension
$\dot{\gamma}$	Shear rate
δ	Phase angle
ΔV_g	Shift in gate voltage
ΔV_{IN}	Input logic swing
ΔV_{OUT}	Output logic swing
ΔV_{sat}	Value of the shift in gate voltage value in saturation
ε_0	Vacuum permittivity
ε_r	Relative permittivity
ε_s	Strain applied during bending tests
η	Viscosity
Θ_C	Contact angle
λ_s	Wavelength spinodal dewetting instabilities
λ_{ST}	Wavelength Saffman-Taylor instabilities
μ_{lin}	Field effect mobility in the linear regime
μ_{sat}	Field effect mobility in the saturation regime
ρ	Ink density
σ	Shear stress
τ	Relaxation time
τ_{ST}	Characteristic time Saffman-Taylor instabilities
τ_s	Characteristic time spinodal dewetting instabilities
φ	Work function
χ	Ionization potential
ω	Angular velocity

Preface

Nowadays electronics has new requirements: it is expected to be cost-effective, environmentally friendly, disposable, light-weight, unbreakable and possibly biocompatible. Printed organic electronics appears to be a suitable solution to these issues, due to low-cost fabrication and to the possibility to obtain large area multifunctional devices on flexible substrates. Although significant improvements, the potential of organic materials is still not fulfilled due to the lack in high performance optimized ink formulations. Moreover, it is required the development of the existing printing techniques in order to meet the electronics constraints. Among the printing techniques, the gravure printing is promising since it combines high throughput with suitable film thickness and homogeneity, resolution and registration accuracy. Nevertheless, in order to achieve high electronic performance, the solution to some manufacturing issues and a deep understanding of the fluid dynamic mechanisms of the process are required.

During this thesis work, the current knowledge on the gravure printing technique has been applied to improve the printing system and to refine some inks based on organic materials, in particular a conductive and a dielectric one. The study of the characteristics of the materials and the printing system has been focused on the most significant for the realization of efficient transistors and circuits.

The first chapter is an introduction on the organic thin film transistor main features and the characterization method used during this thesis work. At first, the transistor working principle and the main requirements for the organic printed electronics are described. Then, the device characterization methods are explained considering as gold standard transistors and capacitors fabricated with materials deposited by well-established by solution techniques. The procedures to study the stability of the devices, in environmental condition, even when subjected to mechanical stress, light or humidity, are exposed.

In the second and third chapters improvements in the gravure technique and study of the inks are discussed, respectively. The gravure printing system has been investigated to understand its physics. In order to improve the technique, a glass printing cliché has been developed and plastic blades have been used. The suitable ink formulations have been defined through the evaluation of some significant fluid dynamic parameters and the rheological analyses, compared to the printing outcomes. The printing parameters, the wettability differences, the cell shape and pattern have been fitted on the fluid properties.

In the fourth chapter the inkjet printing technique is introduced, as it is an effective method for rapid prototyping and it allows to obtain high resolution patterns. This technique has been used for

the definition of either metallic or organic conductive patterns for the transistor contacts and for the device interconnections in circuits. Moreover, the printing procedure of small area resistors has been optimized. The printing process requirements and optimization are detailed.

Then, fully printed organic thin film transistors and basic circuits have been realized with the printing system and the inks optimized. In the last two chapters the performances of the printed transistors and inverters realised are discussed, based on the data of their electrical characterisation.

The main results and future perspectives of this work are exposed in the Conclusions chapter.

Chapter 1
Introduction

1. Organic electronics

Interest in organic electronics is due to possibility to obtain low-cost, flexible and lightweight devices.[1] The possible applications ranges from smart cards, radio frequency identification tags, active matrix flexible displays, solar cells, smart textiles¸ optoelectronics, near-field communication devices, logic circuits to sensors and electronic interfaces with the biological systems.[2–7] This field continues to progress since the mid-1980s when the first low voltage thin film Organic Light Emitting Diode (OLED) has been demonstrated by Tang and van Slyke, opening the way to the possibility of using organic thin films for a new generation of optoelectronic devices.[8] At now, high efficiency, bright and colourful thin displays based on OLEDs are commercially available yet.[1]

The basic components for building electronic circuits are Organic Thin Film Transistors (OTFTs). Silicon integrated circuits have no size constraints, their costs and performance improve as the size is reduced. On the other hand, for OTFTs the main feature is the possibility to realize large area arrays, so to decrease the cost per unit area, instead of the cost per device. OTFTs cannot compete with the standard silicon electronics for processing power as far as large area is an issue for silicon devices.[9]

Strong efforts have been made to improve the device performance and reliability, both optimizing new materials and processing.[10] Since any change in structure or composition of an organic material can markedly alter its bulk properties, to understand the electronic structure is necessary in order to design high performance devices.[8] The charge carrier transport properties of organic semiconductors (OSCs) have been extensively analysed and many studies are reported in literature, the main features are discussed in the next paragraph.

1.1. Organic semiconductors

The OSC used for OTFTs fabrication can be sorted into highly ordered single crystal and disordered semiconductors. These latter range from the small molecules, compounds with a very well defined molecular weight, such as dendrimers and oligomers (< 20 repeated units), to amorphous polymers, long chain molecules consisting of a number of molecular repeated units > 100.[1,11]

These organic solids are made of molecular subunits, at the molecular level organic semiconductors are hydrocarbon molecules with a backbone of carbon atoms connected by strong bonds. These bonds arise from sp² hybridized atomic orbitals of adjacent carbon atoms, which overlap and yield the bonding and antibonding molecular σ and σ* orbitals. The remaining atomic p_z orbitals overlap to a lesser degree, so that the resulting π-bonding is significantly weaker. They generate the π and π* orbitals, which are involved in the electronic excitations of conjugated molecules.[12,13]

Depending on the material degree of order, the charge carrier transport mechanism in organic semiconductors can fall between two extreme cases: band or hopping transport (Fig. 1).
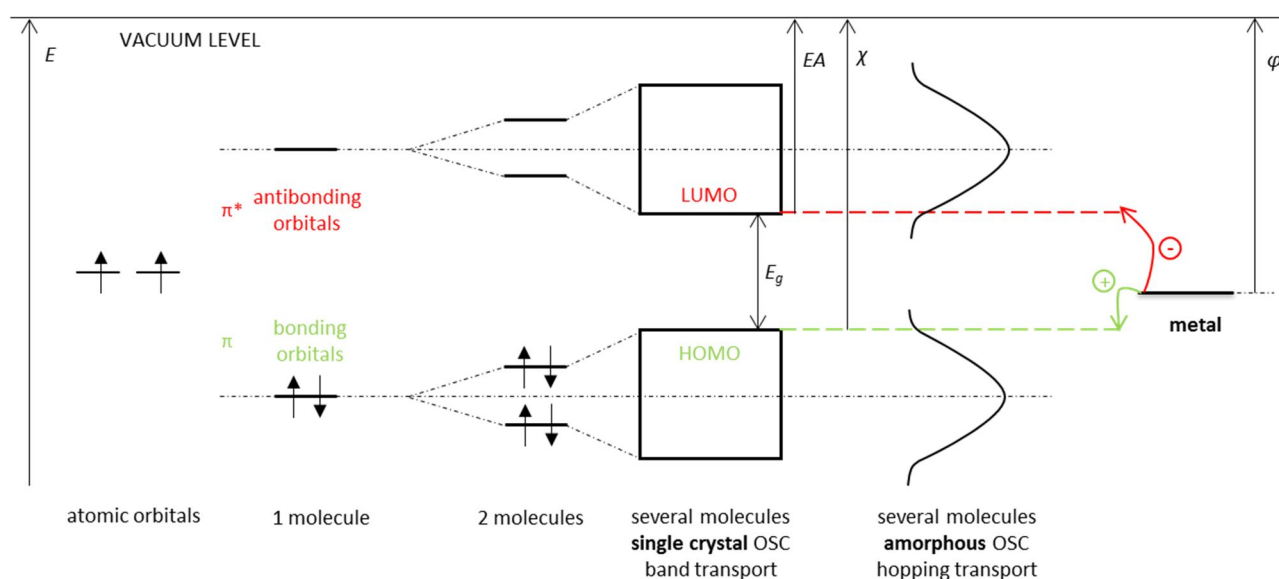

Fig. 1 Transport mechanism for organic semiconductors and the carrier injection mechanism from a metal electrode. *E*= energy, *χ* = ionization potential, *EA* = electron affinity, *E_g* = energy gap.

In single crystal semiconductors, atoms in the regular crystal structure interact creating allowed and forbidden energy levels for their electrons. Due to the crystalline ordering, these levels are shared over the whole crystal and for all charge carriers, hence they are referred to as *extended states*.[14] The electronic structure can be described by using the **band theory**. The energy levels in the material are grouped in bands, separated by energy gaps. In the ground state of the molecule, all bonding orbitals up to the Highest Occupied Molecular Orbital (HOMO) are filled with two electrons of antiparallel spin, from the Lowest Unoccupied Molecular Orbital (LUMO) onwards the antibonding orbitals are empty.[13] Since the block of filled orbitals ends with the HOMO and the sequence of unfilled ones starts with the LUMO, they are also called the frontier orbitals.

For charge transport to occur, there must be a charge on the molecular unit, which may either be an additional electron accommodated into the LUMO or a hole in the HOMO, which corresponds to taking an electron out. The molecule is then no longer in the ground state but rather in a charged

excited state. The addition or removal of an electron from the molecule may be obtained through injection or extraction of an electron at the interface between a metal electrode and the molecule due to an applied electrical field, as is typically the case in the operation of a device such as the OTFT.[11,13] The energy to remove an electron from a neutral molecule, thus creating a molecular cation, is the ionization potential (χ), while the electron affinity (*EA*) indicates the energy gained when placing an electron onto a neutral molecule, thus creating a molecular anion.

As a characteristic feature of band transport, the mobility increases while lowering the temperature following a power law.[12]

With increasing material disorder, the concept of bands separated by an energy gap is no more valid, since different phenomena have to be taken into account.[12,14] In polymeric OSCs the molecular disorder completely impedes the generation of globally shared energy levels, and charge carriers can only occupy physically *localized states*.[14] The charge transport mechanism is described by the Variable Range Hopping (**VRH**) model, at low temperatures. Due to an electric field or a charge carrier gradient, the charge carriers trapped in localized states tend to drift or diffuse to another site. Due to the energetic and structural disorder of the material, this jump is hindered by an energy barrier, which can be overcome with the assistance of thermal energy. Therefore, the hopping transport can be described as a thermally activated, or phonon assisted, tunnelling mechanism from an occupied localized state to an empty one.

According to VRH, the probability of a hop event mainly depends on the phonon frequency, the difference in energy between the initial and final state, the spatial separation between the states and the free carrier wavefunction.[14] In disordered organic solids the Density Of States (DOS, the number of states for volume unit and energy unit) follows a Gaussian distribution.[12,14] Its width is determined by the spatial and energetic disorder within the semiconductor, the broader is the lower are the mobilities and the stronger is the temperature dependence.[10] Most models assume an exponential distribution of localized states, which is the approximation of the tails of the Gaussian bell. At low carrier concentration, this is a reasonable approximation.[10,12,14]

Depending on the model different temperature dependencies for the mobility have been suggested, but mostly the mobility increases with the temperature growth and it also depends on the applied electric field.[12]

Furthermore, the trapping effects as well as the charge carrier injection mechanism itself have to be considered to describe electrical transport in organic solids.[12] All these factors need to be taken

into account when evaluating the conductivity of the semiconductor and the static currents in OTFTs.[14]

In literature high performance have been reported for small molecule materials, however they require to achieve high ordering, in particular at the interface with the dielectric. This requirements is difficult to achieve, particularly to ensure the same high performances on large areas using a printing deposition method.[15] Circuit design becomes more complicate with large variations among device performances. Hence, OTFTs for printed organic circuits are strictly required to have high carrier mobility and to have minimal variations in their electrical performances.[6]

Conjugated polymers have shown lower mobility compared to small molecules materials, but they ensure large area uniformity, with low device to device performance variations.[6,15] Moreover, they allow to control the rheological properties of the solutions and to use the proper orthogonal solvent, offering good mechanical properties.[7] The backbone of a semiconducting polymer is formed by a chain of carbon atoms with alternating single and double bonds, aromatic and heteroaromatic rings may also be part of this structure. The large majority of the OSC polymers contain side chains that not only make them soluble in common organic solvents, but also they keep polymer chains at a certain distance from each other once they are deposited in a film, and sometimes they even control the relative orientation of polymer chains to each other. Hence, modifications to the side chains enable to control the degree of electronic interchain interaction, which determine the mobility of charge carriers in OTFTs.[11] These features have moved the choice of a semiconductor on the polymeric materials.

At last, to obtain a functional device, not only the OSC has to be a material with enhanced regularity and purity, but also its potential has to be exploited optimizing the processing and the device design.[16]

1.2. Printed organic electronics

The peculiar features of the organic materials, whether they are semiconductors, dielectrics or conductors, result from their weak intermolecular bonds, in the order of $10^{-3} \div 10^{-2}$ eV compared to $2 \div 4$ eV of a strong covalent bond. As already introduced for the OSCs, it is possible to modify them chemically during the synthesis, in order to change their physical characteristics, as the hydrophilicity, the viscosity and the mechanical and electrical properties.[2,8,17] Moreover, these molecules are highly soluble in common solvents, so enabling the deposition by solution techniques.[2,8,17] These properties make them suitable for low temperature processes and for

developing inks with the suitable requirements for different deposition techniques. Hence, these materials can be considered as the most suitable for the development of low cost flexible electronics on plastic substrates.[8,17–20] They appear to be a solution towards the new requirements for electronics, which is expected to be cost-effective, environmentally friendly, disposable, light-weight, unbreakable and possibly biocompatible.[7] Although the confirmed improvements, the potential of these materials is still not realized as the processing to realize high performance and reliable electronic devices remains challenging.[16]

The most efficient way to pattern functional materials is depositing the material with an additive process. It allows to avoid material waste, the damage of the previous deposited layers, an easier deposition of different materials on the same level avoiding their deterioration. It eliminates some of the cost drivers in the Si-based electronics, such as the high-vacuum deposition equipment, the subtractive processes, the photolithography.[7] So, it results in a simplified process and in a reduction of the costs.[21,22] In particular, printing techniques have been considered promising for organic electronic device realization. They allow to combine large area low cost production with the possibility to achieve suitable resolutions.[17,20–23] Moreover, they are compatible with the low temperature required.[22] Printed layers have to respect several **requirements**:

- *uniform morphology* over large area;
- *thickness* compatible with the application and constant over the sample;
- *resolution* high enough to achieve interesting operating frequencies;
- *registration accuracy*, defined as the precision in the placement of the printed area;
- high *throughput*.[6]

Printing technologies can be classified using various criteria, as a function of the requirement considered. The system can be in contact or non-contact, depending if the substrate is in contact with the patterned structures with inked surfaces or if the solution is dispensed through openings or nozzles. If they use a master, it can be flat or allow roll-to-roll (R2R) compatibility, so the substrate is enrolled forming a web re-reeled after the process and the master is a patterned roll. The technique can be scalable, so able to be used over a wide range of different substrate and patterning areas to translate a small scale process to manufacturing. The printing speed is strictly correlated to the achievable throughput. Moreover, each technique has its limitation in resolution, registration accuracy, film thickness achievable and suitable ink characteristics. In Tab. 1 are summarized in detail the characteristics of the main printing processes used for electronic devices realization.[7,21,22]

Technique / Parameter	Offset	Gravure	Flexography	Screen	Inkjet
Lateral resolution (μm)	10-50	7.5	6	30	20-50
Registration (μm)	> 10	> 20	< 200	> 25	5-20
Film Thickness (μm)	0.6-2.5	0.02-12	0.04-8	0.015-100	0.01-20
Ink viscosity (mPa·s)	20000-10000	50-200	50-500	500-50000	< 20
Contact Use of master	Yes	Yes	Yes	Yes	No
R2R compatible	Yes	Yes	Yes	Yes	Intermediate
Printing speed (m/min)	15	100	180	100	5
Throughput (m^2/s)	30	60	30	<10	0.5

Tab. 1 Characteristics of the main printing techniques for electronics.[7,21,22]

The *non-contact mode* techniques provide good compatibility with organic electronics. The most used non-contact technique is the inkjet printing, a drop on demand system that allows easy prototyping and high resolution. A microprocessor, intended for RFID tag applications, integrating thousands of transistors in a hybrid technology combining organic p-type and inorganic n-type transistors has been yet demonstrated.[24] On the other hand, feature size is limited to around 20 μm and the technique suffers from the coffee ring effect, so making difficult to obtain a homogeneous morphology in micro-sized features. Moreover, it allows to achieve a low throughput.[25] Further details on this technique will be discussed in Chapter 4.
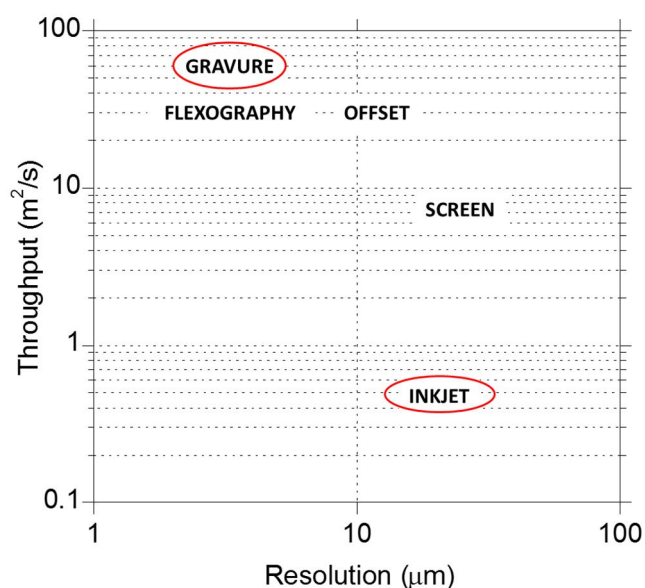

Fig. 2 Throughput vs resolution of the main printing systems for electronics.

The highest throughput is achievable by using *R2R printing techniques* and great interest has grown around them as resolutions scaled below 10 µm.[17,26,27] Among these printing systems, as schematized in Fig. 2, the gravure seems to be the most suitable, allowing to obtain highly defined and homogeneous layers in the thickness range of interest, from tens of nanometres to several microns.[17,18,23,28,29] Further details on this technique will be discussed in Chapter 2.

At the state of the art, fully printed electronics falls into the kHz regime. Thanks to the high pattern fidelity even in defining channel lengths down to 2 µm, it has been possible to obtain fully printed transistors with operating frequencies in the MHz range.[2,20,25,30–32] Polymeric complementary circuits stable in ambient conditions are currently difficult to realize since, despite high performance p-channel polymers, the achievement of good n-channel polymers is still lacking. Recently, it has been reported a highly soluble and printable n-channel polymer exhibiting electron mobilities up to $0.45 \div 0.85$ $cm^2 V^{-1} s^{-1}$ in ambient conditions. Several OTFTs on plastic substrates have been presented, the S/D contacts were in gold, the semiconductor and polymeric dielectric layers have been deposited by spin-coating or printed by gravure, flexographic and inkjet techniques. Hence, all printed polymeric complementary inverters with gain $25 \div 65$ have been demonstrated.[18] Complementary inverters and five-stage ring oscillators fully gravure printed have been realized using organic electrodes. The p- and n-channel transistors are well balanced, with mobility around $2.9 \cdot 10^{-3}$ and $3.9 \cdot 10^{-3}$ $cm^2 V^{-1} s^{-1}$, turn-on voltage around -1 and -1.5 V, respectively. The fully printed ring were able to work until 220 Hz.[27]

Although many progresses have been already demonstrated, the gravure printing technique itself still has some limitations and the efficiency of the printed devices is still not enough as required for high performance electronics.

2. Organic Thin Film Transistors

2.1. Configurations and working principle

An organic field effect transistor is made of two electrodes called source and drain, separated by a distance *L* (channel length) and of width *W* (channel width), in contact with a semiconducting layer. This layer is separated from the gate electrode by an insulating layer, the gate dielectric. The devices can have different structures, as described in Fig. 3, depending on the materials and deposition techniques used. As the preferred structure for this thesis work has been the staggered top gate, usually the consideration will be referred to this configuration.[10]
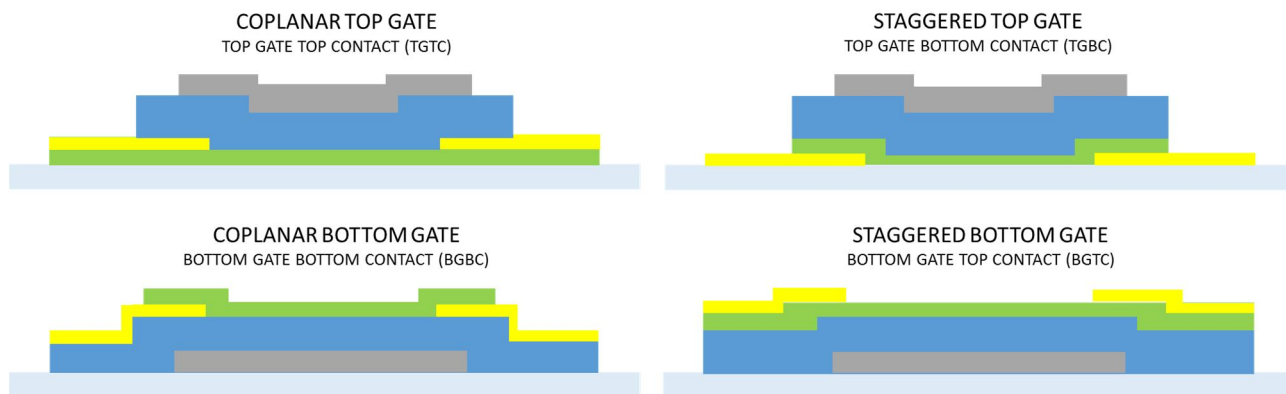
Fig. 3 OTFT configurations: light blue: substrate – blue: dielectric – green: semiconductor – yellow: source and drain contacts – grey: gate contact.

A voltage is applied to the drain and gate electrodes, the source is grounded. The potential difference between the source and the gate is called gate voltage V_g, while the one between the source and the drain is the source-drain voltage V_{ds}.[10] The charges are injected in the semiconductor from the source electrode. The transistor is in the OFF-state when in the channel no mobile charges are present, otherwise it is in the ON-state, when the carriers are accumulated in the transistor channel, hence the device operate in accumulation mode.[10,14,33,34] For n-channel transistors the electrons have to be injected in the LUMO level of the semiconductor, while the holes in the p-channel devices in the HOMO level.[10] Whether electron or hole injection can occur depends on the relative HOMO and LUMO energy of the molecule in a solid film compared to the work function (φ) of the electrode.[11] The interface between the semiconductor and the source is usually treated as a Mott-Schottky barrier, whose height is given at first approximation by the difference between the electrode φ and the semiconductor HOMO or LUMO level. A good *ohmic contact* is expected for low barrier, while poor charge injection occurs if the φ and the OSC molecular orbital are not close enough. Non-ohmic contacts introduce a resistance to the current flow between source and drain, the contact resistance R_c; further details will be given in Paragraph 3.2.1.[10]

The either positive or negative applied gate voltage induces an accumulation of charges of the opposite sign, electrons or holes respectively, at the interface between the semiconductor and the dielectric layers.[10] The number of accumulated charges is proportional to V_g and the capacitance C_i of the dielectric, but not all the induced charges are mobile and contribute to generate the current, I_{ds}, between source and drain electrodes of the transistor. Hence, the voltage at which the charges induced are mobile is not $V_g = 0$, but at a defined threshold voltage V_{TH}. This condition is due to different effects. A mismatch between the work function in the electrode and the HOMO/LUMO level in the OSC generate a dipole and a band-bending in the semiconductor. To achieve the flat-band condition the application of a gate voltage equal to a value named V_{FB} is required, shifting the V_{TH}. Deep traps

have to be filled before the channel can conduct. The gate voltage that has to be applied to have mobile charges is higher than $|V_{TH}|$ and thus, the effective gate voltage is $|V_g - V_{TH}|$. Donor, for n-channel, or acceptor, for p-channel, defect states, usually induced by impurities or defects in the OSC, or interface dipoles can cause accumulation of charges in the channel when $V_g = 0$. The gate has to be biased oppositely to turn the channel off.[10,33]

When a V_{ds} is not applied, the charge carrier concentration in the transistor channel is uniform. A linear gradient of charge density from the source forms when it is applied a small $|V_{ds}| \ll |V_g - V_{TH}|$. This is the linear regime, the potential in the channel increases linearly from 0 at the source to V_{ds} at the drain. Increasing $|V_{ds}|$, when $V_{ds} = V_g - V_{TH}$ the channel is *pinched-off*. A depletion region is generated near the drain, since the difference between the local potential and the gate voltage is below the V_{TH}. The transistor now operates in the saturation regime. Even if voltage applied at the drain is increased, the potential at the pinch-off point at the drain remains at $|V_g - V_{TH}|$ and so the potential drop with the source remains approximately constant. The current which can flow across the depletion zone does not further increase and saturates at $I_{ds,sat}$, but the depletion region is expanded shortening the channel.[10]

2.2. Fabrication procedure by solution techniques

In the next paragraphs the main OTFT electrical features and the characterization methods used during this thesis work will be explained. As gold standard it will be considered the p-type OTFT fabricated with materials deposited by solution techniques and defined by optical lithography.

A common fabrication procedure, used for the realization of these devices, is schematized in Fig. 4 and detailed hereafter. The devices realised with this process are well comparable to the state of the art.[7,33,34]
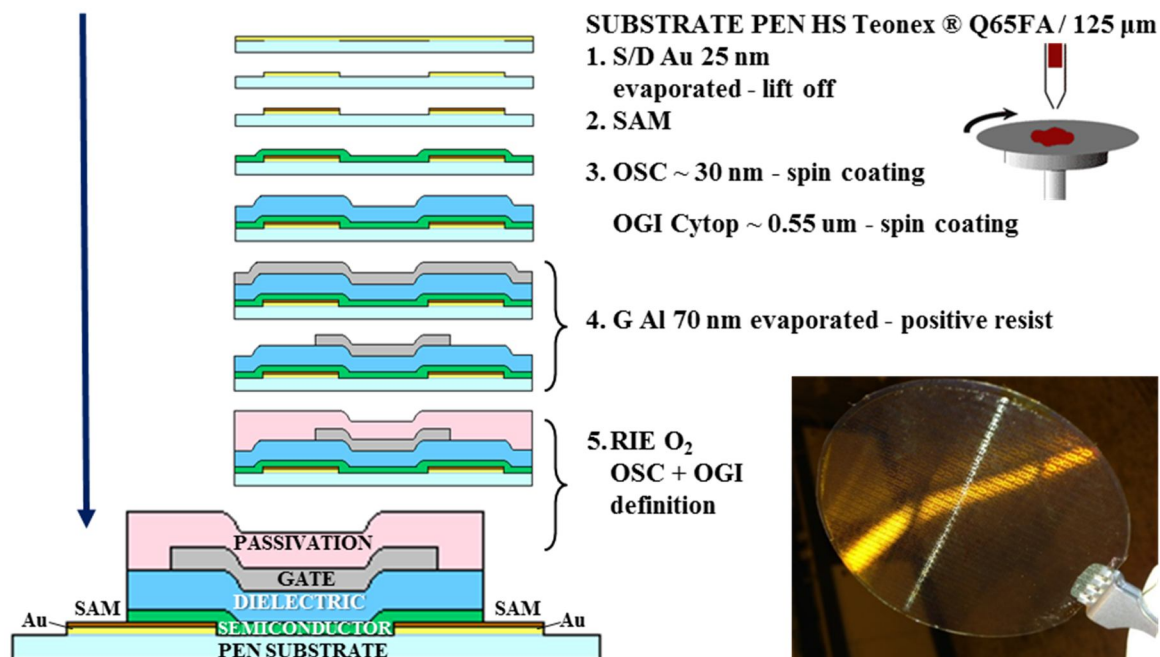
Fig. 4 Scheme of the fabrication procedure of OTFTs by solution techniques.

1. The S/D contacts are in gold 25 nm thick, they have been deposited by thermal evaporation and patterned by optical lithography. To obtain the most efficient interface with the OSC, the lift-off technique has been used to pattern the contacts, using an inverted resist (AZ 5214, as developer AZ 400 K diluted 4:1 in deionized water, both from AZ Electronic Materials (Germany) GmbH).

2. A Self-Assembled Monolayer can be deposited by spin coating before the semiconductor deposition in order to improve the structural properties of organic layer and the carrier injection from the electrodes.[35,36] The concentration used has been 10 mM diluted in isopropyl alcohol (IPA, J.T. Baker, MOS grade).

3. The active and dielectric layers have been deposited by spin-coating technique, using a co-rotating and an open spinner, respectively (Fig. 5).
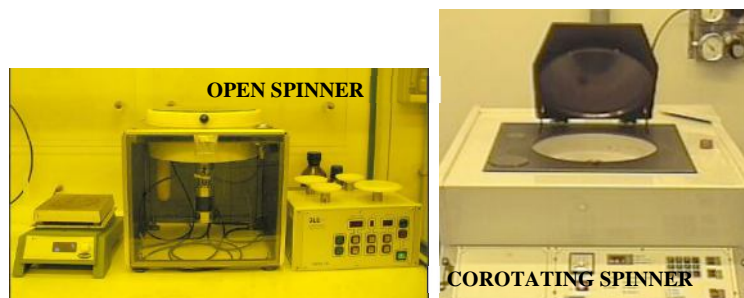

Fig. 5 Instrumentation for spin-coating deposition.

4. The gate contact is in aluminium, thermal evaporated and patterned by photolithography. The metal is wet etched using the formulation H_3PO_4:CH_3COOH: HNO_3:H_2O 4:4:1:1 (respectively: phosforic acid 85-87% and glacial acetic acid; nitric acid, 70% all from J.T.Baker CMOS grade; deionized water).

5. At last, the OSC and the dielectric have been patterned by optical lithography, leaving the photoresist to act as a final passivation layer (Microposit™ S1813™ G2, as developer Microposit™ MF-319, both by DOW®). The etching has been conducted via a physical method, using the Reactive Ion Etching (RIE) system (Fig. 6), with the following receipt:

- 90% O_2 (64.8 sccm)

- 57 W

- bias under 200 V

- pressure ~ 50 mTorr

In a real circuit, leakage can take place also between nearby transistors. Hence, the semiconductor has to be patterned and sized around the gate, to avoid fringe currents.[14]

Fig. 6 Reactive Ion Etching system.

As substrate has been chosen a heat-stabilized, low roughness polyethylene-naphthalate (PEN) foil 125 μm thick, Teonex® Q65FA provided by DuPont. The devices have been realized on the non treated surface. The substrate has been cleaned in ultrasound (US) bath, Ultrasonic® Compact Euromedica s.n.c. with acetone 2 min and IPA 3 min. All curing temperatures have been kept below 100°C to avoid any substrate shrinkage.

Several semiconductors have been tested, in particular data will be reported in this chapter for a small molecule p-type organic semiconductor, SmartKem® p-FLEX™ (supplied by SmartKem Ltd, ≈ 30 nm thick), used as gold standard. In Chapter 4 data for a polymeric n-type organic semiconductor

N2200 (supplied by Polyera, $\approx$ 40 nm thick) will be reported to be compared with the ones obtained with the printed devices. The SAM used have been pentafluorobenzenethiol (PFBT, Sigma-Aldrich) and benzenethiol (BT, Sigma-Aldrich), respectively for the p- and n-type OSC.

The dielectric is a fluoropolymer based material named Cytop™, purchased by AGC Chemicals, used diluted 3:1 in its solvent, CT-Solv180, to achieve a thickness around 550 nm.

The OTFT channel length L ranges from 2 to 100 μm and their channel width W can be 50, 100 or 200 μm.

All fabrication processes have been carried out in a clean room environment (Fig. 7).

Fig. 7 Photolithography setup.

3. Organic Thin Film Transistor characterization

To characterize the deposited materials, the layer morphology has been verified and the film thicknesses have been measured as described in Paragraph 3.1.

The OTFTs are characterized electrically to test their performances following the procedure explained in Paragraph 3.2. To verify their reliability the devices are subjected to different stresses, as described in Paragraph 3.3-3.4-3.5. As known from literature, OTFTs are sensitive to different stresses showing significant changes in their performances. OTFTs have shown instabilities during operation in air conditions or when they are subjected to high biases.[37,38] Organic materials are sensitive to ambient environment, it has been shown that oxygen and water diffusion into the active layer or the exposure to light induce device performance degradation so reducing devices reliability.[1,25,37,39] Moreover, to achieve efficient flexible electronics, the devices have to be stable when subjected to mechanical strain.[9]

3.1. Film characterization

The surface morphology of each deposited films and the full device have been analysed through optical microscopy in bright field with reflected light (Fig. 8 B). The devices have been also observed with transmitted light to measure more precisely the dimensions and to verify the metal layer continuity (Fig. 8 C). The microscope is an Olympus MX50 equipped with a digital camera (Fig. 8 A).
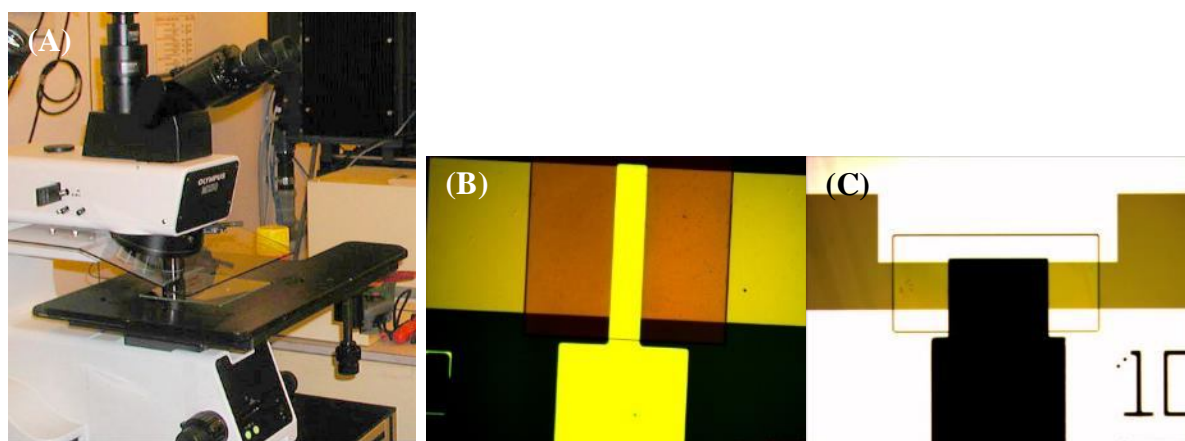

Fig. 8 (A) Optical microscope. (B) OTFT image in reflection. (C) OTFT image in transmission.

The film thicknesses and roughness have been measured through a contact profilometer (Fig. 9, Alpha-Step 500 KLA Tencor), with a low stylus tracking force around 1 mg to avoid material damaging. This method allows to avoid artefacts due to surface reflectance or colours, as characteristic for the optical techniques.

Fig. 9 Profilometer.

3.2. Electrical characterization

Organic thin film transistors are electrically characterized through current-voltage (I-V) characteristics, called the transfer and the output curves,. Electrical characterization has been

performed using a Suss PM5HF Analytical Probe Station (Fig. 10) equipped with a Hewlett Packard HP 4145B semiconductor parameter analyser.
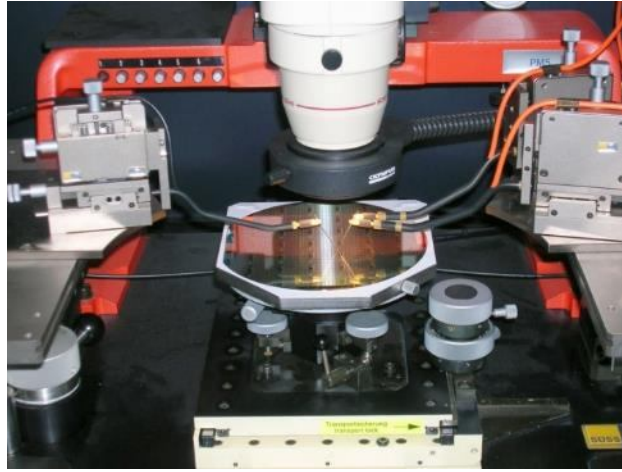

Fig. 10 Suss PM5HF Analytical Probe Station.

The **transfer characteristics** (Fig. 11) are obtained keeping a constant V_{ds} and measuring the I_{ds} at different V_g, the main OTFT parameters can be calculated from these curves.
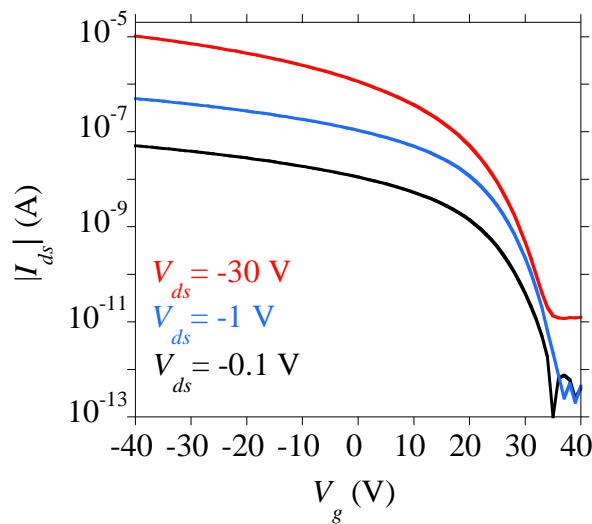

Fig. 11 Transfer characteristics of a staggered OTFT. $L = 100$ μm, $W = 145$ μm.

The main figure of merit for an OTFT is the **field effect mobility**. For $|V_{ds}| << |V_g - V_{TH}|$ is valid the assumption that the charge distribution within the channel is dominated by the field created by V_g and not by the lateral field due to the I_{ds}, the *gradual channel approximation*. In this condition and neglecting diffusion, assuming that the mobility is independent from the carrier density and hence from V_g, the current-voltage characteristics of the device can be described analytically as follows.[10]

The I_{ds} is mainly dependent on the OTFT channel dimensions, the width W and the length L, the field effect mobility μ, the dielectric capacitance C_i, the effective gate voltage $|V_g - V_{TH}|$ and the V_{ds}, as in:

$$I_{ds} = \frac{W}{L} \mu C_i \left[\left(V_g - V_{TH} \right) V_{ds} - \frac{1}{2} V_{ds}^2 \right]$$

Eq. 1

where

$$C_i = \frac{\varepsilon_0 \varepsilon_r}{d}$$

Eq. 2

is the dielectric capacitance per unit area, with $\varepsilon_0 \approx 8.854 \cdot 10^{-12}$ F/m is the vacuum permittivity, ε_r the relative permittivity, d the thickness, thus it represents the amount of charges induced for an applied V_g.

In *linear regime* $|V_{ds}| << |V_g - V_{TH}|$, the term V_{ds}^2 can be dropped, obtaining

$$I_{ds} = \frac{W}{L} \mu_{lin} C_i \left(V_g - V_{TH} \right) V_{ds}$$

Eq. 3

The field effect mobility in the linear regime μ_{lin} can be calculated from the gradient of I_{ds} versus the V_g at a constant V_{ds}, the transconductance $g_m = \left. \frac{\partial I_{ds}}{\partial V_g} \right|_{V_{ds=constant}}$, as defined in the following equation:

$$\mu_{lin} = \left| g_m \right|_{max} \frac{L}{W C_i |V_{ds}|}$$

Eq. 4

This value is generally lower than the effective mobility, since the electric field dependence is neglected and so the dependence on V_g.[10,40]

In the *saturation regime* the Eq. 3 is no more valid, considering negligible the channel shortening due to the depletion region at the drain, the $I_{ds,sat}$ can be obtained from Eq. 1 since $V_{ds} = V_g - V_{TH}$, obtaining:

$$I_{ds,sat} = \frac{W}{2L} \mu_{sat} C_i \left(V_g - V_{TH} \right)^2$$

Eq. 5

In this regime, assuming that mobility is independent from V_g, the field effect saturation mobility μ_{sat} can be calculated as

$$\mu_{sat} = 2 \left(\left. \frac{\partial \sqrt{|I_{ds,sat}|}}{\partial V_g} \right|_{max} \right)^2 \frac{L}{W C_i}$$

Eq. 6

The p-channel devices obtained by solution techniques can be considered at the state of the art, as they show $\mu_{lin} \approx 2 \div 3$ cm^{2}V^{-1}s^{-1} and $\mu_{sat} \approx 1 \div 2$ cm^{2}V^{-1}s^{-1}.

Another important parameter is the **threshold voltage** V_{TH}. In Fig. 12 the calculation method adopted is shown for the linear regime. The V_{TH} value can be extracted from the linear fit to zero of

the transfer curve in a linear scale plot, for the linear regime considering the I_{ds}, while for the saturation regime the $I_{ds,sat}^{1/2}$. The intercept in the linear region can be defined considering the maximum of the g_m.[10,33] The threshold voltage can depend on several effects, such as the impurities, interface states, charge traps independently on its causes, but as deduced from Eq. 6 it can be reduced increasing the C_i in order to induce more charges at lower applied voltages.[10]
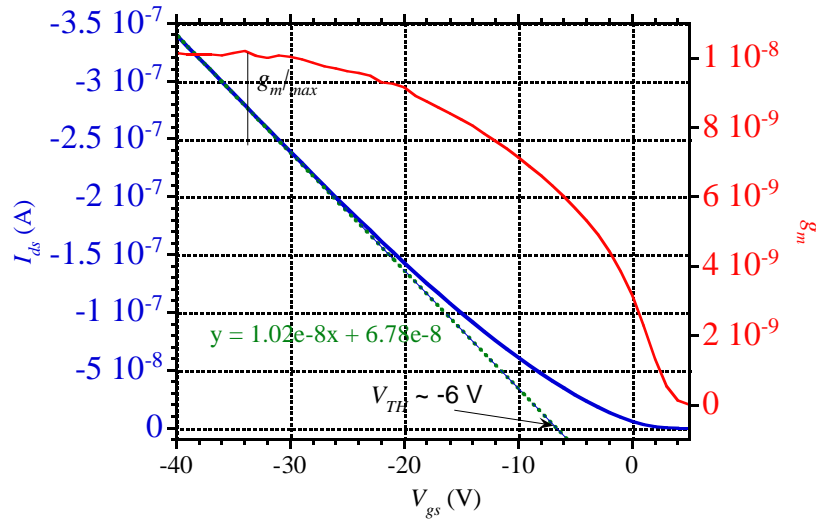

Fig. 12 V_{TH} **calculation method for the linear regime.** $L = 100$ **µm,** $W = 145$ **µm.**

From the transfer characteristics in linear regime on a semilog plot, it is possible to extract the voltage at which the I_{ds} increases above a defined low I_{OFF}, because of the beginning of charge accumulation in the channel, the **onset voltage** V_{on}.[10] More precisely, it can be defined as the maximum value of the second derivative of log (I_{ds}) with respect to V_g as settled in Eq. 6 and reported in Fig. 13.

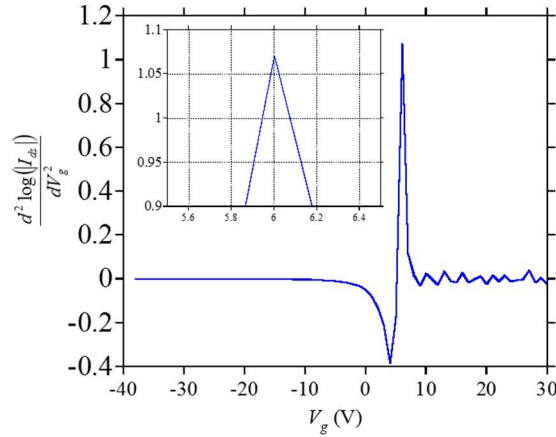$$V_{on} = \left. \frac{d^2 \log(|I_{ds}|)}{dV_g^2} \right|_{max}$$

Eq. 7

Fig. 13 V_{on} **calculation, it results to be $\approx$ 6 V. L = 100 µm, W = 145 µm.**

A measure of how quickly the device switches from the OFF to the ON state is the **Subthreshold Swing**, which is the inverse of the subthreshold slope extracted as the maximum slope of the quasi-linear part of the subthreshold current, for V_g between V_{on} and V_{TH}:

$$SS = \frac{1}{\left| \dfrac{d \log(|I_{ds}|)}{dV_g} \right|_{max}}$$

Eq. 8

It is typically reported in mV/decade and mainly depends on the dielectric capacitance and on the trap states at the interface and inside the semiconductor.[10,33] In practice, it has been considered a $I_{ds} > 2e\text{-}11$ to avoid artefacts due to the I_{OFF} variations (Fig. 14).
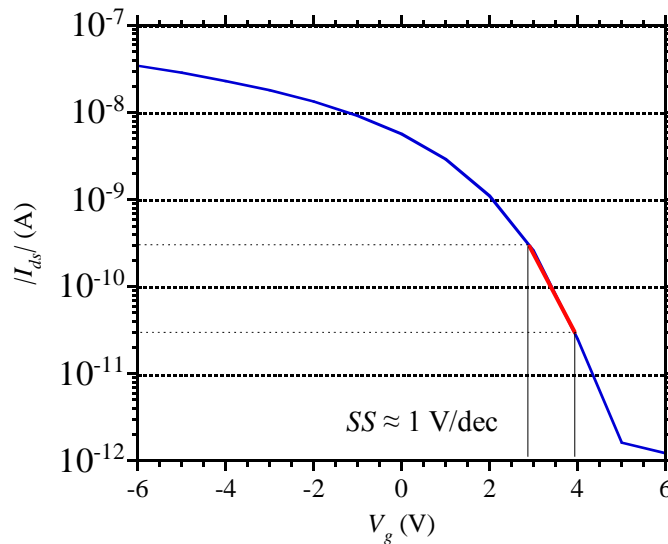
Fig. 14 Calculation method for the *SS*. L = 100 µm, W = 145 µm.

Another significant parameter is the **ON/OFF ratio**, I_{ON}/I_{OFF}, which is the ratio of the highest I_{ds} in the ON-state and the lowest in the OFF-state at low $|V_{ds}|$. It is typically reported as 10^x (Fig.

15).[10,33] This value should be as higher as possible to allow a clean switch of the transistor. The I_{ON} mainly depends on the OSC mobility, the dielectric capacitance and the contact resistance effects at the source/drain (S/D) contacts, while the I_{OFF} is due to the gate leakage, the conduction at the substrate interface and the bulk conductivity of the semiconductor.[10]
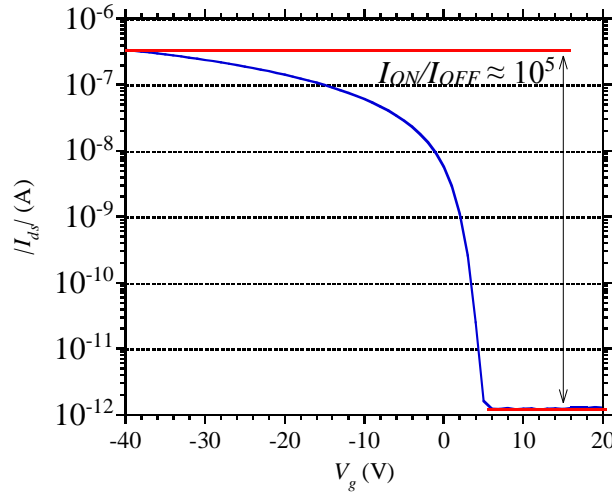

Fig. 15 I_{ON}/I_{OFF} calculation. $L = 100$ µm, $W = 145$ µm.

Both I_{ON}/I_{OFF} and SS depend on the device geometry, the operating conditions and the current detection levels of the measurement system.[33]

The **output characteristics** (Fig. 16) show the I_{ds} versus the V_{ds} obtained keeping constant the V_g. From these characteristics, it is highlighted the linear regime at low V_{ds}, in which the current flowing through the channel is directly proportional to V_{ds}, and the saturation regime at high V_{ds}, with the current saturated at $I_{ds,sat}$.[10]
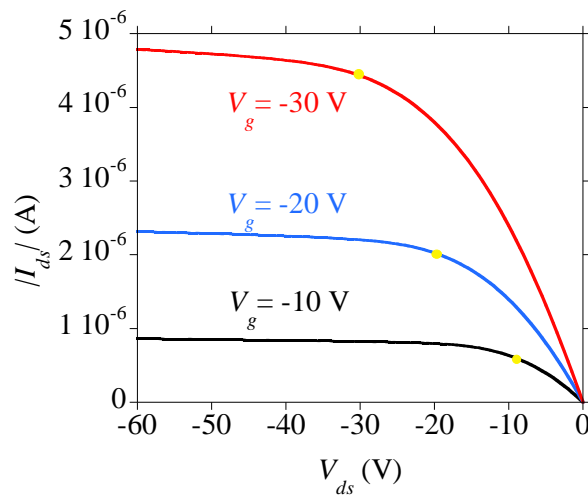

Fig. 16 Output characteristics of a staggered OTFTs, the yellow dots indicate the condition $V_{ds} = V_g - V_{TH}$. $L = 100$ µm, $W = 145$ µm.

High non-ohmic contact resistance is typically found observing the output characteristic, at low V_{ds}. In this case, the current increase in the linear region is suppressed and then the characteristics follows a superlinear trend.[10] Further details will be given in the next Paragraph.

3.2.1. Contact effects

As explained before, the first attempt to evaluate the contact resistance expected from an electrode/semiconductor couple is to compare the difference between the electrode φ and the semiconductor HOMO or LUMO level. Often the interface has an additional dipole barrier that changes the interface barrier height varying the electrode φ.[10,15]

The introduction of Self Assembled Monolayers (SAM) functionalizations is useful to change the electrode φ to improve charge injection in the semiconductor.[10,35,41]

The transistor structure, in particular the position of the S/D electrodes to the gate electrode, influences the R_c. In staggered configuration the S/D overlap the gate so charges are injected over a larger area than the coplanar geometry, reducing the contact resistance. The use of bottom contacts allows the use of SAM, while depositing the contacts on the OSC could introduce surface states and modify the charge injection.[10]

The contact resistance can be measured with the Transfer Line Method (**TLM**), by determining the resistance of transistors with different channel lengths. It is assumed that the parasitic resistance is not dependent on the channel length and the gate voltage. For small drain voltages, the total resistance can be assumed as the sum of the contact resistance, R_c, and the channel resistance, R_{ch}, as follows:

$$R_T = R_c + R_{ch}$$ **Eq. 9**

$$R_{ch} = \frac{L}{WC_i\left(V_g - V_{TH}\right)\mu}$$ **Eq. 10**

The contact resistance, due to both source and drain, can be extracted from the curve of the R_T as a function of L by extrapolating to zero channel length.
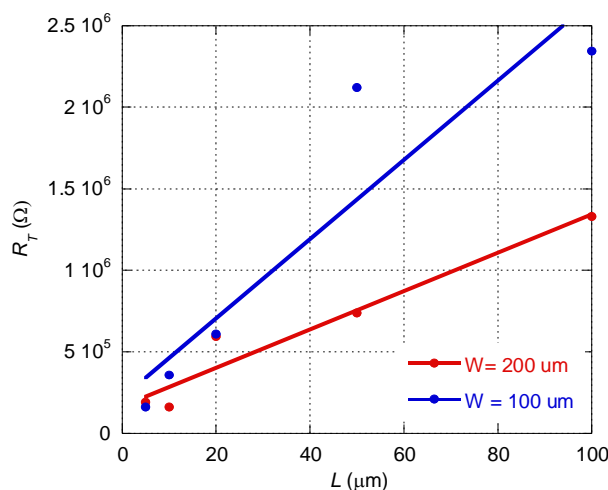
Fig. 17 Total resistance as a function of the channel length for two different channel width.

In Fig. 17 the calculations for two different channel widths are reported. The R_c results to be around 2.75 kΩcm. Since the method requires to use different transistors for the measurements, the resistances can vary from one device to another. Data are not strictly aligned in the graph due to this issue.[15]

3.3. Stability under bias stress

When a transistor operate for an extended time, V_{TH} tends to change. This shift is due to the trapping (de-trapping) of the mobile accumulated charge into immobile trapping states. As a consequence, the OTFT current varies with time. The presence of impurities greatly affects the rate of change of the V_{TH} shift.[9,10] The bias stress behaviour of a transistor has significant effects on the stability in time and the applicability of the transistor in circuits.[10] Fast and reversible shift of the threshold voltage with time also causes hysteresis in the I-V measurements. In this case the forward and reverse scan are not matching.[10]

For bias reliability tests a HP 4145B semiconductor parameter analyser Hewlett Packard has been used.
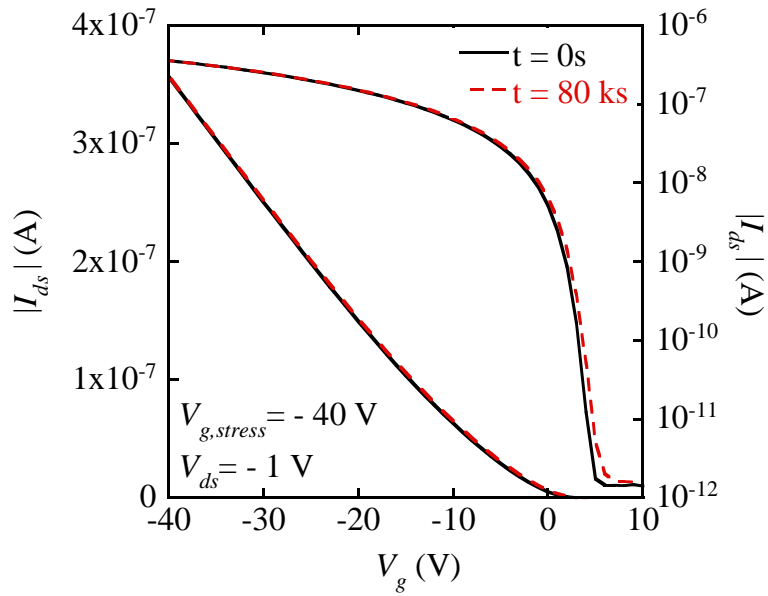
Fig. 18 OTFTs characteristics stress in V_g for an OTFT with $L = 100$ µm, $W = 145$ µm, air and room temperature conditions.

In Fig. 18 are shown the transfer characteristics, measured in air and in dark, before and after the application of 80000 s stress at $V_g = -40$ V. The device shows excellent stability, as the curves are overlying and neither the V_{TH} nor the mobility have shown significant variations. It can be concluded the devices have not shown holes trapping in the dielectric or in the OSC due to the bias stress.

3.4. Sensitivity to light

Light soaking effects on the devices have been investigated keeping them in a probe station under light for a certain time and measuring their transfer characteristics periodically.

These measurements have been carried out by using a HP 4145B semiconductor parameter analyser Hewlett Packard. As light source, a white led light has been used with two different light intensities, high or low (around 20000 or 100 lux). The measurement setup is reported in Fig. 19.
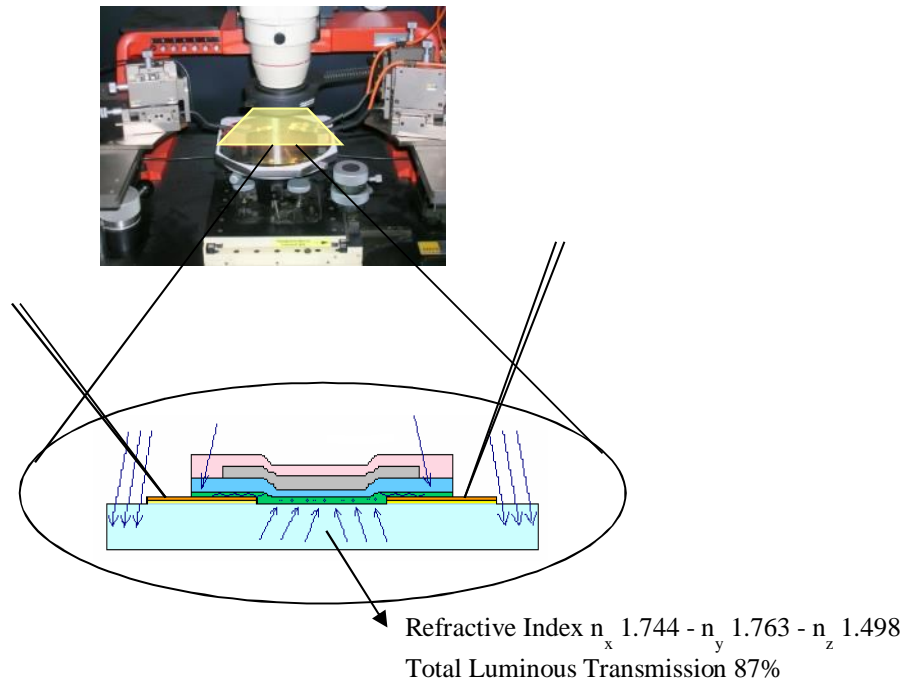
Refractive Index n_x 1.744 - n_y 1.763 - n_z 1.498
Total Luminous Transmission 87%

Fig. 19 Measurement setup for light sensitivity.

A filter can be applied to investigate at which wavelengths the devices are sensible. Either a positive or a negative gate bias, $V_{g,stress}$ can be applied during the light exposure in order to verify the influence of the accumulated charges on the light effects. As it can be seen in Fig. 20 and Fig. 21, a shift towards right of the transfer characteristic has been observed for both negative and positive gate voltages.
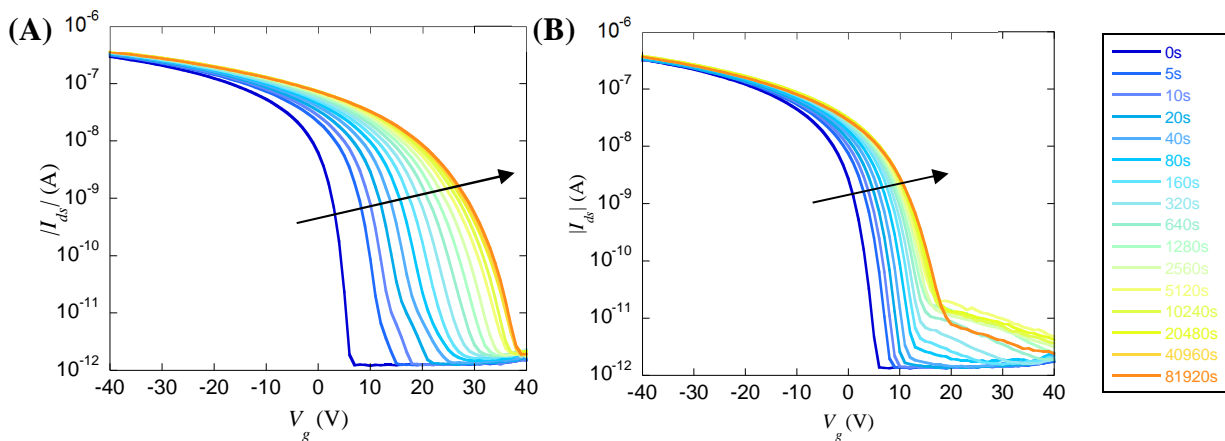
Fig. 20 Gate bias stress with high light intensity and (A) V_g = 40 V (B) V_g = - 40 V. OTFTs is a L = 100 μm, W = 100 μm.

This observation suggests that, in both cases, the shift is induced by the trapping of negative charges generated by the light. For a stress with $V_{g,stress} > 0$, the shift is larger in the subthreshold region, for $V_{g,stress} < 0$ it is lower but uniform along the curve. A positive voltage causes a higher

22

electron trapping and consequently higher current through the channel. Since the shift is rigid in the subthreshold region, it may be an indication that it is trapping just in the semiconductor and not at the interface with the dielectric.
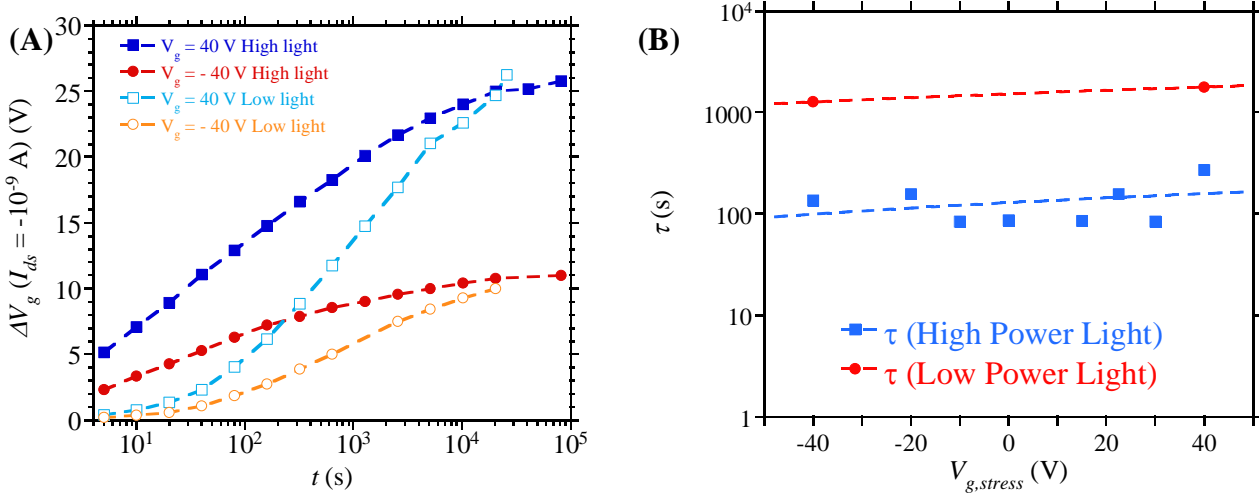

Fig. 21 (A) V_g **shifts for a fixed subthreshold** I_{ds} **in the time. (B) Variations as a function of the applied** $V_{g,stress}$ **and light intensity.**

The V_g shifts for a fixed subthreshold I_{ds} in the time are plotted to study the process dependence on the applied bias and light intensity (Fig. 21 A). For these devices, higher light intensity causes a faster shift but the saturation level is the same. It is an indication that the number of charges trapped is not a function of the light intensity. These curves can be fitted as stretched exponential:

$$\Delta V_g = \Delta V_{sat} \cdot \left(1 - e^{-(t/\tau)^\beta}\right)$$
Eq. 11

where ΔV_{sat} is the shift value in saturation, after the device stabilization, while τ is the characteristic time of the process (relaxation time) and β is the dispersion parameter.[42] The evaluation of these parameters is useful to analyse the mechanism of the light influence on the device. For example, the variation in the value of τ as a function of the applied light intensity or $V_{g,stress}$ can be observed. For these devices, the first one is significant, while the $V_{g,stress}$ dependence has lower influence (Fig. 21 B).

The transistor can recover the before stress condition by thermic release of trapped charge or holes recombination. To study the recovery process, the devices are kept in dark at room temperature and measured periodically (Fig. 22 A).
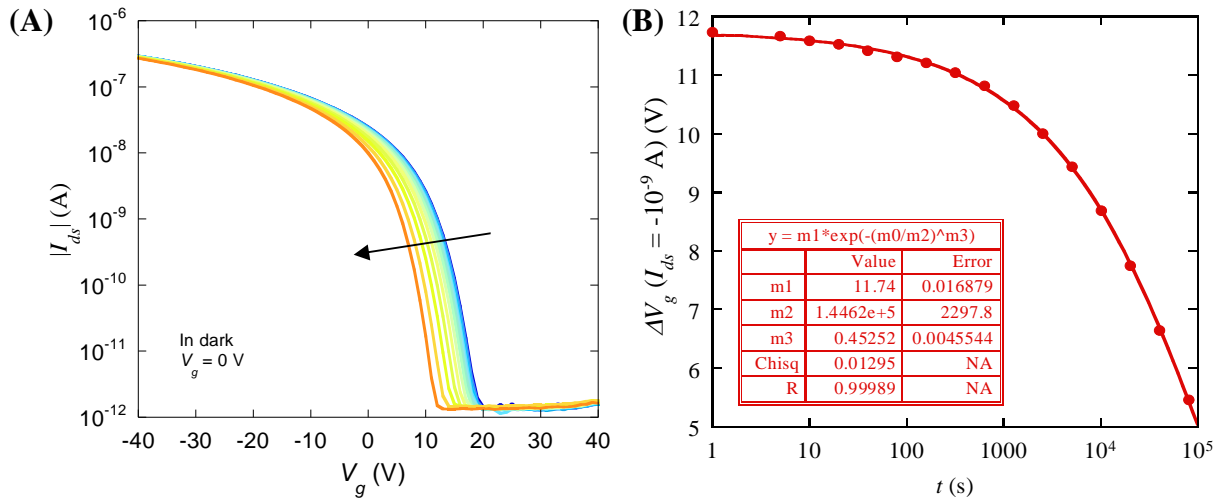
Fig. 22 Recovery. (A) Transfer characteristics measured at different times while the device is kept in dark. Scale time colours as for the stress (Fig. 21). (B) Fitted gate voltage shifts as a function of time.

From the transfer curves, the recovery trend curve (Fig. 22 B) is calculated and then fitted to obtain the recovery time τ, which indicate the time needed for the device to completely recover the stress and their original performances. The V_g shifts follow a stretched exponential defined as:

$$\Delta V_g = \Delta V_{sat} \cdot e^{-(t/\tau)^\beta}$$
Eq. 12

The recovery of these devices is slow, $\tau \sim 10^5$ s, compared to the time of stress application.

In summary, for these devices, the light sensitivity could be due to electrons trapping in the OSC, from the ΔV_{sat} and τ parameters analysis it has been observed that the saturation level depends on the gate voltage, while the process velocity is a function of the light intensity. This process could be explained by the generation of acceptor like metastable states produced by negative charges.

3.5. Mechanical reliability

To verify the device flexibility its performance when subjected to a mechanical stress have to be tested. The aim of the test is to measure the OTFT performances during the mechanical stress (Fig. 23) and the residual stresses after the strain application. The substrate is fixed to a curved support with bending radius R equal to 0.5 or 0.25 cm and it is electrically characterized before bending on a plane surface, during bending in curved position and after the bending in plane.
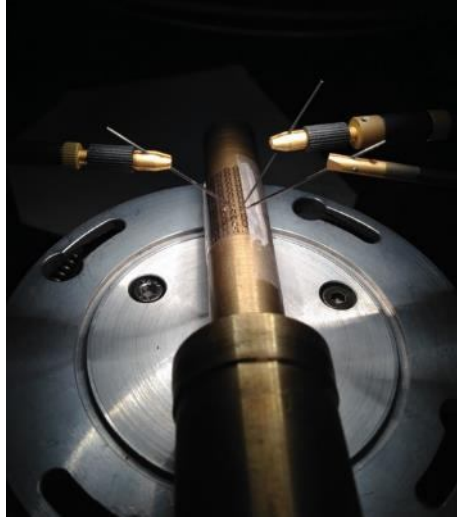
Fig. 23 Measurement setup for bending tests.

The strain is calculated as $\varepsilon_s = d_{PEN}/2R$, where d_{PEN} is the substrate thickness. In Fig. 24 the results of this measurements are shown. Increasing the strain the device shows a variation in the mobility, up to 15% and 30% for strain of 1.5% and 2.5%, respectively. This variation is completely reversible for lower strain, while for higher the mobility after the bending results 20% lower than before the stress. In this condition, also the I_{OFF} increases.
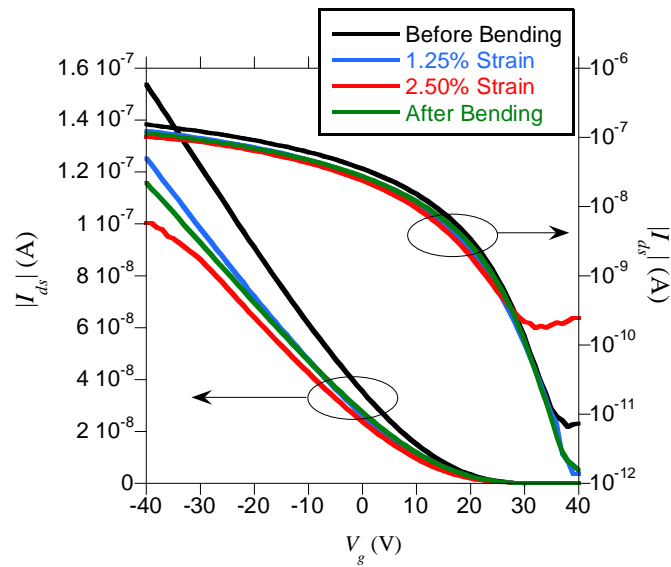
Fig. 24 OTFT transfer curve, $L = 100$ μm, $W = 100$ μm.

4. Dielectric

The dielectric layer plays a significant role in OTFTs performances, since the process of charge accumulation and transport occurs at the interface between the gate dielectric and the semiconductor.

The previous discussed OTFT parameters depend on the semiconductor and its interface with the S/D contacts, but they are also determined by the interface with the dielectric and its properties.[10,16]

The main **requirements** for a gate insulator are the follows:

- high breakdown voltage;

- low concentration of impurities, which could act as traps;

- environmental stability;

- processability, e.g. deposition from solution or low temperature annealing;

- compatibility with the other layers, in particular solvent orthogonality to the semiconductor.[10]

The Organic Gate Insulator (OGI) electrical properties have been characterized realizing and testing capacitors with different thickness and sizes.

Moreover, since the OTFT configuration used is TGBC, this layer acts as a passivation layer, so the environmental stability is necessary not only to avoid charge trapping, but also to protect the OSC from humidity. The water molecules in the air are inclined to interact with the semiconductor, and both worsen mobility and threshold voltage, the I_{ON}, and increase the leakage in the OSC bulk, the I_{OFF}.[14] So the material has been tested for its environmental stability.

4.1. Electrical characterization

To test the electrical properties of the dielectric material capacitors have been realized and characterized. To achieve different thicknesses, the material dilution and the spin-coater spinning speed has been varied, the trend is reported in the following graph (Fig. 25) for two substrates, silicon wafers or aluminium thermally deposited on a wafer. The measurements on PEN foils are in good agreement with the measurements on silicon wafers.
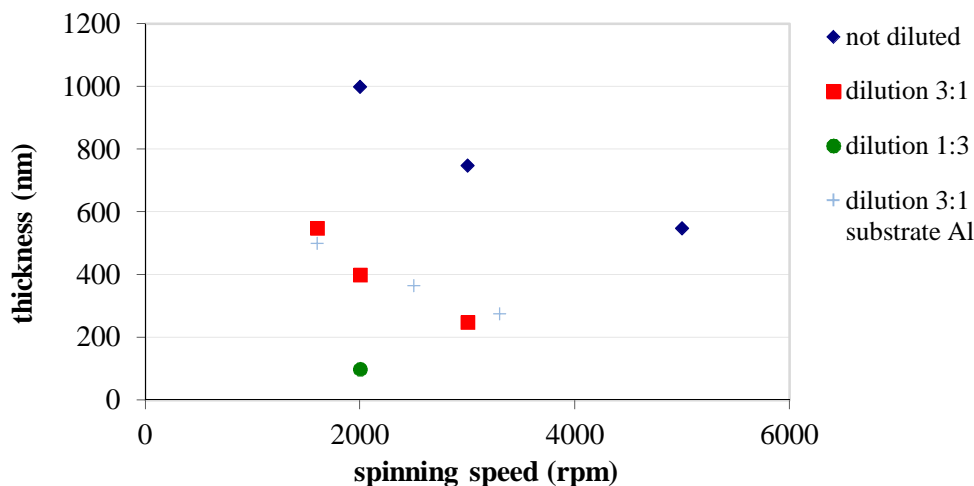
Fig. 25 Dielectric thicknesses as a function of the spin-coater speed and of the substrate.

The devices configuration is Metal-Insulator-Metal (**MIM**), obtained with the following procedure.

1. Substrate, doped silicon, cleaning: deep in BHF solution diluted 1:10.

2. Dielectric (Cytop™ CTL809M, diluted 3:1 in its solvent, CT-Solv180, AGC Chemicals) deposition directly on the wafer through spin-coating technique.

3. Annealing 1 h at 100°C in vacuum oven.

4. Top contact deposition by thermal evaporation of 50 nm thick aluminium.

5. Top contact patterning with optical lithography (positive resist Shipley 1813) and metal wet etching (4 H_3PO_4 : 4 CH_3COOH : 1 HNO_3 : 1 H_2O, etch rate $\approx$ 41 nm/min).

The electrical characterization of these devices has been performed with a 4140B pA Meter/DC voltage source Hewlett Packard. The I-V characteristics obtained using a continuous voltage ramp, ramp rate 1 V/s, are shown in Fig. 26.
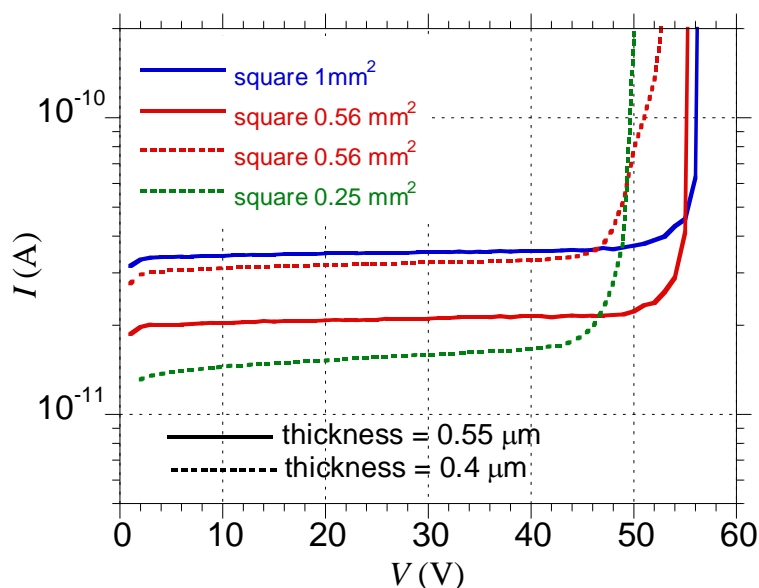
Fig. 26 I-V characteristics of the MIM realized with spin-coated dielectric.

At low voltages, the measured current is the capacitor displacement current, from which it is possible to calculate the device capacitance since $I = C_i \cdot r_r$, where r_r is the ramp rate (for these measurements 1 V/s). The breakdown voltage is around 45-55 V, depending on the thickness, corresponding to a dielectric strength $E_{ds} \approx 1$ MV/cm, in agreement with the specification reported for this material.

4.2. Environmental stability

To test the properties of the dielectric material as passivation layer the material has been deposited and characterized after a defined time in critical humidity and temperature conditions. The dielectric material (Cytop™ 800 CTL809M as is or diluted 3:1 in its solvent CT-Solv180, AGC Chemicals) is spin-coated directly on the wafer of doped silicon. Two thicknesses has been investigated, 960 nm and 550 nm. The layers have been studied through thermo-gravimetric analysis (TGA), these measurements have been performed by Maurizio Greco and Vincenzo Vinciguerra at STMicroelectronics in Catania, Italy.

The measurements procedure to evaluate the humidity adsorption is the following:
- the devices are weighted;
- exposition 24 h in autoclave at 121°C and relative humidity 100%
- the devices are weighted again

The results are shown in the following table:

Sample thickness	Weight (g) t = 0 h	Weight (g) t = 24 h	Weight variation (%)
0.5 μm	4.1021	4.1021	0 %
1 μm	3.9837	3.9832	- 0.01255 %

Then, the samples are subjected to the exsiccation process:

- exposition 24 h in autoclave at 150°C in N_2;

- the devices are weighted again

The results are shown in the following table:

Sample thickness	Weight (g) t = 0 h	Weight (g) t = 24 h	Weight variation (%)
0.5 μm	4.1021	4.1020	0.00243 %
1 μm	3.9837	3.9832	0.01255 %

The stability of this material has been demonstrated and it has shown good resistance to water vapour permeability.

References

(1)   Forrest, S. R. The Path to Ubiquitous and Low-Cost Organic Electronic Appliances on Plastic. *Nature* **2004**, *428* (6986), 911–918.

(2)   Liao, C.; Zhang, M.; Yao, M. Y.; Hua, T.; Li, L.; Yan, F. Flexible Organic Electronics in Biology: Materials and Devices. *Adv. Mater.* **2015**, *27* (46), 7493–7527.

(3)   Lanzani, G. Materials for Bioelectronics: Organic Electronics Meets Biology. *Nat. Mater.* **2014**, *13* (8), 775–776.

(4)   Someya, T.; Kato, Y.; Sekitani, T.; Iba, S.; Noguchi, Y.; Murase, Y.; Kawaguchi, H.; Sakurai, T. Conformable, Flexible, Large-Area Networks of Pressure and Thermal Sensors with Organic Transistor Active Matrixes. *Proc. Natl. Acad. Sci. U. S. A.* **2005**, *102* (35), 12321–12325.

(5)   Schwartz, G.; Tee, B. C.-K.; Mei, J.; Appleton, A. L.; Kim, D. H.; Wang, H.; Bao, Z. Flexible Polymer Transistors with High Pressure Sensitivity for Application in Electronic Skin and Health Monitoring. *Nat. Commun.* **2013**, *4*, 1859.

(6)   Fukuda, K.; Someya, T. Recent Progress in the Development of Printed Thin-Film Transistors and Circuits with High-Resolution Printing Technology. *Adv. Mater.* **2016**.

(7)   Baeg, K.-J.; Caironi, M.; Noh, Y.-Y. Toward Printed Integrated Circuits Based on Unipolar or Ambipolar Polymer Semiconductors. *Adv. Mater.* **2013**, *25* (31), 4210–4244.

(8)   Forrest, S. R.; Thompson, M. E. Introduction: Organic Electronics and Optoelectronics. *Chem. Rev.* **2007**, *107* (4), 923–925.

(9)   Street, R. A. Thin-Film Transistors. *Adv. Mater.* **2009**, *21* (20), 2007–2022.

(10)   Zaumseil, J.; Sirringhaus, H. Electron and Ambipolar Transport in Organic Field-Effect Transistors. *Chem. Rev.* **2007**, *107* (4), 1296–1323.

(11)   Köhler, A.; Bässler, H. *Electronic Processes in Organic Semiconductors*, 1st ed.; Wiley-VCH Verlag GmbH & Co. KGaA.: 2015.

(12)   Brütting, W. *Physics of Organic Semiconductors*; WILEY-VCH Verlag GmbH & Co. KGaA, 2005.

(13)   Bässler, H.; Köhler, A. Charge Transport in Organic Semiconductors. In *Unimolecular and Supramolecular Electronics I*; Metzger, R. M., Ed.; Springer Berlin Heidelberg: Berlin, Heidelberg, 2011; Vol. 312, pp 1–65.

(14)   Raiteri, D.; Cantatore, E.; van Roermund, A. H. M. *Circuit Design on Plastic Foils*; Springer International Publishing, 2015.

(15)   Horowitz, G. Organic Thin Film Transistors: From Theory to Real Devices. *J. Mater. Res.* **2004**, *19* (07), 1946–1962.

(16)   Virkar, A. A.; Mannsfeld, S.; Bao, Z.; Stingelin, N. Organic Semiconductor Growth and Morphology Considerations for Organic Thin-Film Transistors. *Adv. Mater.* **2010**, *22* (34), 3857–3875.

(17)   Grau, G.; Cen, J.; Kang, H.; Kitsomboonloha, R.; Scheideler, W. J.; Subramanian, V. Gravure-Printed Electronics: Recent Progress in Tooling Development, Understanding of Printing Physics, and Realization of Printed Devices. *Flex. Print. Electron.* **2016**, *1* (2), 023002.

(18)   Yan, H.; Chen, Z.; Zheng, Y.; Newman, C.; Quinn, J. R.; Dötz, F.; Kastler, M.; Facchetti, A. A High-Mobility Electron-Transporting Polymer for Printed Transistors. *Nature* **2009**, *457* (7230), 679–686.

(19) Kaltenbrunner, M.; Sekitani, T.; Reeder, J.; Yokota, T.; Kuribara, K.; Tokuhara, T.; Drack, M.; Schwödiauer, R.; Graz, I.; Bauer-Gogonea, S.; Bauer, S.; Someya, T. An Ultra-Lightweight Design for Imperceptible Plastic Electronics. *Nature* **2013**, *499* (7459), 458–463.

(20) Berggren, M.; Nilsson, D.; Robinson, N. D. Organic Materials for Printed Electronics. *Nat. Mater.* **2007**, *6* (1), 3–5.

(21) Kahn, B. E. Patterning Processes for Flexible Electronics. *Proc. IEEE* **2015**, *103* (4), 497–517.

(22) Khan, S.; Lorenzelli, L.; Dahiya, R. S. Technologies for Printing Sensors and Electronics Over Large Flexible Substrates: A Review. *IEEE Sens. J.* **2015**, *15* (6), 3164–3185.

(23) Subramanian, V.; Chang, J. B.; de la Fuente Vornbrock, A.; Huang, D. C.; Jagannathan, L.; Liao, F.; Mattis, B.; Molesa, S.; Redinger, D. R.; Soltman, D.; others. Printed Electronics for Low-Cost Electronic Systems: Technology Status and Application Development. In *Solid-State Device Research Conference, 2008. ESSDERC 2008. 38th European*; IEEE, 2008; pp 17–24.

(24) Myny, K.; Smout, S.; Rockelé, M.; Bhoolokam, A.; Ke, T. H.; Steudel, S.; Cobb, B.; Gulati, A.; Rodriguez, F. G.; Obata, K.; Marinkovic, M.; Pham, D.-V.; Hoppe, A.; Gelinck, G. H.; Genoe, J.; Dehaene, W.; Heremans, P. A Thin-Film Microprocessor with Inkjet Print-Programmable Memory. *Sci. Rep.* **2015**, *4* (1).

(25) Mandal, S.; Noh, Y.-Y. Printed Organic Thin-Film Transistor-Based Integrated Circuits. *Semicond. Sci. Technol.* **2015**, *30* (6), 064003.

(26) Huebler, A. C.; Doetz, F.; Kempa, H.; Katz, H. E.; Bartzsch, M.; Brandt, N.; Hennig, I.; Fuegmann, U.; Vaidyanathan, S.; Granstrom, J.; Liu, S.; Sydorenko, A.; Zillger, T.; Schmidt, G.; Preissler, K.; Reichmanis, E.; Eckerle, P.; Richter, F.; Fischer, T.; Hahn, U. Ring Oscillator Fabricated Completely by Means of Mass-Printing Technologies. *Org. Electron.* **2007**, *8* (5), 480–486.

(27) Kempa, H.; Hambsch, M.; Reuter, K.; Stanel, M.; Schmidt, G. C.; Meier, B.; Hubler, A. C. Complementary Ring Oscillator Exclusively Prepared by Means of Gravure and Flexographic Printing. *IEEE Trans. Electron Devices* **2011**, *58* (8), 2765–2769.

(28) Kitsomboonloha, R.; Morris, S. J. S.; Rong, X.; Subramanian, V. Femtoliter-Scale Patterning by High-Speed, Highly Scaled Inverse Gravure Printing. *Langmuir* **2012**, *28* (48), 16711–16723.

(29) Voigt, M. M.; Guite, A.; Chung, D.-Y.; Khan, R. U. A.; Campbell, A. J.; Bradley, D. D. C.; Meng, F.; Steinke, J. H. G.; Tierney, S.; McCulloch, I.; Penxten, H.; Lutsen, L.; Douheret, O.; Manca, J.; Brokmann, U.; Sönnichsen, K.; Hülsenberg, D.; Bock, W.; Barron, C.; Blanckaert, N.; Springer, S.; Grupp, J.; Mosley, A. Polymer Field-Effect Transistors Fabricated by the Sequential Gravure Printing of Polythiophene, Two Insulator Layers, and a Metal Ink Gate. *Adv. Funct. Mater.* **2010**, *20* (2), 239–246.

(30) Kitsomboonloha, R.; Kang, H.; Grau, G.; Scheideler, W.; Subramanian, V. MHz-Range Fully Printed High-Performance Thin-Film Transistors by Using High-Resolution Gravure-Printed Lines. *Adv. Electron. Mater.* **2015**, *1* (12), 1500155.

(31) Hernandez-Sosa, G.; Bornemann, N.; Ringle, I.; Agari, M.; Dörsam, E.; Mechau, N.; Lemmer, U. Rheological and Drying Considerations for Uniformly Gravure-Printed Layers: Towards Large-Area Flexible Organic Light-Emitting Diodes. *Adv. Funct. Mater.* **2013**, *23* (25), 3164–3171.

(32) Grau, G.; Subramanian, V. Fully High-Speed Gravure Printed, Low-Variability, High-Performance Organic Polymer Transistors with Sub-5 V Operation. *Adv. Electron. Mater.* **2016**, *2* (4), 1500328.

(33) Newman, C. R.; Frisbie, C. D.; da Silva Filho, D. A.; Brédas, J.-L.; Ewbank, P. C.; Mann, K. R. Introduction to Organic Thin Film Transistors and Design of N-Channel Organic Semiconductors. *Chem. Mater.* **2004**, *16* (23), 4436–4451.

(34) Dimitrakopoulos, C. d.; Malenfant, P. r. l. Organic Thin Film Transistors for Large Area Electronics. *Adv. Mater.* **2002**, *14* (2), 99–117.

(35) Boudinet, D.; Benwadih, M.; Qi, Y.; Altazin, S.; Verilhac, J.-M.; Kroger, M.; Serbutoviez, C.; Gwoziecki, R.; Coppard, R.; Le Blevennec, G.; Kahn, A.; Horowitz, G. Modification of Gold Source and Drain Electrodes by Self-Assembled Monolayer in Staggered N- and P-Channel Organic Thin Film Transistors. *Org. Electron.* **2010**, *11* (2), 227–237.

(36) Risteska, A.; Steudel, S.; Nakamura, M.; Knipp, D. Structural Ordering versus Energy Band Alignment: Effects of Self-Assembled Monolayers on the Metal/Semiconductor Interfaces of Small Molecule Organic Thin-Film Transistors. *Org. Electron.* **2014**, *15* (12), 3723–3728.

(37) Cipolloni, S.; Mariucci, L.; Valletta, A.; Simeone, D.; De Angelis, F.; Fortunato, G. Aging Effects and Electrical Stability in Pentacene Thin Film Transistors. *Thin Solid Films* **2007**, *515* (19), 7546–7550.

(38) Simeone, D.; Rapisarda, M.; Fortunato, G.; Valletta, A.; Mariucci, L. Influence of Structural Properties on Environmental Stability of Pentacene Thin Film Transistors. *Org. Electron.* **2011**, *12* (3), 447–452.

(39) Hamilton, M. C.; Martin, S.; Kanicki, J. Thin-Film Organic Polymer Phototransistors. *IEEE Trans. Electron Devices* **2004**, *51* (6), 877–885.

(40) Schroder, D. K. *Semiconductor Material and Device Characterization*, 3rd ed.; John Wiley & Sons, Inc., publication, 2006.

(41) Prakash, S.; Karacor, M. B.; Banerjee, S. Surface Modification in Microsystems and Nanosystems. *Surf. Sci. Rep.* **2009**, *64* (7), 233–254.

(42) Rapisarda, M.; Fortunato, G.; Valletta, A.; Jacob, S.; Benwadih, M.; Coppard, R.; Chartier, I.; Mariucci, L. Self-Heating Effects on the Electrical Instability of Fully Printed P-Type Organic Thin Film Transistors. *Appl. Phys. Lett.* **2012**, *101* (23), 233304.

Chapter 2
Gravure printing

1. Physics of the gravure printing technique

The gravure printing system consists of a large plate or cylinder (cliché), usually metallic, with engraved cells with dimensions in the order of tens of microns. The cells are filled by the ink either rotating the cylinder in a reservoir or through a nozzle dispenser. A doctor blade removes the ink excess from the cliché, then the ink is transferred when the substrate goes through an impression cylinder and the engraved one.[1] As schematized in Fig. 1, during the gravure printing process it is possible to identify four steps: filling, wiping, transferring and levelling.[2–5]

Due to the microscale dimensions of the cells, viscous and surface tension forces dominate inertial and gravity ones during the whole process.[3] The ink flow is ruled by the wettability of the ink towards the printing cliché, the doctor blade and the substrate, with substantially different behaviours in each step.[2,3]
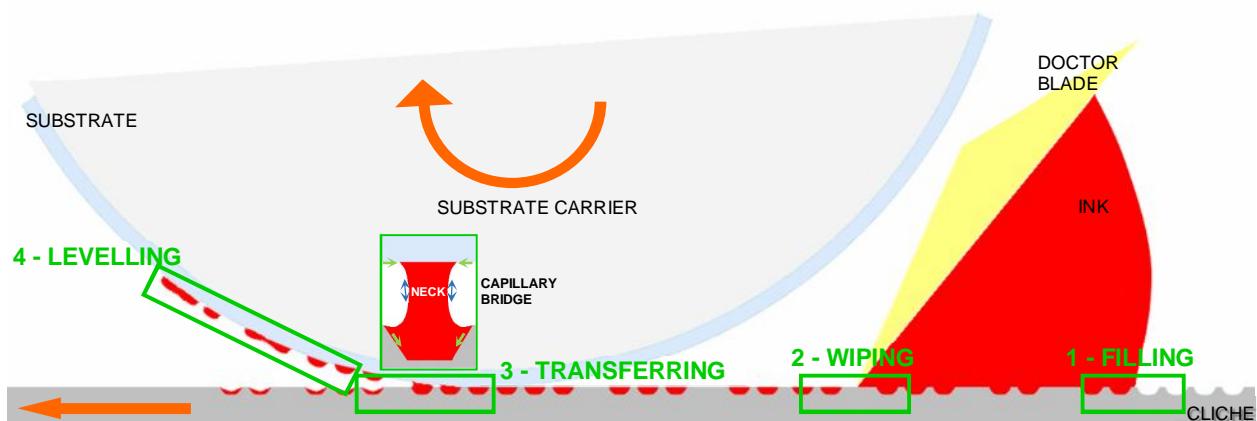
Fig. 1 The four steps of the gravure printing process. In particular, it is schematized an inverse direct gravure printing technique (out of scale).

During the **filling** step, the cells, engraved on the printing cliché, are overfilled with ink. Particularly, the advance of the ink moving contact line on the cliché and the deformation of fluid are due to capillary forces under the constraint imposed by the cell.[3] Throughout the cell filling, the overall fluid front moves at the printing speed and gets pinned at the edge of the cell. Then the pinned fluid front is driven by surface tension forces into the cell from the first edge where the moving contact line has been pinned. The overall fluid front continue in advancing around the cell, gets over

it and eventually the moving contact line recover the minimum surface energy state, that is a straight line.[2,3]

During the **wiping** step, the ink excess is removed from the cliché by the doctor blade. A new ink free surface is created not at the same level of the printing cliché surface, the so called "land area", but above or under the blade due to the capillary flow of the ink. This results in the formation of undesired ink residue volumes on the cliché, the drag-out tails and the lubrication film.[2,3,6]

The *drag-out tails* are a consequence of the ink interactions between the blade and the cells.[2] While the doctor blade moves forward, the gradient of hydrostatic pressure between the cell and the land area, favoured as smaller is the wedge between the blade tip and the cliché, generates a capillary flow of the ink on the back of the blade, afterwards deposited behind the cell. This meniscus shrinks as the blade advances, generating the drag-out tail.[2,3,6]

The *lubrication film* is a continuous thin uniform layer which is due to ink flow between the doctor blade and the printing cliché.[3,6] A lubrication flow is developed by a fluid between two solid boundaries, in this case the blade and the cliché, whose separation is much smaller than the other system dimensions.[6,7] This flow avoids solid-solid contact of the boundaries, reducing the friction that would cause an excessive wear. The generated gap is small enough to induce a high fluid pressure sufficient to deform elastically locally the rigid materials, such as the steel of the blade, as well as to vary the ink viscosity in the gap. In these conditions, the lubrication operates in the piezoviscous-elastic regime or elastohydrodynamic lubrication regime (EHL).[3,6,7] Furthermore, the blade translates vertically or bends as a response to the applied load, generating a moment, including the pressure applied to the blade support and the gravity force.[7]

During the **transferring** step, the substrate contacts the free surface of the ink in the cells and the material is pulled onto the substrate. A capillary bridge is created by the ink between the cell on the cliché and the substrate (Fig. 1, enlarged scheme). Its contact lines (green arrows) on the substrate and the cliché surfaces slip until the capillary break-up due to the rising capillary pressure in the neck (blue arrows), determining the amount of ink transferred on the substrate.[2,3,8] The fluid filament has to be pushed out of the cell before the surfaces are separated.[9] Two characteristic times rule the transferring dynamics and determine the amount of transferred ink. The first one, linked to the moving contact lines, is a function of the capillary pressure gradient. The second one, related to the liquid bridge breaking time, depends on the separation velocity and controls the neck formation.[3,9,10] The capillary pressure gradient, which is the guiding force for the slipping contact lines towards the axisymmetric axis, is due to the difference in the fluid curvature on the substrate and on the cliché.[3]

During the **levelling** step, the individual droplets deposited by the single cells spread to create a continuous pattern and then the film rearranges itself to attain the state of lowest surface energy.[2–4] Final free surface formation and ink levelling on the substrate are dominated by the surface tension gradient, considering that the time available is limited by the solvent drying and by the ink viscosity.[4] Surface energy minimization in very thin layers could have opposite outcomes, preventing or facilitating the film levelling if the non–uniformities are induced by the disjoining pressure or by the Saffman-Taylor instabilities, respectively (Fig. 2).[2]
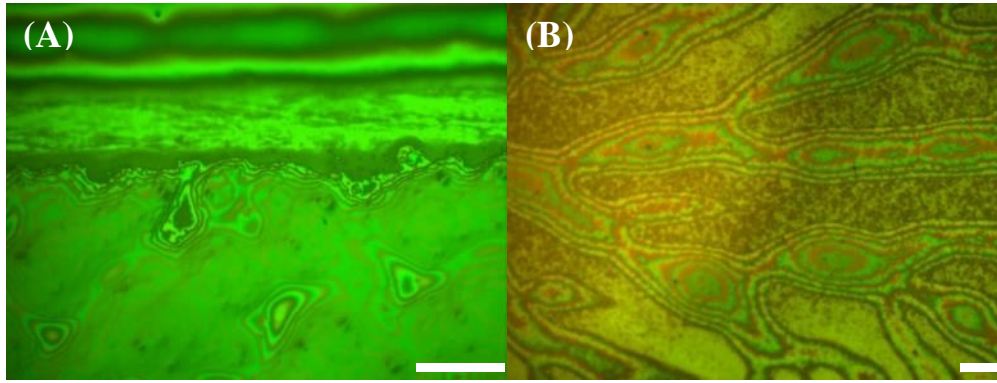
Fig. 2 Spinodal dewetting (A) and viscous fingering (B) effects in PEDOT:PSS printed films. Scale bar 100 μm.

The *disjoining pressure* is the difference between the normal pressure in thin films (few 10s of nm) and the pressure in the adjoining bulk film.[11,12] The disjoining pressure gradient generates a fluid flow from the thinner to the thicker region of the film. This *spinodal dewetting* process modulates the film thickness with typical pattern sizes λ_s if the characteristic time, the rupture time τ_s, is smaller or in the order of the drying time.[2,11,12] λ_s and τ_s are related to the surface tension, γ, the disjoining pressure, P_{disj}, the film thickness, h, the viscosity, η, and the Hamaker constant of the solvent, A, by the following relations:

$$\lambda_s = \sqrt{-\frac{8\pi^2\gamma}{\partial^2 P_{disj}/\partial h^2}}$$

Eq. 1

$$\tau_s = 48\pi^2\eta\gamma\frac{h^5}{A^2}$$

Eq. 2

The spinodal dewetting process promotes the pattern formation in the time between the printing and the film drying.[12]

The undulations caused by the so-called *Saffman-Taylor instabilities*, or *viscous fingering*, will be levelled by the surface energy minimization. When the substrate is detached from the cliché finger-like patterns of air penetrate in the ink. The small disturbances at the interface between ink and air

increase, due to difference in pressure gradient in the ink between the tip and the base of the air fingers (Fig. 1 B). The ink transferred shows undulations, with predominant wavelength λ_{ST}:

$$\lambda_{ST} = \sqrt{\frac{\eta U h^3}{\gamma X}}$$

where U is the printing speed, X is defined as the distance of the fluid meniscus at the nip to the point where the cliché touches the substrate. The undulations completely rearrange themselves with a timescale in the order of τ_{ST}, as defined in Eq. 4.[2,11,12]

$$\tau_{ST} = \frac{3\eta \lambda_{ST}^4}{16\pi^4 \gamma h^3}$$

Considering both these effects, *drying time* has to be lower than τ_s, to avoid spinodal dewetting causing non uniformities, and higher than τ_{ST}, to level undulations caused by Saffmann-Taylor instabilities.

2. Gravure printing system optimization

The gravure printer used in this work is a Labratester, Norbert Schläfli Maschinen, Fig. 3.
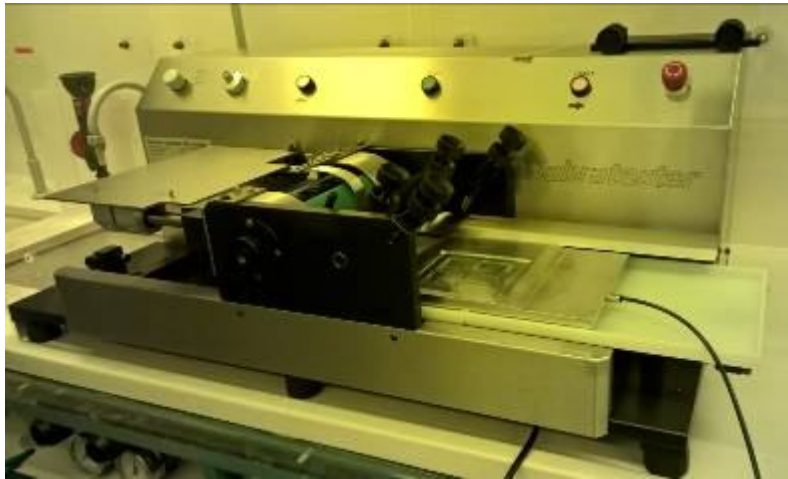
Fig. 3 The gravure printer.

This printing system is a so called "inverse direct gravure printing", because the cliché used to transfer patterns to a substrate is a flat plate instead of a roll.[3] This setup allows for direct imaging of each different step during the printing process and is comparable to the conventional system.[3]

Considering the physics of the gravure printing technique, the main issue faced in order to improve the printing process has been the definition of a suitable printing cliché, combined with a proper blade.

2.1. Layout definition for the metallic cliché

The gravure cliché is made of a steel core covered with a copper layer, the so called ballard skin, which is engraved to define the cells. A chromium layer is then galvanically deposed to protect the cliché both mechanically and chemically.[13]

The standard metallic cliché is mechanical engraved with a stylus, with resolution down to 5 µm. This technique allows to obtain pyramidal cells with rhombic shape (Fig. 4).
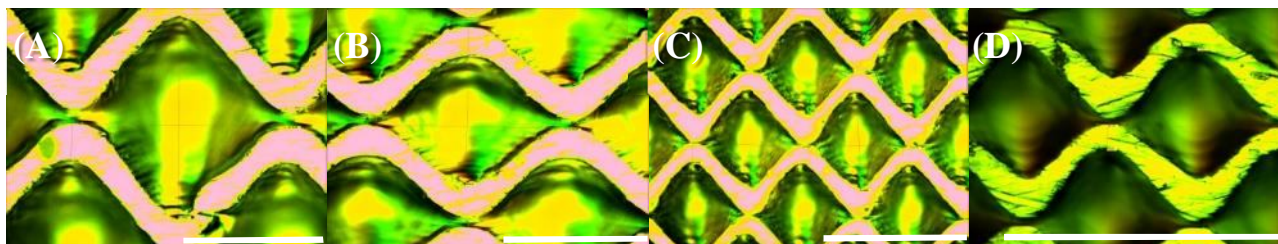
Fig. 4 Standard cliché cells with different engraving resolution: (A) 80 lines/cm, (B) 100 lines/cm, (C) 160 lines/cm, (D) 210 lines/cm. Scale bar 100 µm.

This metallic cliché with mechanical engraved cells has been used for the first tests of gravure printing. This method does not allow to define highly scaled features and the cell structure can only be pyramidal.

As known from literature, the gold standard as gravure cliché consists of a metallic master with a cell-based pattern obtained by laser engraving technique.[2,13,14] A metallic cliché defined with this technique has been designed and used to have a standard reference for the printing process (Fig. 5). The CAD software used for all the cliché layout design has been Lasi7.
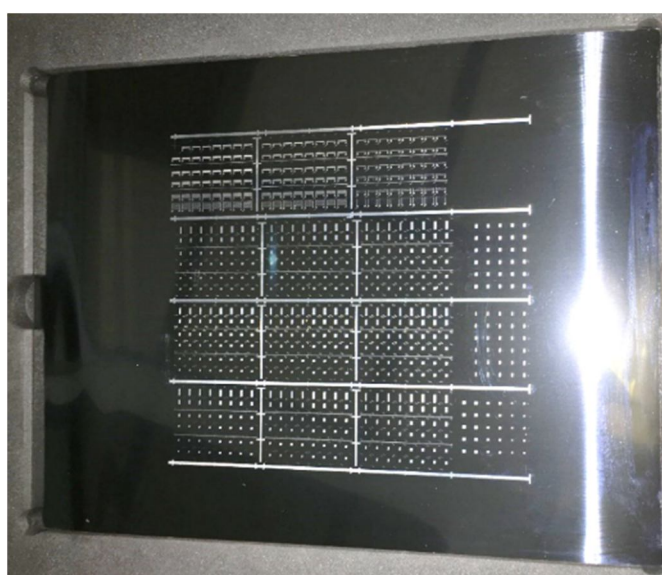
Fig. 5 High resolution metallic cliché.

The layout defined is shown in Fig. 6. The cliché has been realized by GRT GmbH&Co.
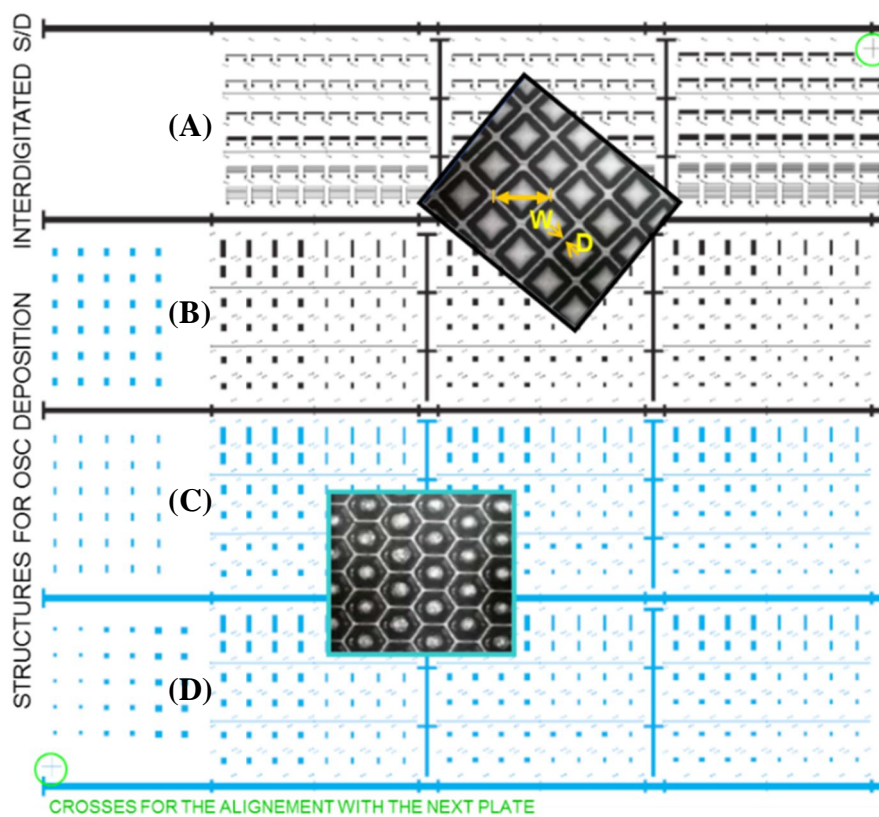
Fig. 6 Layout for the high resolution metallic cliché.

Two different areas have been defined either to test the organic conductive (A area) or semiconductor and dielectric (B, C, D areas) inks.

The A area includes S/D interdigitated contacts as detailed in the following scheme (Fig. 7).

L = 5-10-20-50-100 µm

S = 15-25-50 µm
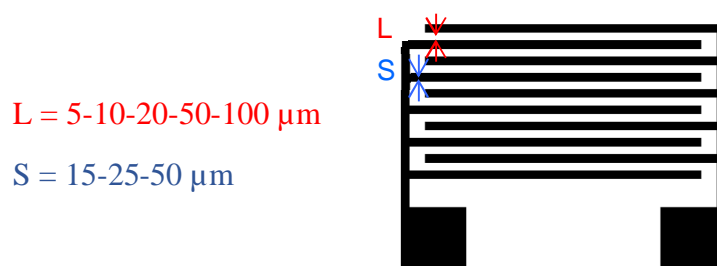
Fig. 7 S/D interdigitated contacts layout.

The B, C, D areas have different cell shape and patterned area, as follows:

- B: rhombic cells, 276.7 lines/cm, gap 3.5 µm

- C, D: honeycomb cells, 172 lines/cm, gap 6.2 µm

For both the cell shapes, the depth is 4 µm.

The system ensures a registration accuracy between different metallic clichés in the range of 50 µm, while the correct positioning is provided by two dowels fitted without backlash. The substrate alignment is mechanical, positioning it on the feeding table in contact with the guides.

2.2. Glass cliché optimization

2.2.1. Cliché requirements

The main cliché requirements are a consequence of the physics of the printing process, previously exposed.

The first strict requisite is the possibility to modify its **wettability** since the ink flow is ruled by the wettability of the ink towards the printing cliché, the doctor blade and the substrate.[2,3]

Then, critical features are the **cell aspect ratio** and **wall slope**. The filling step is facilitated by a suitable cell wall slope and a low cell aspect ratio (height to width), which enhance the fluid flow into the cell.[2,3] Similarly, during the transferring step, since the capillary pressure gradient is due to the difference in the fluid curvature on the substrate and on the cliché, a small cell wall slope and a low aspect ratio enhance the ink transferring to the substrate.[3,8,10,15] The most suitable cell geometry is reported to be a sloped cell wall with rounded edges at the bottom of the cell as similar as possible to a U-shape.[16]

The **cell shape** has to be carefully studied as during the filling step the ink enters into the cell from the first edge where it has been pinned, suggesting the use of hexagonal or rhombic shaped cells.[3] Instead, considering the wiping step, some characteristics of the cell shape could enhance the drag-out tails formation. Indeed, their length is proportional to the cell length in the printing direction and the ratio of the drag-out volume and cell volume increases for smaller cells, so reducing the cell filling.[2,3] Among the main relevant factors influencing the lubrication layer thickness it can be found a strong dependence on the gap shape.[2,6,7]

At last, the **pattern of the cells** and the **gap** between them have to be fitted to the fluid dynamic characteristics of each ink, due to the cell influence on the ink capillary flow. In particular, the cell pattern on the cliché has to be optimized to improve the ink spreading on the substrate. The ink volume per unit area is defined by the cell volume and the gaps among the cells, if it is too large it will induce bulging, on the contrary a too small volume per unit area will lead to a discontinuous film.[2]

Considering the current methods to define the cliché pattern, the laser engraving technique used for high resolution metallic cliché allows high pattern resolution, down to 2 µm, but it has some

drawbacks. The cell edges are quite marked and the roughness at the bottom of the cell is quite high, the procedure is expensive and the cleaning is sometimes ineffective to prevent cell clogging.[2,15,17] Moreover, small amounts of chromium are removed during the wiping step by the blade, consequently leading to poor cliché durability and metallic particle dispersion in the inks, which degrades the electrical properties.[13]

The more advanced silicon microfabricated clichés recently developed, although with nearly atomically perfect surface, suffer from the limitations in the possibility of scaling up the cliché size above the silicon wafer dimensions, at most 300 mm diameter.[2]

To overcome these issues, complying the above detailed requirements, a glass cliché fabrication process has been developed. The choice of the glass as material for the cliché is promising to achieve high resolutions on large areas. This material avoids the metallic particles dispersion in the inks, it is cheap and easily cleanable with various solvents or a piranha etch.[2,13]

2.2.2. Holder for the cliché

To mount the cliché on the gravure printer a proper holder has been designed, considering that the cliché position has to be strictly constrained to avoid misalignments.

The metallic holder (Fig. 8, Fig. 9) has been designed in aluminium to avoid damages by solvents. It fits the printer dowels without backlash and the plane ensure the proper flatness. The cliché is kept in position through a vacuum system (Fig. 9 B).
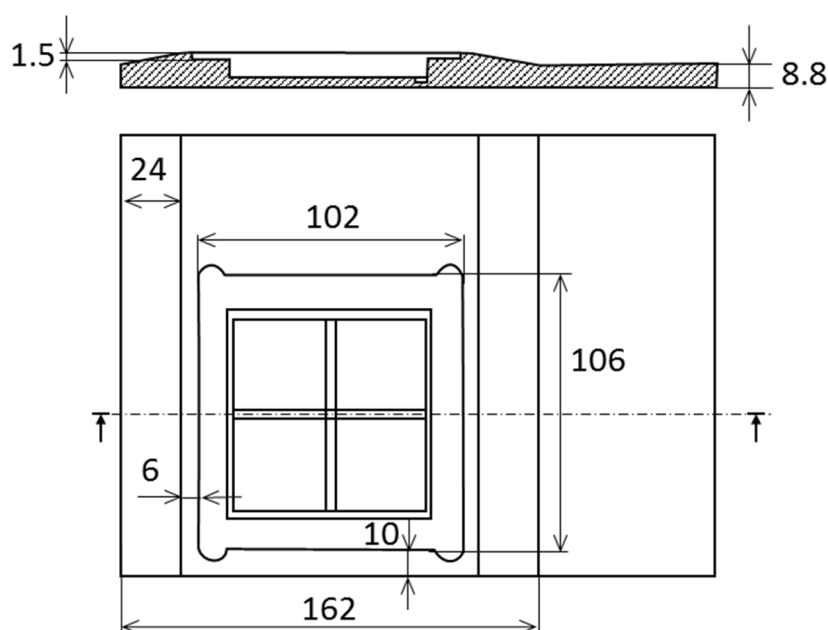
Fig. 8 Design for the cliché holder. Measurements are in mm.
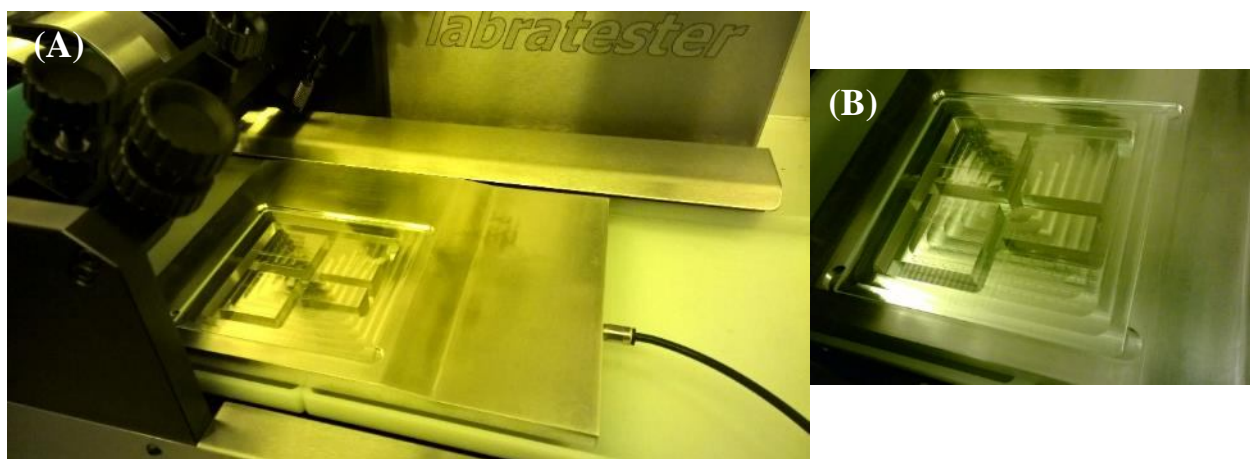
Fig. 9 (A) Cliché holder mounted on the gravure printer. (B) Particular of the cliché housing with the glass cliché.

2.2.3. Cliché fabrication

To realize the clichés, 4"soda lime lithographical masks (4X4X.060 SL LRC D 2,8 std./AZ std.) have been used as blank and patterned following the procedure exposed hereafter.

The designed CAD layout has been reproduced on the mask through laser exposure of photolithographic resist (laser lithography system DWL 66 Heidelberg Instruments, Fig. 10).

Fig. 10 The laser lithography system.

The wet etching has been chosen as it allows to obtain the most suitable cell geometry, the U-shape. The glass etching procedure has been optimized from the techniques used for microfluidic applications.[18,19] The aim of the optimization work has been to obtain a bottom of the cell with low

roughness, to avoid defects due to a non homogeneous etching, to achieve a high control and reproducibility of the technique.

As first etching solution, buffered hydrofluoric acid (BHF, J.T. Baker, CMOS grade, 7:1 hydrofluoric acid in ammonium fluoride) has been used. Both resist and chromium layers have been used as masking layers during the glass etching and then removed with standard techniques (CHROME ETCH 18, OSC OrganicSpezialChemie GmbH). This solution has shown to etch the glass non uniformly (Fig. 11).
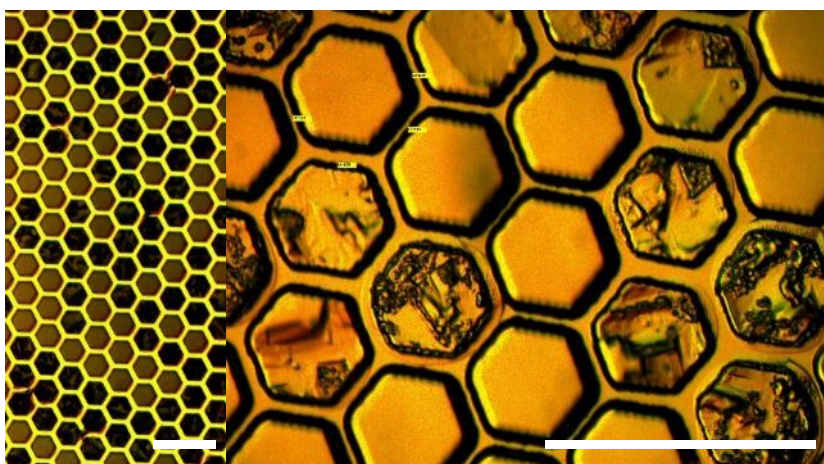
Fig. 11 Non uniform glass etch using a non optimized wet etching process. The less rough cells are 5.7 µm in depth, while the more rough ones are 2.2 ± 0.3 µm. Scale bar 100 µm.

The etch reaction produces some insoluble oxides, which prevents further glass attack. To avoid this issue, hydrochloric acid (HCl, 37%, J.T. Baker, CMOS grade) has been added to the etching solution, since it can dissolve these oxides.[19] The HCl does not etch the chromium, since the layer of chromium oxide and the resist protect it from damaging. It has been paid particular attention on avoiding even little air bubbles in the solution, since it would result in non etched areas in the cliché (Fig. 12).
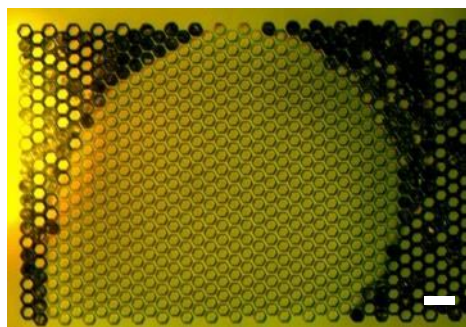
Fig. 12 Defect in the glass etching due to an air bubble. Scale bar 100 µm.

It has been observed that the resist layer above the chromium has been damaged by the etching, inducing softening of the resist. The consequent chromium bending has prevented the lateral etching of the cells, resulting in a bad cell slope profile. To solve this issue the resist has been hard baked before the glass wet etching (40 min at 120°C in oven).[19]

Since the glass wet etching is almost isotropic, the lateral etch rate has been carefully controlled to avoid undercutting effects.[19] The cell pattern has been defined to compensate these effects, in particular properly sizing the cell gaps and area (Fig. 13).
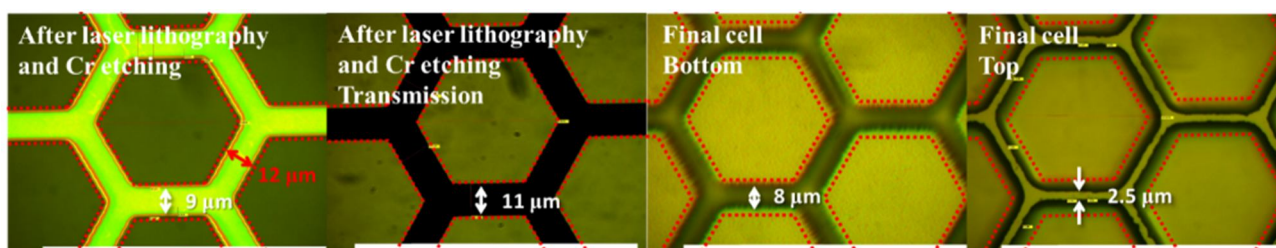
Fig. 13 Example of cell gap size control during the glass cliché realization. In red the original CAD pattern and its gap size, in white the cliché measurements. Scale bar 100 μm.

The optimized glass wet etching has been obtained using a solution of H_2O:HCl:BHF 2:2:1, attaining an etch rate around 1.9 μm/min. An etch control down to 0.5 μm has been achieved.

As shown in the optical microscopy pictures (Fig. 14), with the glass cliché developed it has been possible to obtain resolutions comparable to a standard metallic cliché and the cell edge structure has been improved. The cell roughness has been reduced down to 10 nm at the bottom of the cell (Fig. 15).
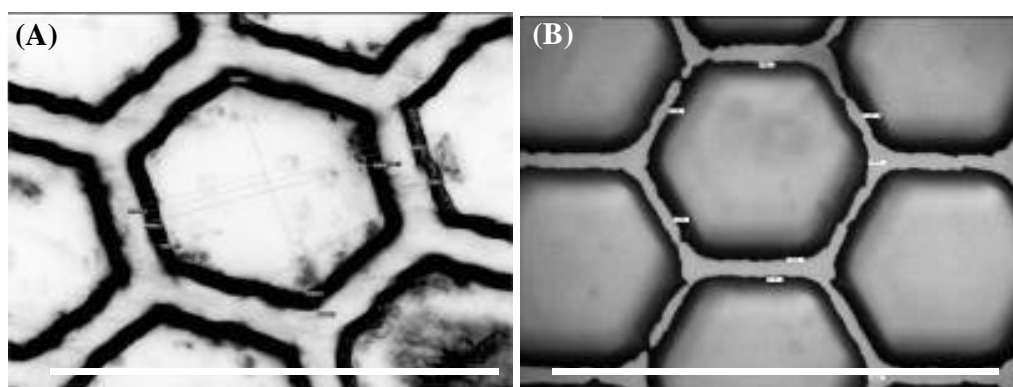
Fig. 14 Plate comparison: metallic (A) vs glass with optimized glass etching (B). Scale bar 100 μm.
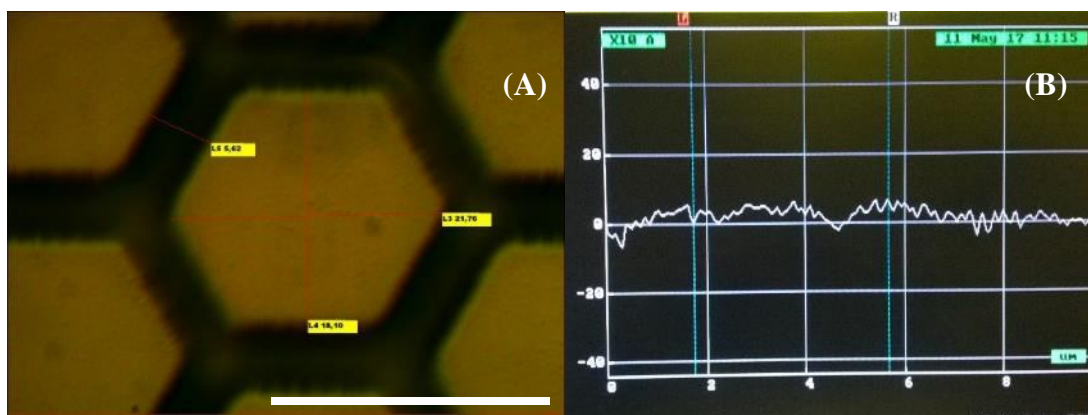
Fig. 15 (A) Bottom of a cell obtained with the optimized process. Scale bar 20 µm. (B) Profile of a cell bottom, the vertical bars show a height difference of 6 nm.

Depending on the ink, the cleaning of the glass cliché (Fig. 16) has been performed with acetone (J.T. Baker, CMOS grade) and isopropyl alcohol, a solvent or a piranha etch, always drying with nitrogen gun.
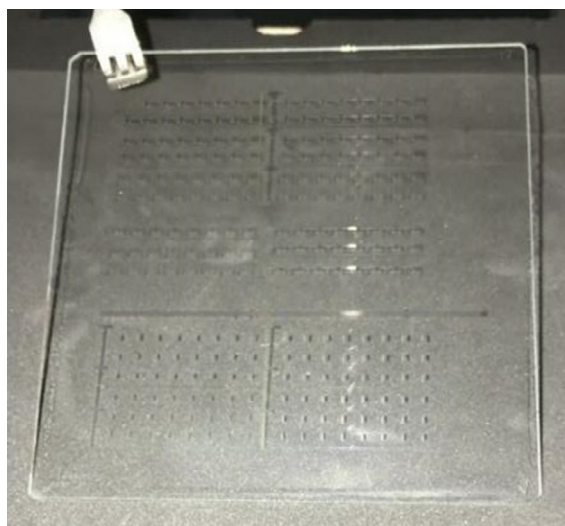
Fig. 16 Optimized glass cliché.

2.2.4. Cliché wettability control

The glass cliché wettability can be easily controlled by functionalizing the surface with a controlled exposition in vapour, such as hexamethyldisilazane (HMDS) or octadecyltrichlorosilane (OTS), depending on the required contact angle. The rationale is to use this functionalization procedure to enhance the ink transfer for the critical interfaces, such as the OSC with the dielectric.

As demonstrated by the contact angle measurements performed (Fig. 17), the cliché wettability decreases if treated with HMDS at increasing temperature. In the optimized procedure, the cliché is

more hydrophobic than the substrate: as already confirmed in literature, this condition is useful in order to increase the transfer to the substrate.[1,10,15,20]
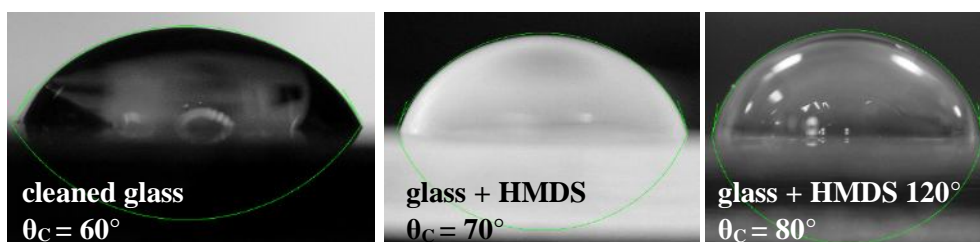
Fig. 17 Contact angle measurements with water on the cliché as is or functionalized.
Reference substrate $\Theta_C = 70°$.

The contact angle measurements have been performed analysing the USB microscope (DigiMicro Prof, dnt) pictures with the support of a plugin of ImageJ, Drop analysis – LB – ADSA.

2.2.5. Layout definition for the test cliché

Using the optimized cliché fabrication procedure, it has been defined a cliché with a peculiar layout for the ink tests (Fig. 18). It has been used to evaluate the most suitable cell for each ink formulation, taking into account different cell shapes and volumes in order to fit the different fluid dynamic properties of the inks.
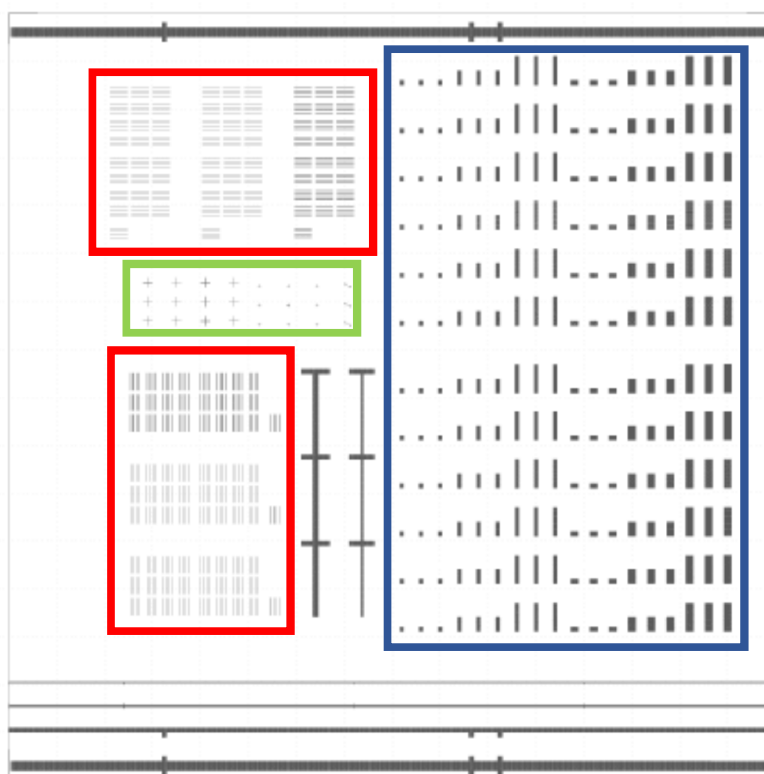
Fig. 18 Test cliché pattern. Red rectangles: S/D ink test; green rectangle: alignment markers; blue rectangle: semiconductor/dielectric ink test.

The cell shape has been defined to improve cell filling from the first edge pinned or, as for continuous lines, to support capillary flow. The gap between cells has been varied between 2 and 4 µm to set the best one, which allows a correct ink rearrangement on the substrate. The cell depth was kept constant, at about 5 µm.

The test cliché included different patterned areas for the semiconductor or dielectric ink testing, the blue area in Fig. 18. They are squares or rectangles, with area $0.2 \div 24$ mm^2. Each zone includes cells with various shapes, as shown in the optical microscopy pictures in Fig. 19, blue contour: hexagonal $100 \div 2400$ µm^2, square $80 \div 1400$ µm^2, rhombic $90 \div 1800$ µm^2.

In order to test the inks for source and drain contacts some lines have been patterned (Fig. 18, red areas). Line widths are of $15 \div 50$ µm and their length is of 1.8 mm. The lines are continuous or composed of cells shaped as rhombus with area $97 \div 3000$ µm^2 or as parallelogram with area $195 \div 2000$ µm^2, angle 40°-50° (Fig. 19, red contour).

An area has been designed for the alignment markers (Fig. 18, Fig. 19, green contour). These markers have to be reported on each cliché in order to check the alignment between different gravure printed layers. Moreover, they have been used for the alignment between the layer deposited by

gravure and the one processed with other techniques, such as the inkjet printing and the laser lithography.
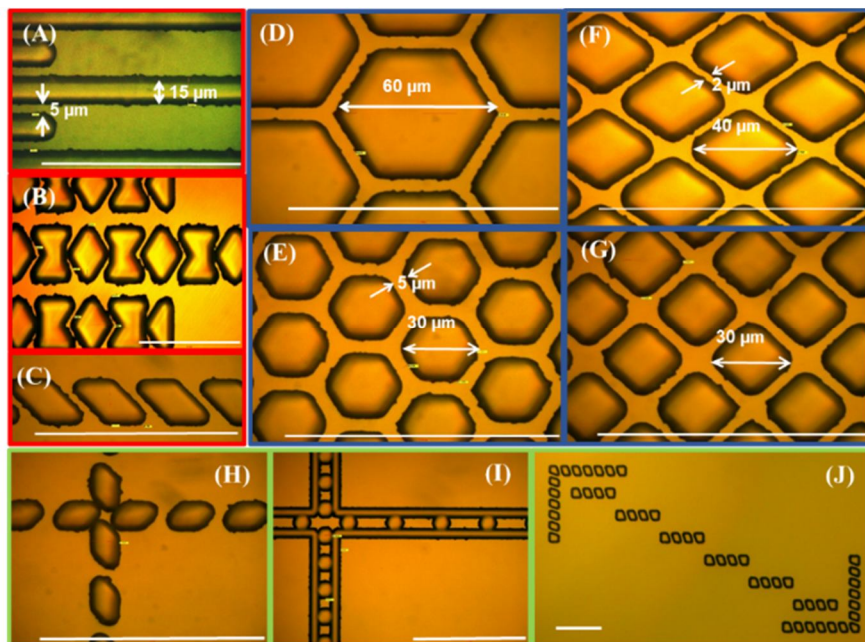
Fig. 19 The different cell shapes in the test cliché. The colours of the figure contour refer to Fig. 18. S/D ink test: (A) continuous lines, (B) rhombic cell lines, (C) parallelogram cell lines; semiconductor/dielectric ink test: (D, E) hexagonal cell, (F) rhombic cell , (G) square cell; (H, I, J) alignment markers. Scale bar 100 µm.

2.3. Doctor blade

Usually the doctor blade material is a metal, such as steel, but this choice has some drawbacks considering the blade influence on the ink capillary flow.

As previously discussed, the high surface energy of the blade reduces the ink transfer to the substrate. Moreover, the drag-out tails are mainly due to the high surface energy of the blades. Since the blades are metallic, their hydrophilicity support the ink flow from the cell to the blade back.[2,3]

The lubrication layer thickness strongly depends on the gap shape, but also on the load applied on the blade and on the blade tip shape or defects. The blade stiffness and angle should not affect it relevantly, to first order.[2,6,7]

At last, the use of metallic blades reduces the cliché durability and produces metallic particle dispersion during wiping, degrading the ink properties.

To work out these problems we have used plastic blades (Fig. 20). These blades have been clamped with a metallic support to increase their stiffness for highly scaled features (e.g. S/D contacts,

OSC). This support would reduce the deformations in the blade body, which could be detrimental during the wiping step.
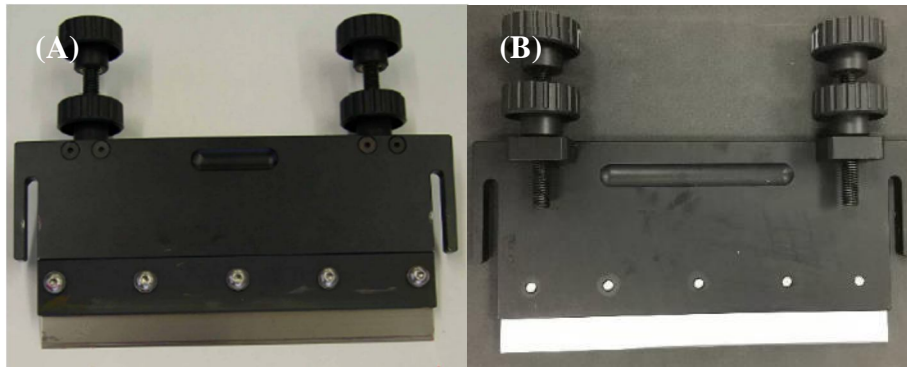
Fig. 20 Metallic (A) vs plastic (B) blades.

References

(1)   Khan, S.; Lorenzelli, L.; Dahiya, R. S. Technologies for Printing Sensors and Electronics Over Large Flexible Substrates: A Review. *IEEE Sens. J.* **2015**, *15* (6), 3164–3185.

(2)   Grau, G.; Cen, J.; Kang, H.; Kitsomboonloha, R.; Scheideler, W. J.; Subramanian, V. Gravure-Printed Electronics: Recent Progress in Tooling Development, Understanding of Printing Physics, and Realization of Printed Devices. *Flex. Print. Electron.* **2016**, *1* (2), 023002.

(3)   Kitsomboonloha, R.; Morris, S. J. S.; Rong, X.; Subramanian, V. Femtoliter-Scale Patterning by High-Speed, Highly Scaled Inverse Gravure Printing. *Langmuir* **2012**, *28* (48), 16711–16723.

(4)   Kitsomboonloha, R.; Kang, H.; Grau, G.; Scheideler, W.; Subramanian, V. MHz-Range Fully Printed High-Performance Thin-Film Transistors by Using High-Resolution Gravure-Printed Lines. *Adv. Electron. Mater.* **2015**, *1* (12), 1500155.

(5)   Subramanian, V.; Cen, J.; de la Fuente Vornbrock, A.; Grau, G.; Kang, H.; Kitsomboonloha, R.; Soltman, D.; Tseng, H.-Y. High-Speed Printing of Transistors: From Inks to Devices. *Proc. IEEE* **2015**, *103* (4), 567–582.

(6)   Kitsomboonloha, R.; Subramanian, V. Lubrication-Related Residue as a Fundamental Process Scaling Limit to Gravure Printed Electronics. *Langmuir* **2014**, *30* (12), 3612–3624.

(7)   Hariprasad, D. S.; Grau, G.; Schunk, P. R.; Tjiptowidjojo, K. A Computational Model for Doctoring Fluid Films in Gravure Printing. *J. Appl. Phys.* **2016**, *119* (13), 135303.

(8)   Lee, S.; Na, Y. Analysis on the Ink Transfer Mechanism in R2R Application. *J. Mech. Sci. Technol.* **2010**, *24* (1), 293–296.

(9)   Campana, D. M.; Ubal, S.; Giavedoni, M. D.; Saita, F. A.; Carvalho, M. S. Three Dimensional Flow of Liquid Transfer between a Cavity and a Moving Roll. *Chem. Eng. Sci.* **2016**, *149*, 169–180.

(10) Dodds, S.; Carvalho, M. da S.; Kumar, S. Stretching and Slipping of Liquid Bridges near Plates and Cavities. *Phys. Fluids* **2009**, *21* (9), 092103.

(11) Sweeney, J. B.; Davis, T.; Scriven, L. E.; Zasadzinski, J. A. Equilibrium Thin Films on Rough Surfaces. 1. Capillary and Disjoining Effects. *Langmuir* **1993**, *9* (6), 1551–1555.

(12) Bornemann, N.; Sauer, H.; Dörsam, E. Gravure Printed Ultrathin Layers of Small-Molecule Semiconductors on Glass. *J. Imaging Sci. Technol.* **2011**, *55* (4), 40201–1.

(13) Brokmann, U.; Sönnichsen, K.; Hülsenberg, D. Application of Micro Structured Photosensitive Glass for the Gravure Printing Process. *Microsyst. Technol.* **2008**, *14* (9–11), 1635–1639.

(14) Clark, D. A. Major Trends in Gravure Printed Electronics. **2010**.

(15) Sankaran, A. K.; Rothstein, J. P. Effect of Viscoelasticity on Liquid Transfer during Gravure Printing. *J. Non-Newton. Fluid Mech.* **2012**, *175–176*, 64–75.

(16) Dörsam, E. Printing Technology for Electronics 5.2 Printing Techniques for Electronics – Gravure Printing. June 28, 2013.

(17) Kahn, B. E. Patterning Processes for Flexible Electronics. *Proc. IEEE* **2015**, *103* (4), 497–517.

(18) Hannes, B.; Vieillard, J.; Bou Chakra, E.; Mazurczyk, R.; Mansfield, C. D.; Potempa, J.; Krawczyk, S.; Cabrera, M. The Etching of Glass Patterned by Microcontact Printing with Application to Microfluidics and Electrophoresis. *Sens. Actuators B Chem.* **2008**, *129* (1), 255–262.

(19) Bahadorimehr, A.; Jumril, Y.; Gebeshuber, I. C.; Dee, C. F.; Majlis, B. Y. Low Cost Fabrication of Passive Microfluidic Devices. In *Nanotechnology (IEEE-NANO), 2010 10th IEEE Conference on*; IEEE, 2010; pp 1007–1011.

(20)   Kang, H. W.; Sung, H. J.; Lee, T.-M.; Kim, D.-S.; Kim, C.-J. Liquid Transfer between Two Separating Plates for Micro-Gravure-Offset Printing. *J. Micromechanics Microengineering* **2009**, *19* (1), 015025.

Chapter 3
Gravure inks

1. Study of electronic organic inks for gravure printing

The main **requirements** for a functional gravure ink are the following:
- processing temperatures compatible with plastic substrates;
- capability to wet the substrate, avoiding hydrodynamic or thin film instabilities;
- solvent orthogonality;
- avoiding contaminations of the underlying materials.[1–3]

To fit these constraints, the study of the fluid dynamic mechanisms involved in gravure printing is required. In the recent years, an intense activity has been carried out by different groups, through a combined computational and experimental approach, focusing on specific parts of the process to understand its physics.[4–16]

In this thesis work, the current knowledge on the gravure printing technique has been applied to refine some inks based on organic materials for the realization of OTFTs.

In particular, for the **dielectric** and the **conductive** materials the approach adopted has been the following.

At first, *preliminary tests* have been conducted printing several inks with the metallic cliché, using standard steel blades with metallic support. These tests have allowed to study the influence of each printing process parameter, to define the most significant that have to be considered in order improve the printing process. Moreover, it has been necessary to study the materials for the ink formulations using a standard gravure printing method, to avoid artefacts due to the developed glass cliché or the plastic blades and to have a reference for further improvements.

Then, a *study of printability* has been conducted considering several electronic ink formulations useful for realizing OTFTs. The most suitable ink formulations and printing conditions have been defined through the evaluation of some significant fluid dynamic parameters and the ink rheological characterization, compared to the printing outcomes obtained using the optimized glass test cliché combined with the plastic blades. Hence, the printing parameters, the wettability differences, the cell shape and pattern have been fitted on the fluid properties.

The organic **semiconductor** formulations have been used without modifications. It has been optimized any process parameter useful in order to improve the *homogeneity* and *continuity* of the printed film.

1.1. Methods

1.1.1. Fluid dynamic parameters

A first evaluation of the fluid dynamic characteristics of the ink during the printing process is feasible considering the variations in several fluid dynamic parameters of the inks. Such preliminary numerical fluid dynamic analysis has allowed to evaluate some issues caused by the unbalance of the forces acting on the fluid during each printing step, as incomplete cell filling, low transferring and poor levelling. The significant fluid dynamic parameters that have been considered for the ink study are the capillary, *Ca*, Bond, *Bo*, Weber, *We*, and Ohnesorge, *Oh*, numbers (all dimensionless), and the characteristic velocity V^* (in m/s), as defined in the following equations.

$$Ca = \frac{\eta U}{\gamma} = \frac{U}{V^*}$$

Eq. 1

$$Bo = \frac{\rho g l^2}{\gamma}$$

Eq. 2

$$We = \frac{\rho U^2 l}{\gamma}$$

Eq. 3

$$Oh = \frac{\eta}{\sqrt{\rho \gamma l}}$$

Eq. 4

$$V^* = \frac{\gamma}{\eta}$$

Eq. 5

where ρ is the ink density, g is the constant of gravitational acceleration and l is a characteristic length.

The principal parameter that has to be taken into account is the ratio between viscous and surface tension forces, **Ca** (Eq. 1), which describes the wettability and is strictly related to the formation of residue volumes and to the ink transfer to the substrate.[4,5] *Ca* is closely correlated to the characteristic velocity V^* (Eq. 5), which is the velocity of the capillary flow moving into and outside the cell.

Ca value strongly influences the filling, wiping and transferring processes.

Filling is reduced at high *Ca*, since viscous forces dominate in this range.[4] In this condition the overall fluid front is too fast and overtakes the cell before the ink is slowly driven into the cell by

weak surface tension forces.[4,5] So, to avoid air entrapment and asymmetric ink filling in the cell, the V^* has to be $>> U$.[4,5]

During wiping, as Ca is reduced the drag-out tail formation increases, since the ink is guided out of the cell, at high V^*, by capillary forces and low U ensures wide timescales for the meniscus generation and movements.[4,5,10,13] On the contrary, the lubrication layer is reduced, since the fluid pressure, and so the gap between the blade and the cliché, increases if driven by high printing speed or viscous forces.[4,5,13]

Transferring process could be divided into three regimes depending on the Ca. At low values ($Ca < 10^{-2}$), it is governed by the differences in wettability, so that the moving contact lines are highly mobile, mainly on the substrate but also on the cell surface in the cliché. The fluid is so driven out of the cell before the capillary break-up.[7,11,12] In this regime, only around 50% of the ink volume in the cell is transferred.[12] At high $Ca > 10^{-1}$, the transfer is dominated by viscous forces, while during all the process the contact lines are practically still.[11,12] The transfer reaches a plateau, corresponding to a quasi-static regime, which varies slowly and increases almost linearly as Ca increases.[11] At intermediate Ca values, the contact lines are still in movement and the neck breaks up before the fluid is pushed up from the cell.[12] For Ca values in the low and intermediate ranges the registration accuracy, defined as the precision in the placement of the printed area, and the pattern fidelity are strongly reduced, since the noticeable slipping of the contact lines causes a movement of the ink on the substrate, reducing the correct pattern positioning and shape.[12] So, either the ink viscosity or the printing speed has to be increased in order to work in the high Ca range, but taking into account the limits imposed by the increase of the lubrication layer.[4,5,7,8,12]

The **Bo** and **We** numbers (Eq. 2 and Eq. 3) take into account the ratio between gravity and inertial forces, respectively, to capillary forces. They have to be minimized to avoid unbalance of the forces acting on the ink during the process. For example, during transferring, if gravity dominates over the interfacial forces the break-up of the capillary neck would not be symmetric. The **Oh** number (Eq. 4) allows to consider the strength of the viscous force influence over the process. Both Bo and Oh are not dependent on U.[9,15]

According to the data reported in literature, it is possible to define a **range of values** for the fluid dynamic parameters convenient for a first definition of a suitable ink formulation. In this working range, the materials should show a suitable balancing of the forces.

Considering $U = 0.01 \div 1$ m/s, $\eta = 50 \div 500$ mPas, $\gamma = 20 \div 30$ mN/m, $l = 1 \div 10$ μm, suitable values of the fluid dynamic parameters are the following.[5,15,17]

- $Ca = 1 \div 5$

- $V^* \gg U$

- $Oh \gg 1$

- $Bo < 10^{-8}$

- $We < 10^{-5}$

It is possible to consider *Bo* and *We* negligible if lower than 10^{-4}, since their values have to be scaled as our characteristic length is tens of microns.[5,18]

For the preliminary fluid dynamic analysis, the inks have been considered to be printed at 0.3 m/s.

1.1.2. Surface tension measurements

To calculate the fluid dynamic parameters it has been necessary to measure some ink physical characteristics, such as the surface tension.

The surface tension has been measured through the classic **pendant drop method** with a home made system. For these measurements a high resolution USB microscope has been used to acquire the images, then analysed using the ImageJ2 plugin Fiji, Pendant drop. This plugin allows to solve the Laplace equation for the drop shape, using a fourth order Runge-Kutta scheme. The drop shape fit obtained can be translated and rotated as a function of some geometrical parameters entered by the user. The result is then optimized for subsequent iterations (Fig. 1).
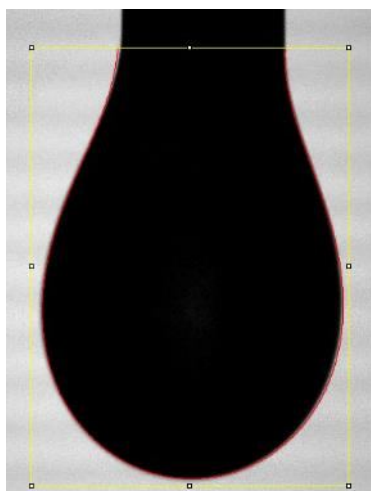
Fig. 1 Image of an ink drop with the fitting curve.

In Tab. 1 are reported the values obtained for some standard materials, used to verify the method reliability, and for some organic conductive ink formulations. For further material specifications, refer to Paragraph 1.2.

Material	γ [mN/m]
IPA	17
Triton X- 100	23
ST	24
H_2O	74
SV3:IPA 4:1	20
SV3:ST 4:1	36
SV3:H_2O 1:5 + Triton X-100 1%v/v	30
SV3:H_2O 1:10 + Triton X-100 1% v/v	31
SV3:H_2O 1:20 + Triton X-100 1% v/v	34
SV4:H_2O 1:10 + Triton X-100 1% v/v	31

Tab. 1 Surface tensions for some solvents and inks.

From these measurements, some observations regarding the efficiency in reducing the surface tension with some solvents or additives can be pointed out. The best results have been achieved using small amounts of Triton X-100 or diluting the materials with IPA. Hence, these materials have been chosen for further investigations.

1.1.3. Rheological measurements

The instrument used for the rheological measurements was a Physica rheometer MCR 301 Anton-Paar, with a cone/plate geometry, 75 mm diameter, 1° angle. All rheological measurements have been performed at 21°C, without pre-shearing and stirring the sample at 500 rpm for 1 h before the measurements, to better simulate the printing conditions.

It is noteworthy that the viscosity has been obtained through rheological measurements, that allow to quantify the ink viscosity while subjected at different shear rates. This procedure is required since the shear on the ink is in the order of $\sim 10^4 \div 10^6$ s^{-1} during gravure printing.[5] For a Newtonian-like ink, viscosity is independent of the shear rate, while for a non-Newtonian pseudoplastic ink, with shear thinning behaviour, the viscosity varies as a function of the shear rate.[19,20] However, at very high shear rates, even for Non-Newtonian fluids the viscosity approaches asymptotically a constant value (the so called second Newtonian range), since the molecules have been already oriented by the shear.[20] Considering the shear imposed by the gravure process and the described fluid dynamic aspects, the relevant viscosity for our analysis is that measured at high shear rates in the second Newtonian range.[5,20]

In addition, the rheological analyses have allowed to understand more deeply the fluid dynamic behaviour of the inks.

Possible instabilities in the fluids as a function of the applied shear rate have been investigated. It has been measured the shear stress as a function of an increasing and then decreasing shear rate, obtaining the **up-down flow curves**. The viscosity is calculated from the shear stress considering specific rheometer parameters, obtaining the **viscosity curves**, which can be studied to analyse the viscosity variations as a function of the shear rate.

In order to study the material elastic characteristics, the material storage and loss moduli variations have been measured performing **frequency sweep** tests at constant temperature and strain. This test consists in a stepwise increasing of the strain frequency, at any frequency step the two resulting values of the phase angle δ and the complex modulus G^* are measured. The values of the *shear storage moduli G'* and of the *shear loss moduli G''*, respectively the in-phase elastic reversible and the out-of-phase viscous irreversible component of the oscillatory flow, are calculated considering that $G^* = G' + \mathrm{i}\, G'' = G^* \cdot \cos\delta + \mathrm{i}\, G^* \cdot \sin\delta$. The G' and G'' variations as a function of the angular velocity ω define the elastic properties of the fluid under test.[21]

Furthermore, the *yield point* has been evaluated performing **creep tests**.[21] A shear stress is instantaneously applied and the strain is measured as a function of time. The yield point value is the shear stress at which a material turns into a flowing liquid and the network collapses due to the applied forces.[20] Its value is linked to ink spreading on the substrate, since it defines the resistance to flow of the ink at low shear rates.

1.1.4. Procedures for the printing tests

1.1.4.1. Preliminary tests

To conduct the preliminary tests, the metallic cliché has been used, combined with standard steel blades with metallic support. If not otherwise specified, printing speed has been kept at 0.6 m/s, to obtain the highest ink transfer, pressure dial 5.98. This choice has been due to the observation that the printing speed variations have not shown influences on the process other than the increase in the ink transfer to the substrate. The roll pressure and the angle between the printing cliché and the doctor blade have been kept constant during all the experiments.

The substrate used has been a heat stabilized low roughness 100 µm thick PEN (DuPont Teijin Teonex® Q65HA), it has been cleaned in US bath with acetone 2 min and IPA 3 min.

The overall process has been conducted in a cleanroom environment under hood.

1.1.4.2. Study of the printability

The run of printing tests to evaluate the printing properties of several ink formulations has been conducted using the optimized glass test cliché. If not otherwise specified, all the inks have been printed at printing speed 0.3 m/s, pressure dial 5.98, performing a pre-treatment on the cliché exposed at HMDS vapours for 15 min after a pre-heating at 120°C. The roll pressure and the angle between the printing cliché and the doctor blade have been kept constant during all the experiments. The plastic blade chosen are the following:

- PEDOT:PSS formulations and p-type semiconductor: E10/25/22 degree bevelled edge profile (Esterlam Blades) with metallic support

- dielectric: E10/25/ST with step lamella profile (Esterlam Blades)

- n-type semiconductor: E600/25/22 degree bevel edge profile (Esterlam Blades) without support or E10/25/22 degree bevelled edge profile (Esterlam Blades) with metallic support.

As substrate a heat stabilized low roughness 100 µm thick PEN (DuPont Teijin Teonex® Q65HA) has been used, it has been cleaned in US bath with acetone 2 min and IPA 3 min. All curing temperatures have been kept below 120°C to avoid substrate shrinkage.

The overall process has been conducted in a cleanroom environment under hood.

1.2. Ink formulations

1.2.1. Organic dielectric ink

For the dielectric ink two different formulations based on the fluoropolymer Cytop™ (CTL 809M, AGC Chemicals) have been analysed, for CYTOP_A pure, for CYTOP_B diluted 3:1 with its solvent, (CT-Solv180, AGC Chemicals).

1.2.2. Organic conductive ink

1.2.2.1. Preliminary tests

For the organic conductive ink different compositions based on poly(3,4-ethylenedioxythiophene) : polystyrene sulfonate (PEDOT:PSS) have been studied. The PEDOT:PSS formulations have been based on two screen printing pastes, Clevios™ SV3 or SV4 and on an inkjet ink (Clevios™ PH 510), all purchased by Heraeus. The additives, TritonX-100, Glycerol and dimethyl sulfoxide (DMSO), have been purchased from Sigma-Aldrich and used without further purifications. Annealing has been performed in oven at 100°C for 15 min, variations between 80°-120°C up to 30 min have not shown significant differences in the final film morphology.

Several formulations have been taken into account for the preliminary tests, reported in Tab. 2.

Name	Bulk material	Solvent	Additives (%v/v)
3A	SV3	-	-
3B	SV3	IPA 4:1	-
3C	SV3	IPA 4:1	Triton X-100 0.1%
3D	SV3	IPA 4:1	Triton X-100 0.5%
3E	SV3	IPA 4:1	DMSO 4%
3F	SV3	IPA 4:1	DMSO 6%
3G	SV3	IPA 4:1	DMSO 10%
3H	SV3	IPA 4:1	DMSO 6% - Triton X-100 0.5%

Tab. 2 Organic conductive ink formulations for the preliminary tests with the metallic cliché.

1.2.2.2. Study of the printability

The formulations for the ink study for the realization of OTFTs are detailed in Tab. 3. The ink formulations have been chosen as the most significant to understand the relations between the ink characteristics and its printability. The main materials have been mixed with the solvent and additives with gentle magnetic stirring to avoid bubbles formation for 24 h in nitrogen glove box. PEDOT_A and PEDOT_B are based on a paste diluted to decrease both the viscosity and the surface tension, further added with a conductivity enhancer and a surfactant to reduce the surface tension. PEDOT_B composition is refined with the addition of a plasticizer. PEDOT_C is a highly conductivity paste just diluted with its solvent (ST, Heraeus) to reduce the viscosity. PEDOT_D is a low viscosity material, added with DMSO, with surface tension comparable to the other PEDOT formulations.

Name	Bulk material	Solvent	Additives (%v/v)
PEDOT_A	SV3	IPA 4:1	DMSO 6% - TritonX-100 0.5%
PEDOT_B	SV3	IPA 4:1	DMSO 6% - TritonX-100 0.5% - Glycerol 5%
PEDOT_C	SV4	ST, Heraeus 4:1	-
PEDOT_D	PH510	-	DMSO 4%

Tab. 3 Organic conductive ink formulations for the ink study for OTFT realization.

It has to be noted that formulations 3H and PEDOT_A are the same material. Annealing has been performed in oven at 100°C for 15 min, variations between 80°-120°C up to 30 min have not shown significant differences in the final film morphology.

1.2.3. Organic semiconductor inks

As semiconductors two polymeric material have been chosen in order to ensure low variability among the devices throughout the sample, as discussed in the first chapter.[22,23] As p-type OSC has been used the SP400, provided by Merck, while as n-type the N2200 by Polyera.

2. Organic dielectric ink

2.1. Preliminary tests

To test if the dielectric preserves its electrical characteristics when deposited through the gravure printing technique, **MIM** devices have been realized (Fig. 2).
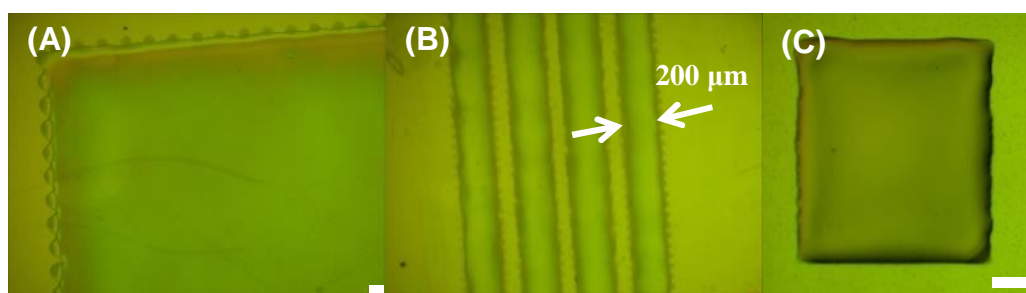
Fig. 2 (A-B) Gravure printed dielectric. (C) MIM devices to test the printed dielectric. Scale bar 100 μm.

The procedure is the following:

1. Aluminium thermally evaporated, 25 nm thick.
2. Dielectric gravure printing, using the standard metallic cliché, CYTOP_A formulation, printing speed 0.12 m/s to avoid possible Al cracking due to mechanical stresses during the printing process.
3. Annealing 1 h at 100°C in vacuum oven.
4. Top contact deposition through inkjet printing, same procedure as reported in Chapter 4, Paragraph 2.2.
5. Annealing 80°C overnight in oven.

The top contact area is a square with side 1 – 0.75 – 0.5 mm. The resulting dielectric thickness has been measured around 90 nm, 150 nm, 300 nm and 400 nm, depending on the engraving resolution.

In Fig. 3 are reported the results for a 0.5 mm side top contact, measured with two different ramp rate.
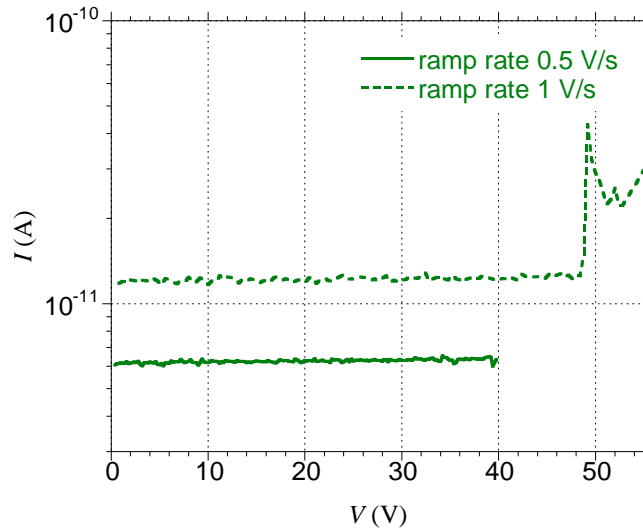
Fig. 3 I-V characteristics of the MIM realized with gravure printed dielectric and top contact inkjetted. Thickness 400 nm, side contact 0.5 mm.

The data reported in Fig. 3 green dotted line, are well comparable to those reported in Chapter 1 Fig. 19, obtained with the dielectric spin-coated on silicon, with top contact in Al, considering the same device area, dielectric thickness and ramp rate.

The breakdown voltage is around 50 V, corresponding to a dielectric strength $E_{ds} \approx 1$ MV/cm, in agreement with the specification reported for this material and the previously obtained values.

2.2. Study of the printability

Concerning the two dielectric formulations considered for the printability studies, the values of the fluid dynamic parameters calculated are reported in Fig. 4.
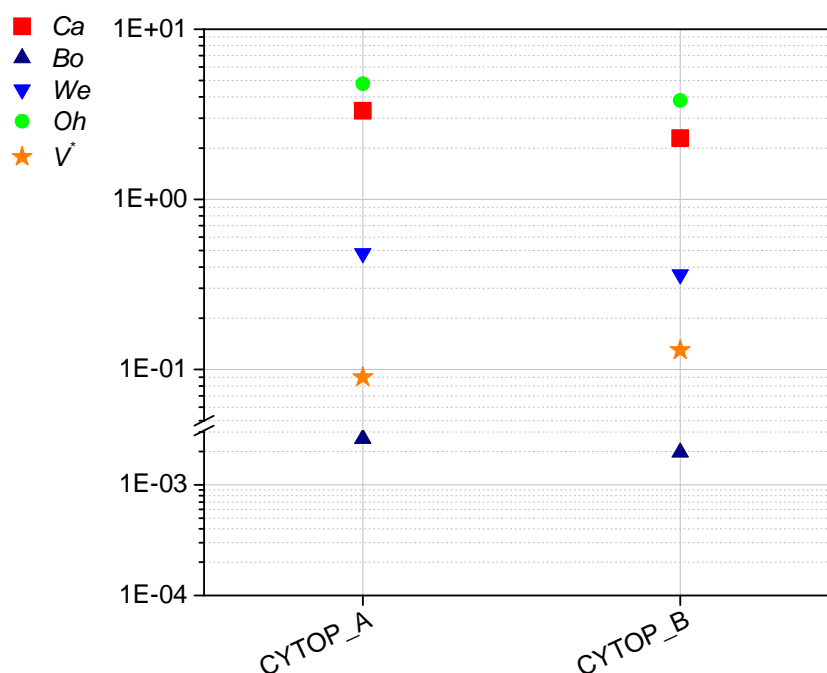
Fig. 4 Main results of the preliminary fluid dynamic analysis for the dielectric formulations. The V^* values reported are in m/s. Printing speed $U = 0.3$ m/s.

The **fluid dynamic analysis** has shown that they have characteristic velocities V^* lower than the printing speed $U = 0.3$ m/s, a condition that could induce air entrapment in the cells. However, during the printing process the viscosity forces should be more relevant compared to the surface tension and inertial ones, as expected from the high *Ca* and *Oh*, around 3 and 4 respectively for both formulations. This prevalence should improve the ink transfer to the substrate and counterbalance a low filling, resulting in a good printing outcome without further modifying the ink viscosity or surface tension. As indicated by the high *Bo* values (in the order of 10^{-3}) gravity forces cannot be neglected. That should result in a reduced transfer, however the influence of the inertial forces should counterbalance this issue, as highlighted by the high *We* values.[24] The CYTOP_B formulation could result in a more uniform film compared to CYTOP_A, since, as discussed before, the ink spreading on the substrate is inhibited by viscous forces and by a high solvent evaporation rate, that further increases the ink viscosity.[4]

Rheological measurements have been performed to better understand the ink fluid dynamic characteristics. Fig. 5 A shows that the *viscosity curves*, as a function of the shear rate, are almost constant for both dilutions (flow curves in Fig. 5 B), indicating that they are both Newtonian-like fluids. These formulations have a *yield point*, if present, under the instrumental limit of detection (10^{-3} Pa). So, it was not expected to obtain very high resolution patterns.
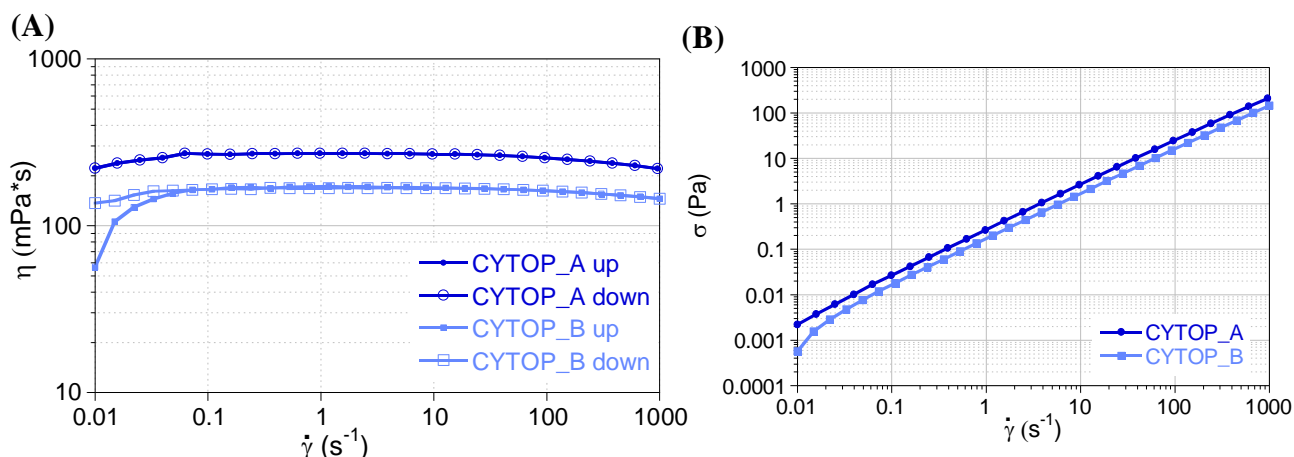
Fig. 5 CYTOP_A and CYTOP_B up-down viscosity (A) and flow (B) curves.

The previous analyses have been confirmed by the **printing tests**, performed using as substrates a bare PEN sheet or an OSC layer gravure printed on the PEN foil (Fig. 6, Fig. 7). For both inks printed on PEN, using different cell geometries and volumes, pattern dimensions and printing speed, there are no significant differences in film continuity and homogeneity and the drag-out tails have not been observed (Fig. 6).
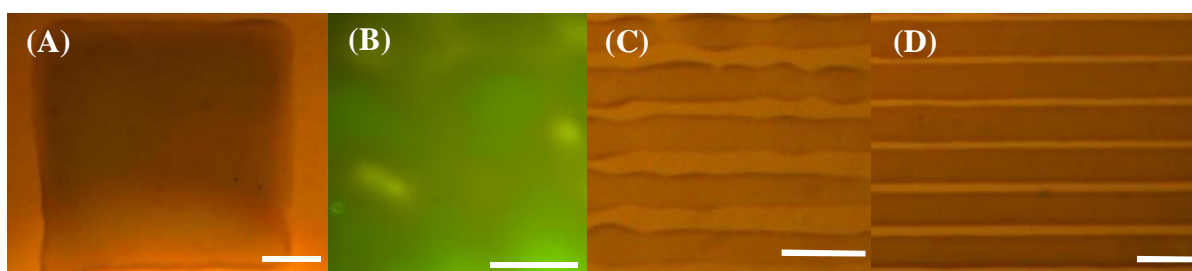
Fig. 6 CYTOP_A printing outcomes with different cell shapes or printing speed: (A) hexagonal, *U* = 0.3 m/s, (B) hexagonal, *U* = 0.48 m/s, (C) parallelogram, (D) rhombic. Scale bar 100 µm.

This could be due to the low yield, which allows a liquid-like ink flowing, supporting the filling and enhancing the levelling, perhaps sustaining the single drops spreading. The low surface tension, around 20 mN/m, combined with the low yield could justify the absence of drag-out residues, since the ink does not wet the blade, so it is not drawn on the blade back by capillary forces.
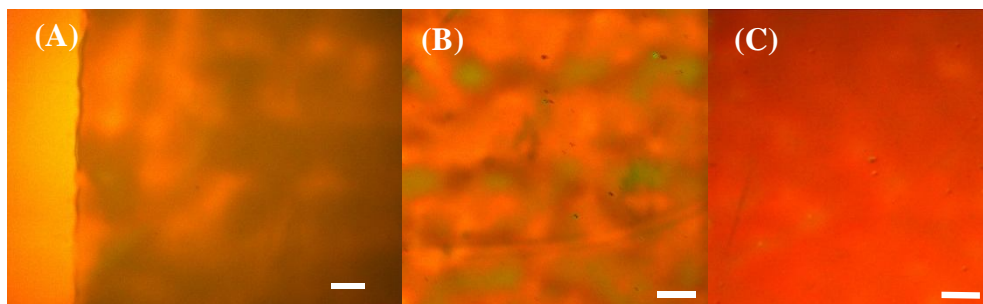
Fig. 7 Dielectric inks printing test outcomes, hexagonal cells: CYTOP_A on PEN (A) and on OSC (B), CYTOP_B on OSC (C). Scale bar 100 μm.

Using a suitable pattern design, the printed area edges are straight and the area definition is acceptable for OTFT application (Fig. 7). The film homogeneity on the OSC (Fig. 7 C-D) is improved for the less viscous formulation, according to the fluid dynamic parameters analysis. The good homogeneity obtained with these materials appears to be in contrast with the tendency of a Newtonian gravure ink to produce inhomogeneous layers, with poor registration accuracy and low thicknesses.[12,25] However, it has to be considered that usual gravure printed Newtonian fluids have low concentration, with viscosity and surface tension similar to their solvent.[25] On the contrary, Newtonian-like dielectric inks have been used, which have viscosity in the order of hundreds of mPas and low yield point. In these conditions, it is possible to obtain a suitable printed pattern by adjusting the wettability differences among ink, cliché, blade and substrate. Indeed, the printing outcomes show that it has been possible to obtain continuous films over large areas on particularly hydrophobic materials and to achieve high thicknesses, homogeneity and acceptable resolutions.

In the following graph (Fig. 8), the dielectric **thickness trend** as a function of its dilution and of the cell depth is shown. It has been considered the same hexagonal cell shape. The cell volume is 7642 and 24192 μm^3, the aspect ratio 0.11 and 0.19, respectively for cell depth 4.9 and 10.7 μm.
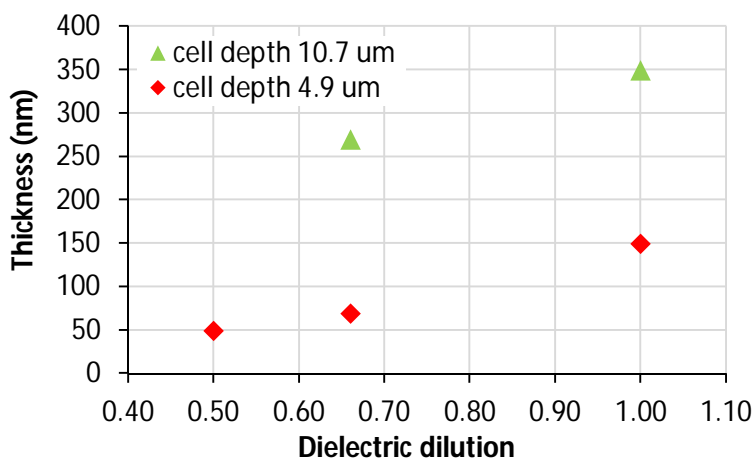
Fig. 8 Thickness of a dielectric gravure printed film as a function of its dilution and of the cell depth.

It has been highlighted that the thickness varies as a function of the dilution following an exponential trend. Increasing the cell depth the quantity of thickness increase is dependent on the dilution.

3. Organic conductive ink

3.1. Preliminary tests

All the ink formulations have been stirred for long time to obtain a homogeneous material. In Fig. 9 are reported the microscope images of a typical *distribution of particles* in a material before and after the stirring procedure.
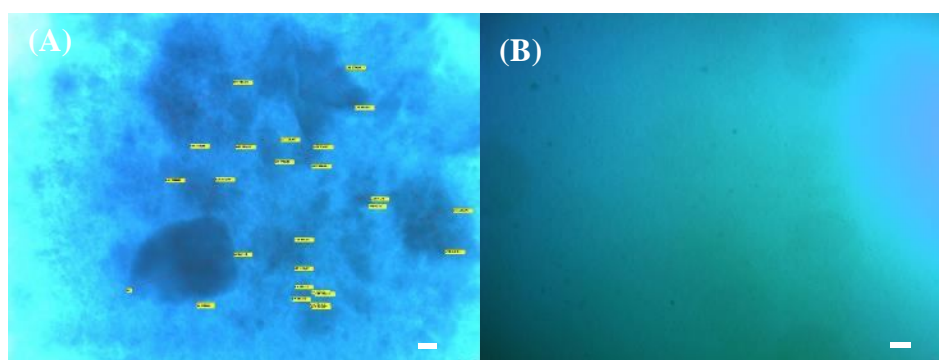
Fig. 9 Optical microscopy images of the typical particle size in an ink before (A) and after (B) the stirring procedure. Scale bar 100 µm.

The distribution of particle dimensions has not shown significant variations after 3 months, so the stirring procedure can be considered as not reversible in the mid-term. Ink gelling has occurred, nevertheless 1 h stirring before usage has been sufficient to regain the optimized ink features.

According to the fluid dynamic of the gravure printing process reported above, it is necessary to balance the forces acting on the ink during the process. The main issue is the balance between the viscous and the surface tension forces acting in the ink. To evaluate how the material *dilution* influences this aspect, the paste has been printed as is or diluted with IPA, a low surface tension solvent, formulations 3A and 3B respectively. The optical microscopy images of the printed films before and after the annealing are reported in Fig. 10.
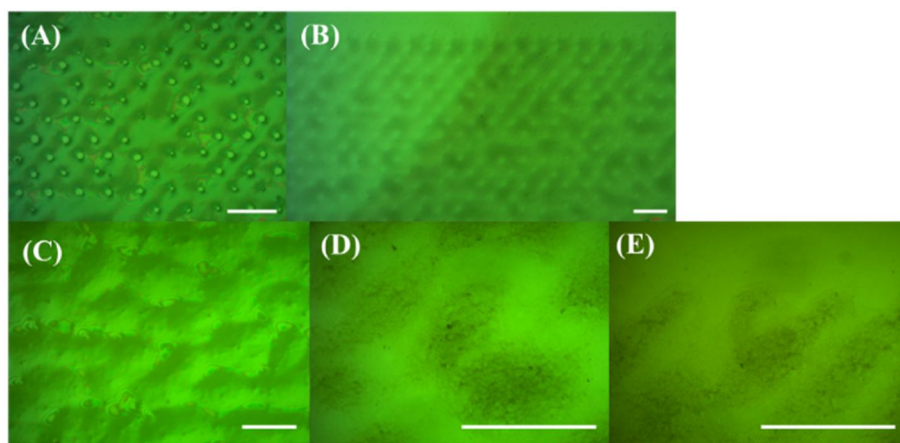
Fig. 10 Optical microscopy pictures of the inks: 3A before (A) and after annealing (B), 3B before (C) and after annealing (D-E). Scale bar 100 μm.

The 3A formulation is too viscous, the film is not continuous after the printing (Fig. 10 A) because the material is not able to rearrange itself on the substrate after being transferred from the cliché. Also after the annealing (Fig. 10 B) it has been observed the presence of discontinuities. The diluted formulation, 3B, shows better printability, allowing to obtain a continuous film after the printing, but strongly not homogeneous (Fig. 10 C). Due to this issue, the disjoining forces are too high during the levelling step, so inducing the formation of holes in the film, Fig. 10 D (hole size ≈ 8 μm). The line edges are strongly undulated, even when printed following the printing directions (Fig. 10 E), pointing out the poor printability of this material. Both formulations are not stable in time and do not ensure good repeatability of the results.

To improve the printability, a *surfactant* has been added to the formulation. It allows to reduce the ink surface tension, even when added in small quantities, in order to improve the ink wettability towards the substrate. It also enhances the material dispersion and stability. In Fig. 11 are reported the effects on the printing outcomes of the addition of different concentration of Triton X-100 to the diluted formulation 3B.
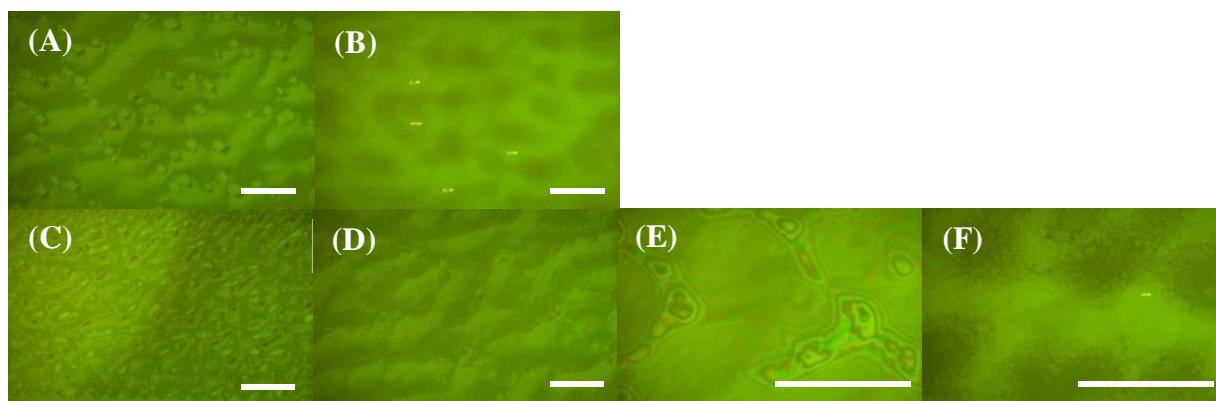
Fig. 11 Optical microscopy pictures of effect of adding different Triton X-100 concentrations in the ink: 3C before (A) and after annealing (B), 3D before (C-E) and after annealing (F). Scale bar 100 μm.

The addition of a lower concentration of surfactant, formulation 3C, has worsened the material printability, resulting in a less homogeneous film. The holes in the film after the annealing are around 13 μm (Fig. 11 B). A higher concentration, formulation 3D, improves the material transferring to the substrate as shown in Fig. 11 C, while the forces acting during the levelling are similar to 3B formulation, Fig. 11 D-E. The hole sizes in the final film are around 7 μm (Fig. 11 F). Both formulations have shown more reproducibility in the results and good stability in time, stirring the solution at 500 rpm for 1 h before the printing.

To enhance the ink conductivity, usually DMSO is added to the formulation. The effects of this material at different concentrations on a 3B formulation are reported in Fig. 12.
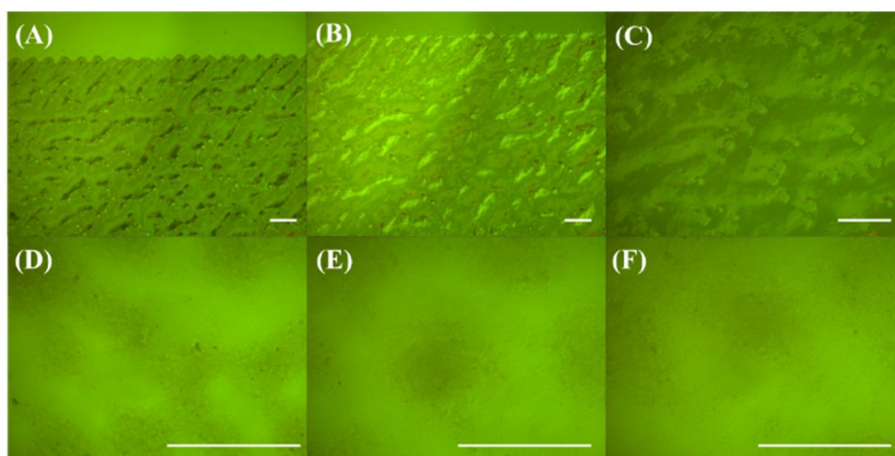
Fig. 12 Optical microscopy pictures of the effect of adding different DMSO concentrations in the ink: 3E before (A) and after annealing (D), 3F before (B) and after annealing (E), 3G before (C) and after annealing (F). Scale bar 100 μm.

The ink printability has worsened for the formulations 3E and 3G compared to the 3D formulation. The formulation 3F has shown the best results as the addition of DMSO has not

influenced negatively the material printability. It has been pointed out that even small variations in the amount of conductivity enhancer can strongly affect the ink printability.

To study the influence of each additive or solvent on the electrical properties of the printed film, an electrical characterization has been performed. Several **resistors** have been realized printing lines of each formulation on a PEN substrate. To contact the material silver electrodes have been realized. **Electrical characterization** has been performed using the Suss PM5HF Analytical Probe Station equipped with a Hewlett Packard HP 4145B semiconductor parameter analyser.

In Fig. 13 are reported the *sheet resistances* of the organic conductive ink formulations. All the films have been annealed for 15 min at 80°C, except the ones printed with the 3A ink.
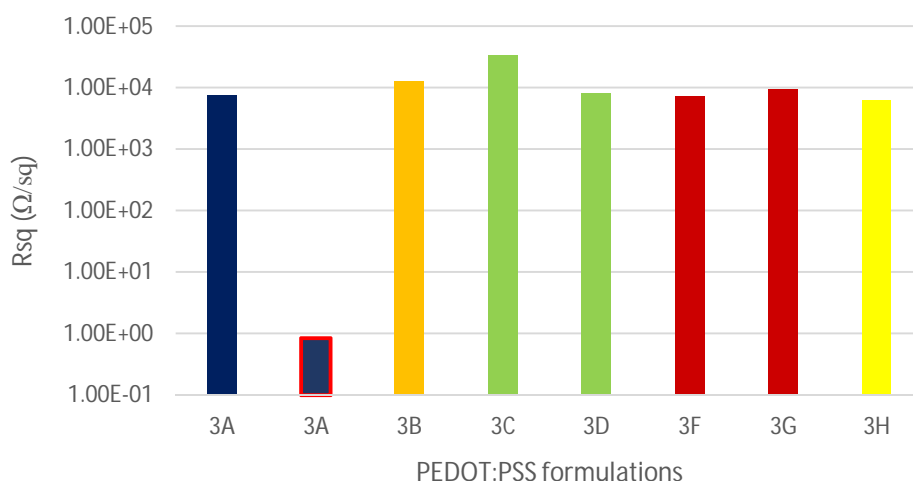
Fig. 13 Sheet resistance for several ink formulations. Blue: pure material annealed at 100°C or 130°C (red contour); orange diluted; green addition of Triton X-100; red addition of DMSO; yellow addition of Triton X-100 and DMSO.

The differences in sheet resistances among the modified ink formulations are negligible and can be attributed to the discontinuities in the printed film. It has been highlighted that the main influence on the material conductivity is due to the *annealing temperature* (Fig. 13, 3A formulation).

In Fig. 14 are reported the printing outcomes for the 3H formulation. The printed film shows discontinuities, after the annealing the holes are around 10 μm of diameter.
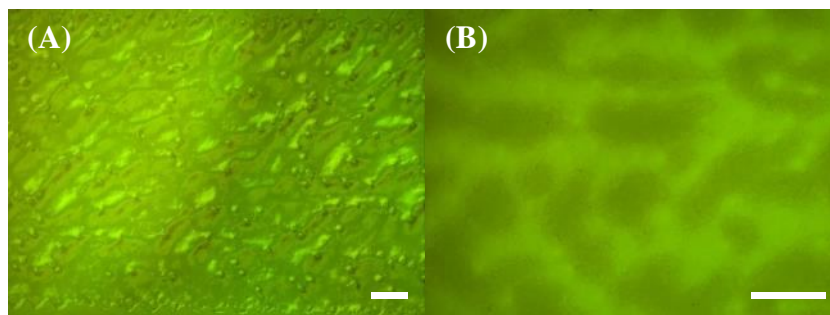
Fig. 14 3H before (C-E) and after annealing (F). Scale bar 100 μm.

3.2. Study of the printability

The values of the fluid dynamic parameters calculated for the ink formulations considered for the printability studies are reported in Fig. 15.
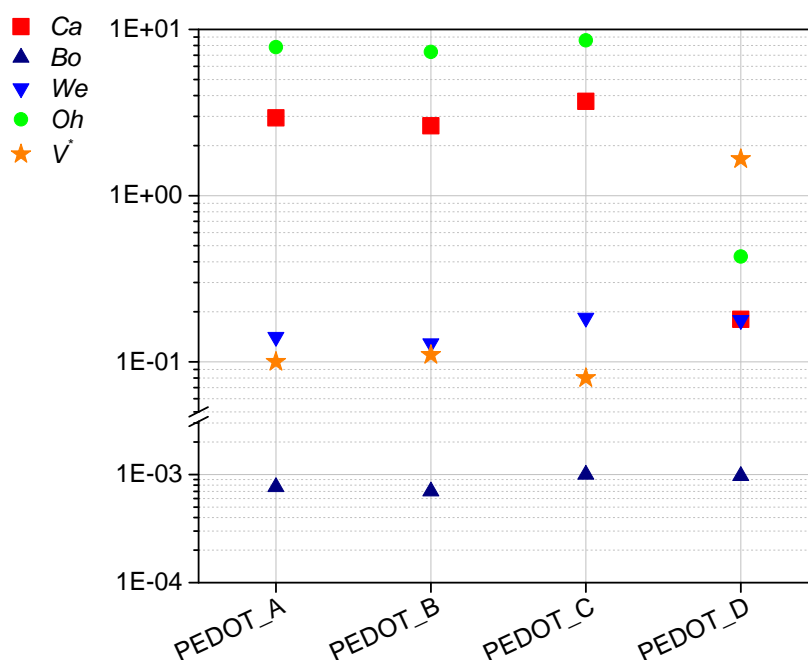
Fig. 15 Main results of the preliminary fluid dynamic analysis for the organic conductive ink formulations. The V^* values reported are in m/s. Printing speed $U = 0.3$ m/s.

The numerical **fluid dynamic analysis** of PEDOT:PSS formulations shows that Ca values for the PEDOT_A, PEDOT_B and PEDOT_C are in the acceptable range for printing, resulting in the range 2.6÷3.7, although a thicker lubrication layer was expected for increasing Ca-values, in particular for PEDOT_C formulation.[5,17] The behaviour of these inks is largely dominated by the viscous forces over the surface tension ones, as highlighted by the high values of Oh and Ca. This prevalence should result in a weaker dependence on the wettability differences, while the rheological properties of the materials were expected to strongly affect the ink behaviour. Instead, it has to be

68

remarked that *Oh* and *Ca* values of PEDOT_D are at least one order magnitude lower compared to the other formulations. In these conditions the surface tension and the inertial forces will dominate PEDOT_D behaviour and the transfer has supposed to be widely reduced.[5,15] It has also to be noticed that it has a high V^*, around 1.66 m/s, so capillary flow is quite fast and it should not show asymmetric cell filling. For PEDOT_C and PEDOT_D formulations, gravity forces cannot be neglected, as presumed from *Bo* values in the order of 10^{-3}. From the *We* values, the inertial force influence was supposed to counterbalance and avoid any reduction in the transfer for these two formulations.[24] According to this analysis, it was expected to have good printability for PEDOT_A, PEDOT_B and PEDOT_C formulations, with increased lubrication layer for the PEDOT_C. Furthermore, the printability conditions of the inks are related to the rheological properties of the materials, rather than to their wettability differences with the cliché, the blade and the substrate.

A run of **printing tests** has been conducted for each PEDOT:PSS based ink to optimize the printing process conditions. The *U* has been chosen at an intermediate value of 0.3 m/s in order to reduce the formation of residue volumes without modifying the ink formulation and to avoid excessive lubrication layer formation. The drag-out tail drawbacks have been limited with the proper cell pattern spacing, to avoid short circuits between the electrodes. Better film morphology has been observed decreasing the gap between two adjacent cells down to 2 µm, with increased continuity for all formulations. For higher gap widths, hole formation occurs in the film in the area corresponding to the wide gap at the intersection among several cells. This behaviour can be attributed to the higher disjoining pressure gradient due to the higher difference in the layer thickness transferred from the cell and the gap surface.
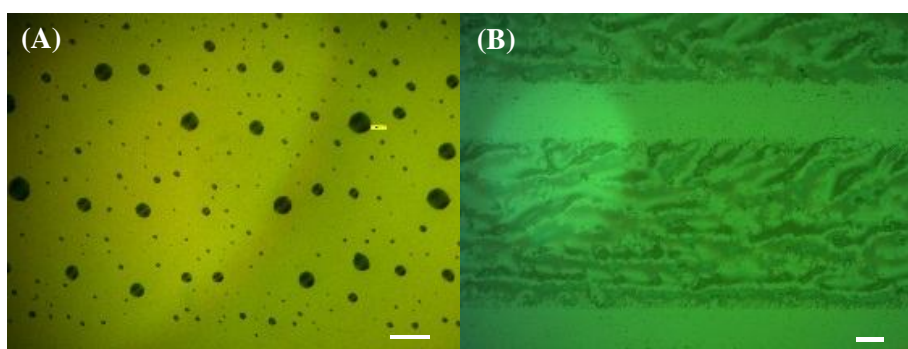
Fig. 16 PEDOT:PSS printing outcomes. PEDOT_D (A) and PEDOT_C (B). Scale bar 100 µm.

Concerning the different formulations, as expected from the fluid dynamic analysis, it has been confirmed (Fig. 16 A) that PEDOT_D is not suitable for gravure printing. PEDOT_A, PEDOT_B and PEDOT_C have not shown significant differences in pattern formation modifying the cliché or

substrate wettability, as anticipated by the fluid dynamic parameters. Despite PEDOT_C has quite good fluid parameters and even if, as supposed, the transfer is not affected by the gravity influence, this ink has shown poor printability (Fig. 16 B). The resulting film is not homogeneous and not well defined. The significant lubrication layer observed has confirmed the preliminary fluid dynamic analysis expectations. Better results have been obtained with PEDOT_A and PEDOT_B, as shown in Fig. 17 A-D and Fig. 17 E-H.
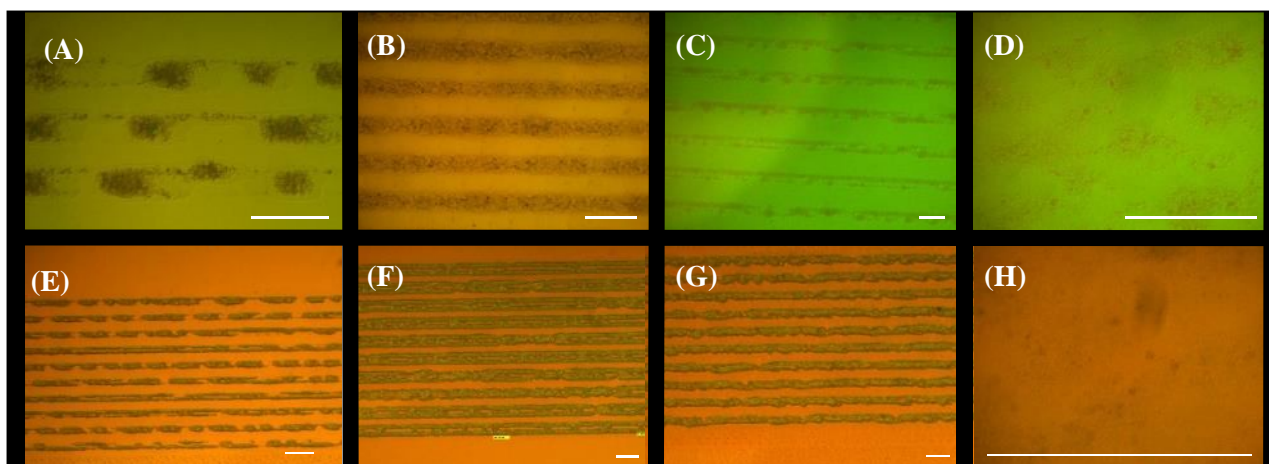
Fig. 17 PEDOT:PSS printing outcomes. PEDOT_A (A-D) and PEDOT_B (E-H): lines without cells (A,E), with rhombic cells (B,F), with parallelogram cells (C,G) and film morphology (D,H). Average film thickness PEDOT_A ≈ 25 nm, PEDOT_B ≈ 35 nm. Scale bar 100 μm.

It can be noticed that a significant different behaviour has been observed between the two formulations depending on the cell shape. For both inks, it has been possible to find a shape able to fit the ink properties in order to obtain quite straight edges and a continuous and rather homogeneous film. In particular, the most suitable cell shape has been identified for PEDOT_A as the rhombic one, while for PEDOT_B as the parallelogram one. It is noteworthy that the proper cell shape is different for the two formulations, although they have similar fluid dynamic parameters.

It has to be remarked that the printing outcomes obtained are different while using the optimized or the standard gravure printing configuration. Usually, an improvement in homogeneity and continuity in the final film has been observed using the modified system (for direct comparison

Fig. 14 vs Fig. 16 B, obtained in the best printing conditions for each system).

To understand the particular behaviours of PEDOT_A, PEDOT_B and PEDOT_C, a **rheological characterization** has been performed.
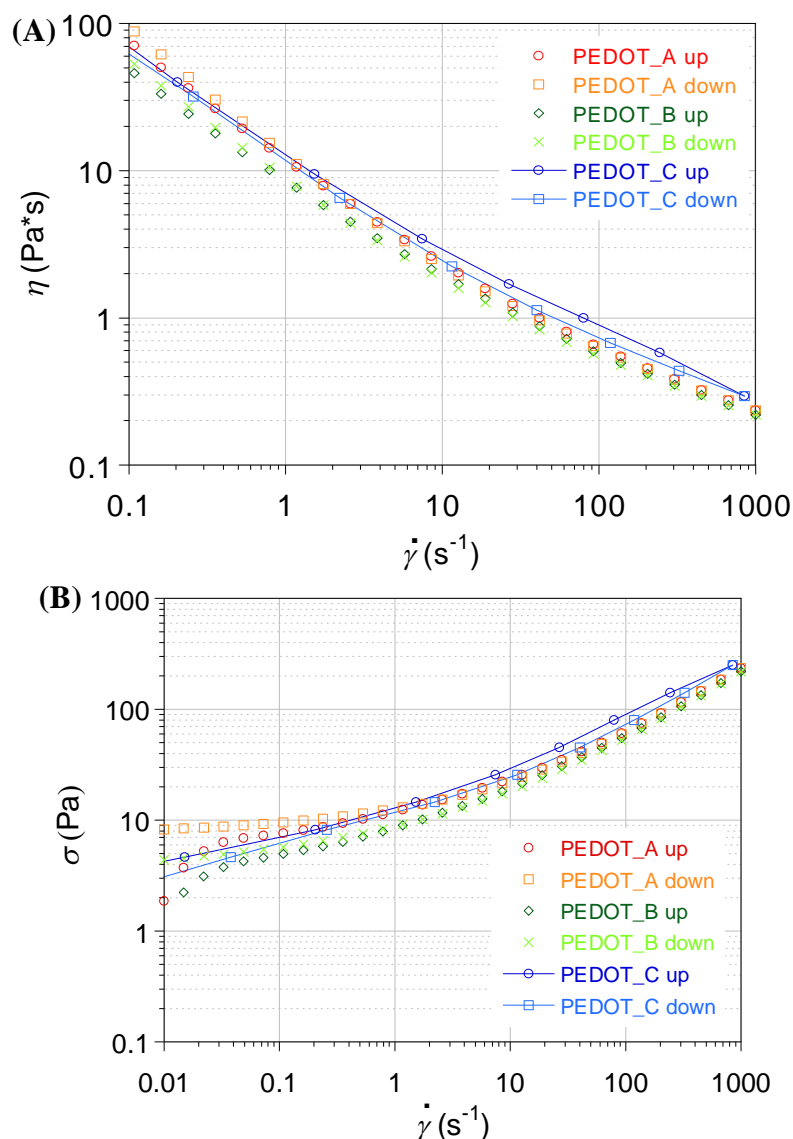
Fig. 18 PEDOT_A, PEDOT_B and PEDOT_C up-down viscosity (A) and flow (B) curves.

In Fig. 18 A the viscosity curves (flow curves in Fig. 18 B) show that these inks become thinner as the shear rate increases. They are non-Newtonian pseudoplastic fluids with yield point.[20] It is evident that PEDOT_C has a significant thixotropic loop, since the down and up curves do not coincide. This occurs mainly at high shear rates that correspond to the gravure range of work.[20] The cause of the PEDOT_C poor printability could depend on this intrinsic instability in the material, due to the time the fluid needs to recover its 3D network after a shear stress, which easily breaks the weak hydrogen or ionic bonds of the structure.[20]
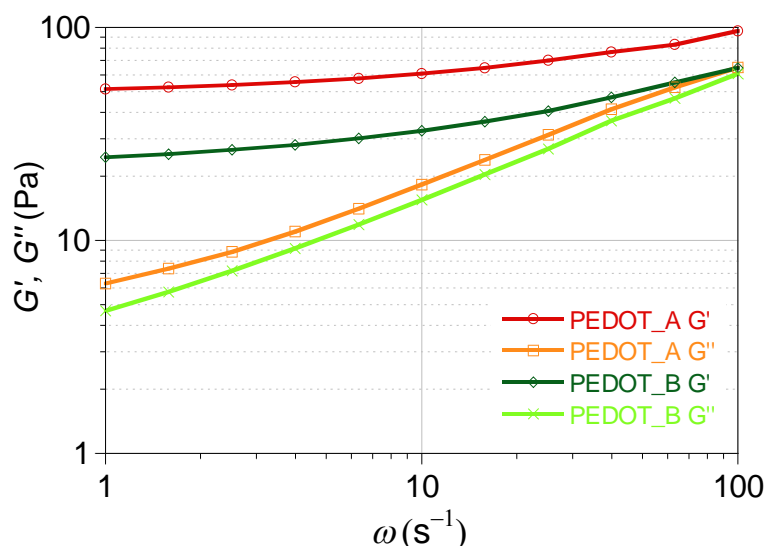
Fig. 19 PEDOT_A and PEDOT_B frequency sweep measurements.

From the *frequency sweep* measurements (Fig. 19) it is evinced that both PEDOT_A and PEDOT_B inks show high relaxation time and solid-like behaviour, since the *G'* are higher than the *G''*.[21] The differences observed in the ink performances with various cell shapes (Fig. 17 A-H) could be due to the differences in their elastic behaviour, as suggested by the increased moduli values for PEDOT_A, in particular the *G'*. As highlighted in the literature, the elasticity effects are significant for non-Newtonian fluids and could influence the ink transfer as a function of the cell shape.[9,16]

Creep tests on PEDOT_A and PEDOT_B inks have been performed to measure their yield point (Fig. 20).
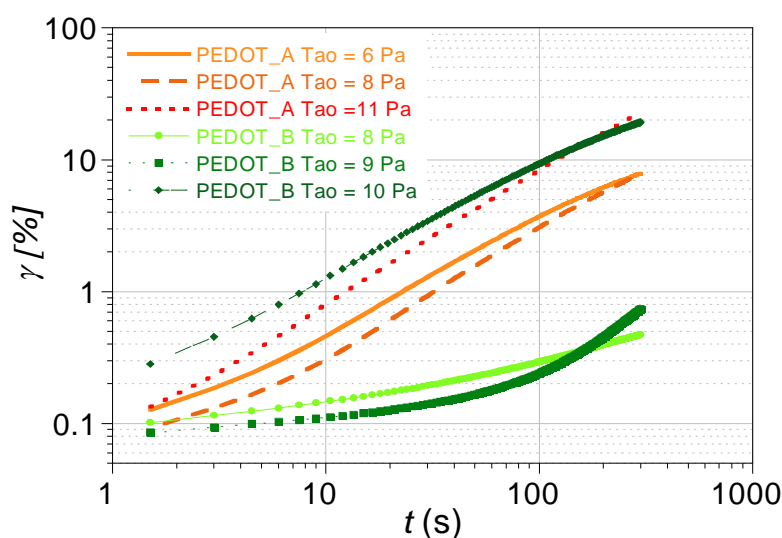
Fig. 20 PEDOT_A and PEDOT_B creep tests.

No significant differences have been pointed out between PEDOT_A and PEDOT_B, their yield stress is 9÷10 Pa and 9÷11 Pa respectively, but their yield points are order of magnitude higher

than the dielectric one. This strong behaviour can be observed as a dendritic arrangement of the ink after each rheological measurement (Fig. 21). The difficulty in obtaining a homogeneous layer with these two PEDOT:PSS based materials has been attributed to the limitations in levelling due to both the viscous forces acting in these materials and the high yield point. However, these forces acting in the material reduce ink spreading on the substrate, allowing to achieve high pattern definition, making these PEDOT:PSS inks suitable for high resolution steps, such as the contact definition.

Fig. 21 Disposition of the high yield point PEDOT:PSS based inks after the rheological measurements.

Electrical characteristics have been evaluated for PEDOT_A and PEDOT_B formulations. Several **resistors** have been realized printing on a PEN substrate the inks, using the same configuration as for the S/D contacts of OTFTs. To contact the material silver electrodes have been realized, as exposed in Chapter 5, Paragraph 2.3.1. Electrical characterization has been performed using the Suss PM5HF Analytical Probe Station equipped with a Hewlett Packard HP 4145B semiconductor parameter analyser.

In Fig. 22 are reported the typical I-V characteristics measured for the 3 fingers configuration.
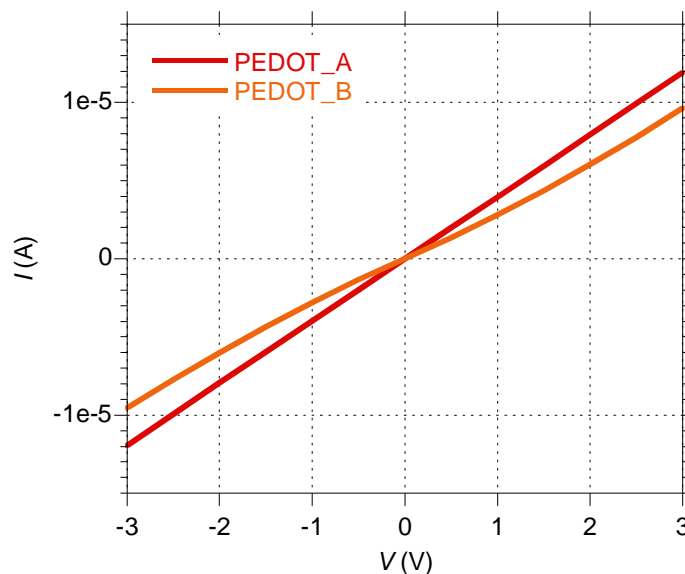
Fig. 22 I-V characteristics for PEDOT_A and PEDOT_B formulations.

All the films have been annealed at 100°C. The resistivity has been calculated from these measurements, for PEDOT_A $\approx$ 1.36·10^{-2} Ωcm, while for PEDOT_B $\approx$ 3.24·10^{-2} Ωcm, well comparable with the literature values obtained for printed PEDOT:PSS for S/D contacts.[26] These measurements show that the addition of the plasticizer has damaged the electrical properties of the printed film, as the curve for PEDOT_B is not perfectly linear. Hence, the PEDOT_A formulation should be preferred if considering the electrical performances.

4. Organic semiconductor inks

4.1. P-type organic semiconductor

The printing parameters of OSC have been optimized in order to obtain a homogeneous layer when deposited with the gravure printing technique.

To get **continuity** on the substrate the cliché has been functionalized with HMDS.

To optimize the **homogeneity**, the ink has been printed following the procedure for the study of the printability and the outcomes have been analysed by optical microscopy to define the best cell sizes and shapes. Some significant results are shown in Fig. 23. The general trend is that the homogeneity has been improved by increasing the cell area, while rhombic shaped cell outcomes show worst uniformity compared to hexagonal ones. In fact, the films obtained with rhombic cell shape show wider homogeneous areas but surrounded by large and long areas with reduced thickness among them.
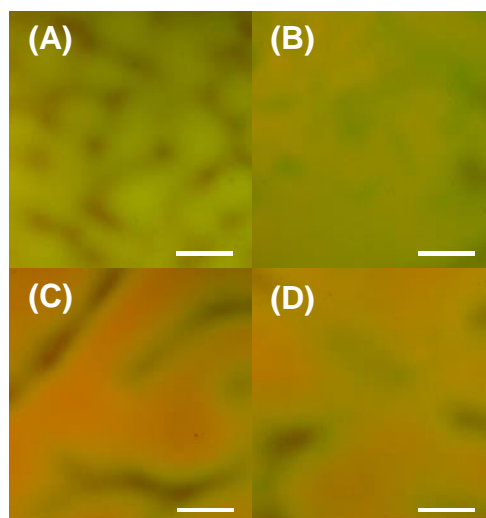
Fig. 23 OSC printing outcomes with the test cliché. (A) Hexagonal cell, printed area 12 mm², cell area 110 μm², cell depth 4 μm. (B) Hexagonal cell, printed area 12 mm², cell area 2340 μm², cell depth 4.6 μm. (C) Rhombic cell, printed area 12 mm², cell area 430 μm², cell depth 4.9 μm. (D) Rhombic cell, printed area 24 mm², cell area 1750 μm², cell depth 5.3 μm. Scale bar 100 μm.

The average film thicknesses, as expected, strongly depend on the cell shape and volume. The results are reported in Fig. 24.
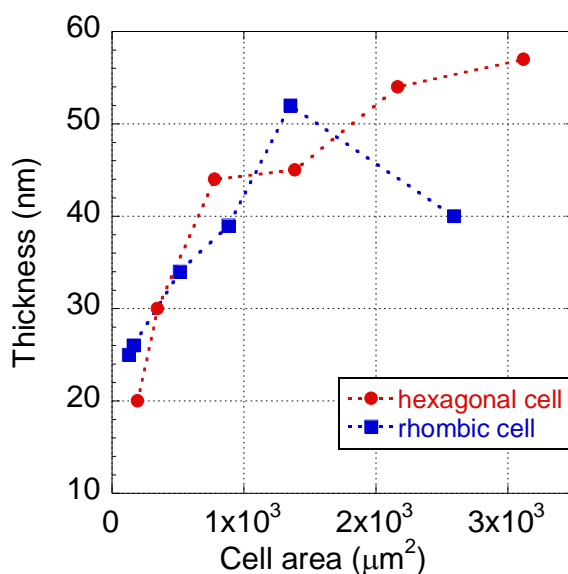
Fig. 24 OSC film thickness as a function of cell shape and volume.

Since the OSC is highly hydrophobic, with contact angle $\Theta_C \approx 92°$, the transfer of the gravure printed dielectric on it is reduced due to the poor wettability, which influences the fluid curvature on the substrate and so the capillary pressure gradient. To improve the transfer, a surface functionalization is applied both on the substrate ad on the cliché, as detailed in Chapter 2, Paragraph 2.2.4.

4.2. N-type organic semiconductor

The n-type semiconductor has been printed using two different blades, with the optimized gravure printing system following the procedure for the study of the printability. The printing outcomes are shown in the optical microscopy pictures reported in Fig. 25 A-B, the films have been obtained using an E600/25/22 degree bevel edge profile without support or an E10/25/22 degree bevelled edge profile with metallic support, respectively.
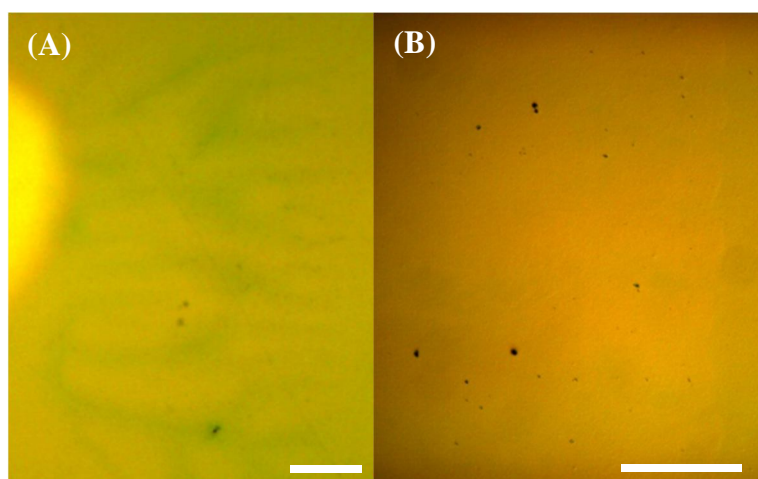
Fig. 25 Optical microscopy picture of the n-type organic semiconductor film obtained using an E600/25/22 degree bevel edge profile without support (A) or an E10/25/22 degree bevelled edge profile with metallic support. Scale bar 100 μm.

An improvement in the film **homogeneity** and definition has been observed for the ink wiped with the more loaded blade. The film thicknesses are around $10 \div 20$ nm and around 60 nm for the two different blades, respectively. The printing outcomes are not significantly dependent on the cell shape, while the **continuity** is ensured just for the thicker layers (> 50 nm).

5. Concluding remarks

According to the above analyses, it is possible to define, for the optimized printing system configuration, a **modified range of values** for the fluid dynamic parameters resulting in acceptable printability outcomes. Considering as $U = 0.1 \div 0.5$ m/s, $\eta \approx 10^2$ mPas, $\gamma = 20 \div 30$ mN/m, l around tens of microns, the suitable values of the fluid dynamic parameters result:

- $Ca = 2 \div 4$
- $Bo \approx 10^{-3}$
- $We \approx 10^{-1}$

- $Oh = 3 \div 9$
- $V^* \approx 10^{-1}$ m/s.

The following **formulation** and **printing configurations** have been chosen for OTFTs fabrication.

The formulation CYTOP_A as the dielectric ink, with hexagonal cell shape of 7642 μm^3 volume and aspect ratio 0.11, and PEDOT_A as the conductive ink, with rhombic cell shape of 11718 μm^3 volume and aspect ratio 0.18.

The CYTOP_A formulation has been selected for the dielectric ink to ensure the best interface with the OSC. The PEDOT_A has been preferred to the PEDOT_B since it has allowed to define straighter area edges, as shown in the optical microscopy pictures in Fig. 17 A-H. This requirement is rather strict for the printing of the S/D contacts layer. Moreover, PEDOT_A has shown better electrical performance.

For the p-type semiconductor, hexagonal cells with cell gap 2.5 μm have been chosen to obtain the better film uniformity. The area is 2261 μm^2 and the cell depth 4.7 μm, in order to achieve the desired thickness.

The n-type semiconductor has been printed using as blades the E10/25/22 degree bevelled edge profile with metallic support. The cell shape again has been the hexagonal of 10627 μm^3 volume and aspect ratio 0.08.

References

(1)   Khan, S.; Lorenzelli, L.; Dahiya, R. S. Technologies for Printing Sensors and Electronics Over Large Flexible Substrates: A Review. *IEEE Sens. J.* **2015**, *15* (6), 3164–3185.

(2)   Kahn, B. E. Patterning Processes for Flexible Electronics. *Proc. IEEE* **2015**, *103* (4), 497–517.

(3)   Hernandez-Sosa, G.; Bornemann, N.; Ringle, I.; Agari, M.; Dörsam, E.; Mechau, N.; Lemmer, U. Rheological and Drying Considerations for Uniformly Gravure-Printed Layers: Towards Large-Area Flexible Organic Light-Emitting Diodes. *Adv. Funct. Mater.* **2013**, *23* (25), 3164–3171.

(4)   Grau, G.; Cen, J.; Kang, H.; Kitsomboonloha, R.; Scheideler, W. J.; Subramanian, V. Gravure-Printed Electronics: Recent Progress in Tooling Development, Understanding of Printing Physics, and Realization of Printed Devices. *Flex. Print. Electron.* **2016**, *1* (2), 023002.

(5)   Kitsomboonloha, R.; Morris, S. J. S.; Rong, X.; Subramanian, V. Femtoliter-Scale Patterning by High-Speed, Highly Scaled Inverse Gravure Printing. *Langmuir* **2012**, *28* (48), 16711–16723.

(6)   Subramanian, V.; Cen, J.; de la Fuente Vornbrock, A.; Grau, G.; Kang, H.; Kitsomboonloha, R.; Soltman, D.; Tseng, H.-Y. High-Speed Printing of Transistors: From Inks to Devices. *Proc. IEEE* **2015**, *103* (4), 567–582.

(7)   Dodds, S.; Carvalho, M. da S.; Kumar, S. Stretching and Slipping of Liquid Bridges near Plates and Cavities. *Phys. Fluids* **2009**, *21* (9), 092103.

(8)   Lee, S.; Na, Y. Analysis on the Ink Transfer Mechanism in R2R Application. *J. Mech. Sci. Technol.* **2010**, *24* (1), 293–296.

(9)   Sankaran, A. K.; Rothstein, J. P. Effect of Viscoelasticity on Liquid Transfer during Gravure Printing. *J. Non-Newton. Fluid Mech.* **2012**, *175–176*, 64–75.

(10)   Kitsomboonloha, R.; Subramanian, V. Lubrication-Related Residue as a Fundamental Process Scaling Limit to Gravure Printed Electronics. *Langmuir* **2014**, *30* (12), 3612–3624.

(11)   Huang, C.-H.; Carvalho, M. S.; Kumar, S. Stretching Liquid Bridges with Moving Contact Lines: Comparison of Liquid-Transfer Predictions and Experiments. *Soft Matter* **2016**, *12* (36), 7457–7469.

(12)   Campana, D. M.; Ubal, S.; Giavedoni, M. D.; Saita, F. A.; Carvalho, M. S. Three Dimensional Flow of Liquid Transfer between a Cavity and a Moving Roll. *Chem. Eng. Sci.* **2016**, *149*, 169–180.

(13)   Hariprasad, D. S.; Grau, G.; Schunk, P. R.; Tjiptowidjojo, K. A Computational Model for Doctoring Fluid Films in Gravure Printing. *J. Appl. Phys.* **2016**, *119* (13), 135303.

(14)   Kang, H. W.; Sung, H. J.; Lee, T.-M.; Kim, D.-S.; Kim, C.-J. Liquid Transfer between Two Separating Plates for Micro-Gravure-Offset Printing. *J. Micromechanics Microengineering* **2009**, *19* (1), 015025.

(15)   Lee, J. A.; Rothstein, J. P.; Pasquali, M. Computational Study of Viscoelastic Effects on Liquid Transfer during Gravure Printing. *J. Non-Newton. Fluid Mech.* **2013**, *199*, 1–11.

(16)   Ahn, S.; Lee, S.; Na, Y. Elasticity Effect on the Ink Transfer Process in Gravure Printing. In *International Conference on Computational Science and Its Applications*; Springer, 2008; pp 565–575.

(17)   Grau, G.; Subramanian, V. Fully High-Speed Gravure Printed, Low-Variability, High-Performance Organic Polymer Transistors with Sub-5 V Operation. *Adv. Electron. Mater.* **2016**, *2* (4), 1500328.

(18) Darhuber, A. A.; Troian, S. M.; Miller, S. M.; Wagner, S. Morphology of Liquid Microstructures on Chemically Patterned Surfaces. *J. Appl. Phys.* **2000**, *87* (11), 7768–7775.

(19) Bird, R. B.; Stewart, W. E.; Lightfoot, E. N. *Transport Phenomena*, 2nd ed.; John Wiley & Sons Inc, 2002.

(20) Schramm, G. *A Practical Approach to Rheology and Rheometry*, 2nd ed.; Gebrueder HAAKE GmbH: Karlsruhe, Federal Republic of Germany, 2000.

(21) Hackley, V. A.; Ferraris, C. F. *Guide to Rheological Nomenclature: Measurements in Ceramic Particulate Systems*; National Institute of Standards and Technology Special Publication 945 Natl. Inst. Stand. Technol. Spec. Publ. 946, 2001.

(22) Fukuda, K.; Someya, T. Recent Progress in the Development of Printed Thin-Film Transistors and Circuits with High-Resolution Printing Technology. *Adv. Mater.* **2016**.

(23) Horowitz, G. Organic Thin Film Transistors: From Theory to Real Devices. *J. Mater. Res.* **2004**, *19* (07), 1946–1962.

(24) Boelens, A. M. P.; de Pablo, J. J.; Lim, S.; Francis, L.; Ahn, B. Y.; Lewis, J. A. Visualization and Simulation of the Transfer Process of Index-Matched Silica Microparticle Inks for Gravure Printing. *AIChE J.* **2017**, *63* (4), 1419–1429.

(25) Voigt, M. M.; Mackenzie, R. C. I.; King, S. P.; Yau, C. P.; Atienzar, P.; Dane, J.; Keivanidis, P. E.; Zadrazil, I.; Bradley, D. D. C.; Nelson, J. Gravure Printing Inverted Organic Solar Cells: The Influence of Ink Properties on Film Quality and Device Performance. *Sol. Energy Mater. Sol. Cells* **2012**, *105*, 77–85.

(26) Barret, M.; Sanaur, S.; Collot, P. Inkjet-Printed Low-Voltage Organic Thin-Film Transistors: Towards Low-Cost Flexible Electronics. In *Mater. Res. Soc. Symp. Proc. 1003*; 2007.

Chapter 4
Inkjet printing technique

1. The inkjet printing technique

As anticipated in the first chapter, inkjet printing is a non contact technique that allows the direct patterning. The process consists of five steps: ejection from the nozzles, flight, impact on the substrate, ink spreading and drying of the solvent (Fig. 1).[1]
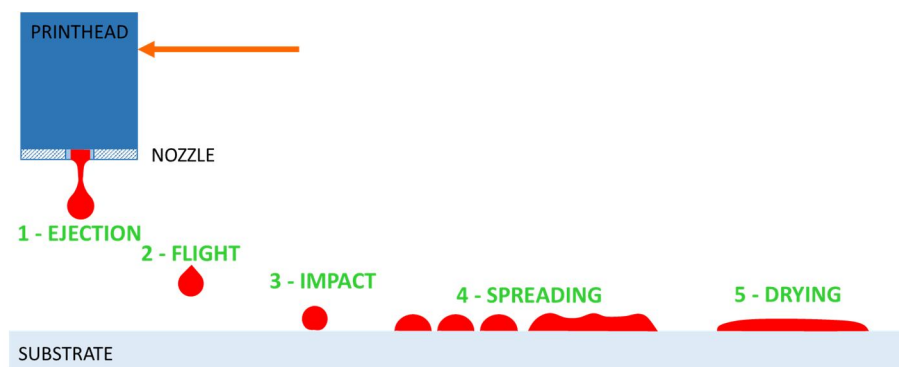
Fig. 1 The five steps of the inkjet printing process (out of scale).

The ink is ejected through a series of micrometer sized nozzles located on the printhead. Among the different mechanisms of actuation of the printhead, the most promising are the piezoelectric and electrohydrodynamic systems.[2] The system used in this thesis work (Fig. 2, Dimatix DMP 2800 by Fujifilm) is based on a piezoelectric actuation.
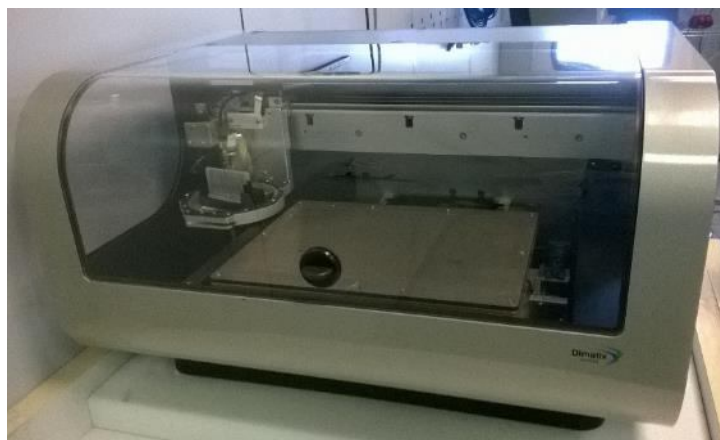
Fig. 2 The inkjet printer used for this thesis work.

This system is designed for feasibility tests, material development, prototyping and digital pattern optimization. Drops around 1 pl or 10 pl volume, depending on the nozzle dimensions in the cartridge jetting module (Fig. 3), are ejected at the corresponding pulse generated by the piezoelectric actuator. The printer provides an optical alignment system, combined with the possibility of moving the platen in horizontal, vertical and rotation, while the printhead has only the horizontal degree of freedom. The temperature of both the cartridge and the platen, on which the substrate is fixed with a vacuum system, as well as both the substrate and the printhead height, can be defined by the user. The cartridge settings allow to define several printing parameters, the waveform and the cleaning procedure, as it will be discussed in the next paragraphs.

Fig. 3 The cartridge. The jetting module is a DMC 11610 printhead.

The main factors that affect the inkjet printing results can be sum up as:
- *ink properties*;
- *jetting conditions*;
- *substrate wettability* and *roughness*.[3]

This printing technique allows to deposit soluble materials with low viscosity, dispersions of small particles, several functional molecules, colloidal solutions. The **main features for inks** optimised for this inkjet system, similar to those required for an industrial system, are the following:
- *viscosity* 10÷12 mPas at jetting temperature, if it is too high the fluid will not flow through the nozzle, too low the drop formation is not optimal;

- *surface tension* 28÷33 mN/m at jetting temperature, if it is too high the air will not be removed in the jetting mechanism before the printing, so the ink cannot be jetted, if it is too low the ink will flow continuously from the nozzles;

- *specific gravity* > 1 g/cc;

- *non-volatile solvent*, with high boiling point > 100°C, to avoid nozzle clogging;

- *degassing*, gas in the fluid prevents jetting as it interferes with the piezo pulse;

- *filtration* < 1 μm;

- *free of gels*, which can clog the nozzles.[3]

Among the **issues** of the inkjet printing technique, the main problem is due to the difficulty in obtaining a *continuous* and *homogeneous* film over a large area. Since individual drops are jetted, they have to spread on the substrate to form a continuous layer. This process is strongly affected by the *substrate-ink interactions*, mainly due to their surface tension and to the substrate roughness or functionalization, but it also depends on the distance of the substrate from the printhead and on the substrate and ink temperatures at the jetting instant. Moreover, the material tends to migrate to the edges of the printed dot, generating the so called *coffee ring effect*. Hence, this technique results to be more suitable to deposit small amounts of material over small areas.[1,4]

Moreover, material loading and management is very critical in inkjet printing, since the ink contacts with the dispensing system and the additives used to obtain the desired ink properties can damage their electrical performances.[4]

The ink is subjected to high mechanical shear forces during the jetting, which could change its features. The even partial nozzle *clogging* during printing leads to fluctuations in the drop volume and trajectory, limiting the final registration accuracy, resolution and layer homogeneity.[4] The first procedures to avoid nozzle clogging are an extensive US sonication of the material to break the agglomerates and its filtration before the cartridge filling.

The drop formation may require some space, to recover the tail generated during the ejection (Fig. 4 A). Some smaller droplets of ink may split off from the main jet following the tail, requiring some space and time to rejoin the main drop. These issues limit the printhead distance from the substrate and the jetting frequency. In some cases, the smaller droplets fail to rejoin the main one and generate the satellite droplets, which are deposited in unintended locations on the substrate (Fig. 4).[4]
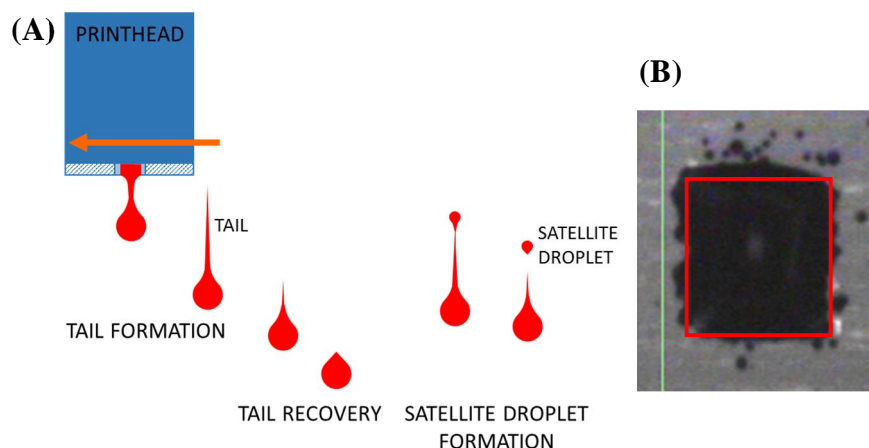
Fig. 4 Drop formation: tail formation and recovery, satellite droplet formation (A) and effect of satellite droplets on the printed pattern, in red the original pattern (B).

Several **process parameters** have to be fitted to ink and substrate characteristics, to avoid the previously discussed issues. The main parameters are detailed in the following list and will be discussed in the following paragraphs:

- ejected *drop volume*;

- *platen temperature*;

- *cartridge temperature*;

- *jetting frequency*;

- *meniscus set point*;

- *drop space*;

- cartridge *cleaning cycles*;

- *waveform.*

1.1. The waveform

In Fig. 5 is schematized a typical **jetting waveform**, which defines how the piezoelectric actuator is moved on the fluid chamber membrane.
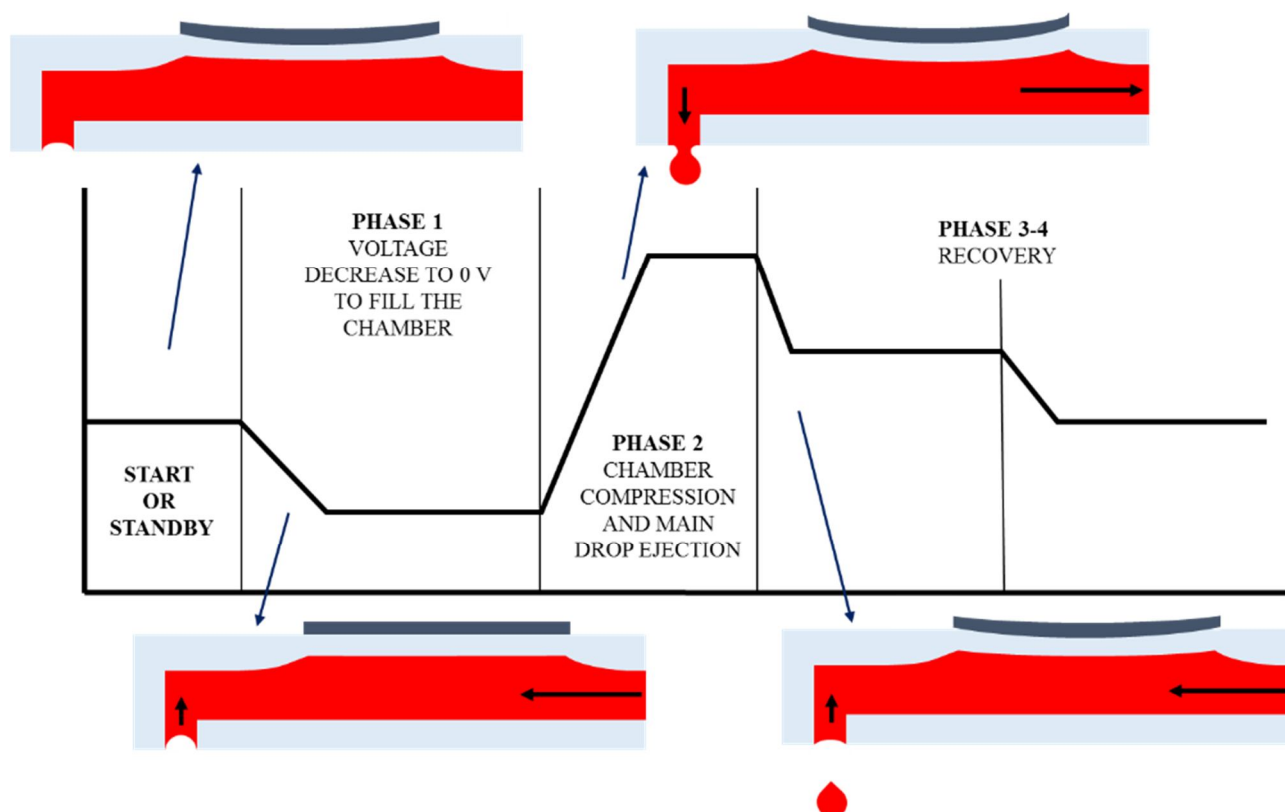
Fig. 5 Typical jetting waveform and its relation to the jetting process. Start and phase 4 are the same segment.

The typical basic jetting waveform is divided into four segments, depending on the voltage applied to the piezoelectric actuator. Each segment is characterized by the following features:

- *duration*, the time interval in which the fluid chamber membrane element held the position;

- *level* or amplitude, the applied voltage that influences the bending of the fluid chamber membrane;

- *slew rate*, the bending speed of the fluid chamber membrane.

The applied voltage, the duration of the first segment, the slew rate and duration of the second segment have the most impact on the jetting process.[3]

It has to be noticed that the meniscus is kept at the edge of the nozzle operating under negative pressure. Hence, to fit the ink viscosity and surface tension, the value of the *meniscus set point* has be correct before changing the waveform.

The idle nozzles during printing are working with the **non-jetting waveform**, a small amplitude signal in the tickle mode. Its amplitude can be raised to avoid clogging of the nozzles for critical inks.[3]

Different waveforms have been refined depending on the ink characteristics, the ejected drop volume and the application. The main waveform parameters used during this thesis work are

schematized in the following table (Tab. 1). The ink considered are commercial available dispersions of silver nanoparticles, PEDOT:PSS or carbon nanoparticles, in triethylene glycol monoethyl ether, ethanol or water.

	AgC	*AgCTop*	*AgANP1pl*	*pedot*	*Cink1*	*Cink2*
Duration scaler	1	1	1	1	1	1
Width (µs)	9.856	9.408	24.320	11.520	12.160	19.648
Maximum jetting frequency (kHz)	20	20	8	20	5	4
Jetting waveform						
Start						
Level (%)	-	0	7	-	-	-
Slew rate	-	1.6	1	-	-	-
Duration (µs)	-	3.584	4.032	-	-	-
Phase 1						
Level (%)	33	-	-	0	0	0
Slew rate	0.40	-	-	0.65	0.65	0.65
Duration (µs)	3.968	-	-	3.584	3.648	3.648
Phase 2						
Level (%)	100	100	100	100	100	87
Slew rate	1.60	0.80	0.27	0.40	0.36	0.36
Duration (µs)	1.984	1.600	6.592	3.712	6.784	8.896
Phase 3						
Level (%)	47	27	13	67	67	67
Slew rate	1.84	0.60	1.00	0.60	0.60	0.60
Duration (µs)	3.392	3.392	6.4	3.392	1.216	4.672
Phase 0						
Level (%)	-	-	47	-	-	-
Slew rate	-	-	0.40	-	-	-
Duration (µs)	-	-	5.824	-	-	-
Phase 4						
Level (%)	40	0	7	40	40	47
Slew rate	0. 80	0.80	0.80	0.80	0.80	0.80
Duration (µs)	0.512	0.832	1.472	0.832	0.512	2.432
Non-Jetting waveform						
Segment 1						
Level (%)	53	0	20	53	53	53
Slew rate	1.00	1.00	1.00	1.00	1.00	1.00
Duration (µs)	3.712	9.408	6.080	3.712	3.776	3.776
Segment2						
Level (%)	40	-	7	40	40	47
Slew rate	1.00	-	1.00	1.00	1.00	1.00

Duration (μs)	6.144	-	18.240	7.808	8.384	15.872

Tab. 1 Waveform parameters. The acronyms correspond to the hereafter detailed processes: *AgC* for evaporated contact thickening with silver, Paragraph 2.1; *AgCTop* for silver top contacts, Paragraph 2.2; *AgANP1pl* for silver source and drain contacts, Paragraph 2.3; *Pedot* for PEDOT:PSS contacts, Paragraph 3; *Cink1* and *Cink2* for carbon resistors, Paragraph 4.

For some inks it has been necessary to insert, between phase 3 and phase 4, a segment (called phase 0), which causes a partial chamber compression. Its function has been to stabilize the new ejected drop, reducing the tail and the satellite droplets formation.

For the ANP DGP40 LT-15C printed with 10 pl drop volume, a given waveform yet optimized for this material has been used without further modifications.

1.2. The nozzle cleaning

There are four possible functions to clean the nozzles:
- *purging*, forces the fluid out of all nozzles at once;
- *spitting*, ejects a number of drops with the defined frequency;
- *blotting*, brings the nozzle plane in close proximity to a cleaning pad to remove the ink excess;
- *tickle mode*, low amplitude movement of the chamber to avoid nozzle clogging during printing.[3]

A cleaning cycle can be defined using a sequence of different cleaning functions, with different durations, frequency and delays among them. The cycle can be repeated before and after each printing process or every defined number of bands (lines printed) or time interval during the printing.

The main cleaning cycles used during this thesis work are detailed in Tab. 2 hereafter.

	Duration (ms)	Frequency (kHz)	Delay (s)
start			
Spit	50	1.5	1
Purge	100		1
Blot	500		
Spit	150	1.5	1
interstmp			
Spit	200	1.5	1
Purge	100		1
Blot	200		
Spit	70	1.5	1
clog (for heavily clogged nozzles cleaning)			

Spit	300	1.5	1
Purge	800		1
Blot	4000		
Spit	300	1.5	1

Tab. 2 Cleaning cycles.

2. Silver ink

The silver nanoparticles based dispersion inks used have been the Cabot AG-IJ-G-100-S1 and the ANP DGP40 LT-15C.

Before filling the cartridge, the materials have been sonicated in the US bath for 1 h, left for 1 h and filtered with a 0.45 or 0.22 μm polyvinylidene fluoride (PVDF) filter (Millex®-HV, Merck Millipore Ltd.).

2.1. Contact thickening

The inkjet printing technique is particularly suitable for the deposition of small amounts of materials with specific electrical, optical, chemical, biological, or structural functionalities, to pattern them on the substrate with highly resolved features.[4] Hence, this technique has been used for the thickening of the transistor metallic contact thermally evaporated and patterned by lithography. The required resolution is critical, the pad area is around 200x100 μm, moreover the metal is much more hydrophobic than the substrate, so even if a single drop or satellite droplet is inkjetted in proximity of the substrate it will be attracted, bringing most of the ink out of the pad as shown in Fig. 6.

Fig. 6 Inkjetted silver over a contact pad: effect of the substrate attraction on the ink due to its better wettability compared to the metal. Scale bar 100 μm.

The printing conditions have been optimized, the **process parameter** chosen are the following:

- ejected drop volume: 10 pl

- platen temperature: disabled

- cartridge temperature: 35°C

- jetting frequency:15 kHz

- meniscus set point: 4.0 inches H_2O

- drop space: 20 μm

- cartridge cleaning cycles: start of print *start*; during print *interstmp* every 200 bands or every 180 s

- waveform: *AgC*

The ink used for these samples is the Cabot AG-IJ-G-100-S1.

The Fig. 7 shows the **printing outcomes**.
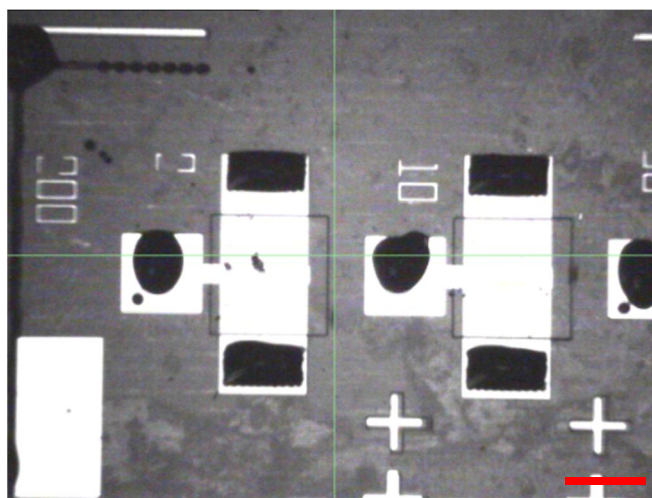
Fig. 7 Contact thickening of a TFT array with inkjetted silver. Scale bar 200 μm.

It has been possible to obtain a highly resolved pattern on a 6x6 array of transistors without observable registration issues.

2.2. Top contact

The aim of these tests has been to verify that the inkjet printing will not damage the dielectric layer, in order to use this technique to realize the gate contact of the OTFTs.

2.2.1. Metal-Insulator-Metal devices

The dielectric used in this thesis work (Cytop™ CTL809M, AGC Chemicals) is strongly hydrophobic, with contact angle ≈ 112°. To improve its wettability, the surface has been treated with a plasma oxygen, in the RIE system, before each printing procedure, with the following receipt:

- 90% O_2 (64.8 sccm)

- 150 W

- bias under 200 V

- pressure ~ 300 mTorr

- etching time 5 s.

The drop diameter after this surface treatment, using a 10 pl drop volume, is ≈ 40 μm.

To test if the dielectric preserves its electrical characteristics when deposited through the gravure printing technique, **MIM** devices have been realized (Fig. 8).
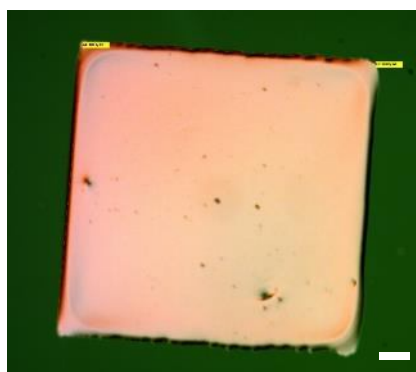
Fig. 8 MIM device with inkjetted top contact. Scale bar 100 μm.

The process is detailed hereafter.

1. Substrate, doped silicon, cleaning: deep in BHF solution diluted 1:10.

2. Dielectric deposition through spin-coating technique.

3. Annealing 1 h at 100°C in vacuum oven.

4. Top contact deposition through inkjet printing with the following **process parameters**:

    - ejected drop volume: 10 pl

    - platen temperature: disabled

    - cartridge temperature: 35°C

    - jetting frequency:15 kHz

    - meniscus set point: 4.0 inches H_2O

    - drop space: 20 μm

    - cartridge cleaning cycles: start of print *start*; during print *interstmp* every 200 bands or every 180 s

    - waveform: *AgCTop*

5. Annealing 60°C overnight in oven.

The ink used for these samples is the Cabot AG-IJ-G-100-S1.

The top contact area is a square with side 1 - 0.75 – 0.5 mm and with thickness around 900 nm. The resulting dielectric thickness has been measured around 500 nm and 250 nm, depending on the spinning speed.

In Fig. 9 are reported the results of the device **electrical characterization** with ramp rate 1 V/s.
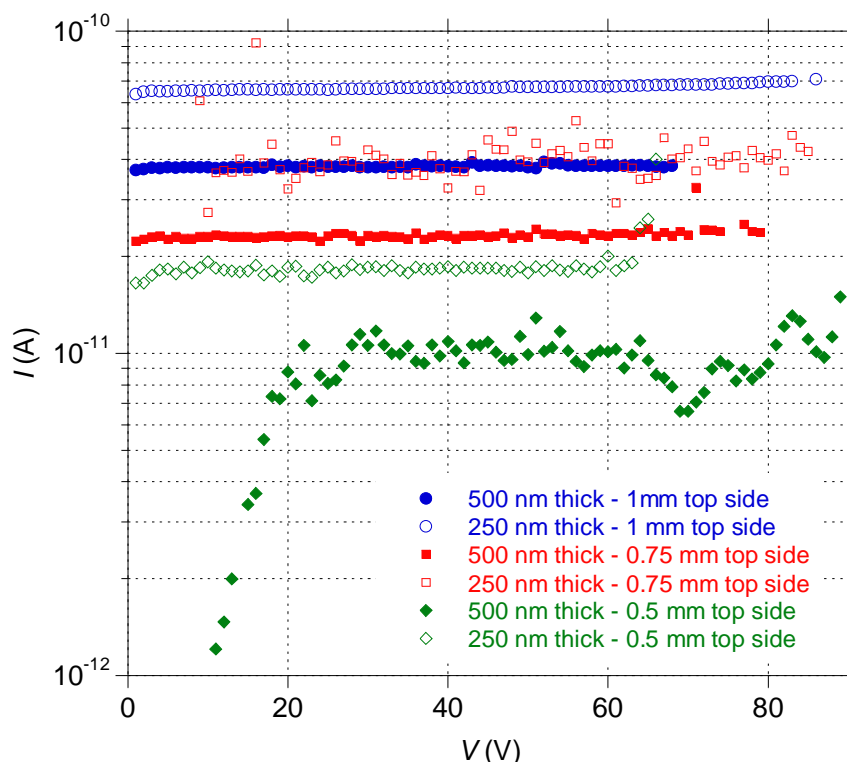
Fig. 9 I-V characteristics of MIM devices with the top contact inkjet printed. The dielectric is 550 or 250 nm, while the top electrode is a square with side 1 mm - 750 μm - 500 μm.

The instrument inferior limit is nearby 10^{-12}, inducing the instabilities observed in the measurements of the smaller area devices (green plain rhombi in Fig. 9). The resulting electric field strength is $E_b = 1.4 \div 2.8$ MV/cm.

The data are well comparable to those reported in Chapter 1 Fig. 19, obtained with the dielectric spin-coated on silicon and top contact in Al thermally evaporated. This result proves the suitability of this process for the realization of electrodes without damaging the dielectric electrical performances.

2.2.2. Resistors

Several **resistors** have been realized to measure the printed silver electrical characteristics. The printing procedure is the same as for the top contact for the MIM devices above explained. **Electrical**

characterization has been performed using the Suss PM5HF Analytical Probe Station equipped with a Hewlett Packard HP 4145B semiconductor parameter analyser.

The dependence of the material resistivity on the *annealing temperatures* has been measured and the results are shown in Fig. 10.
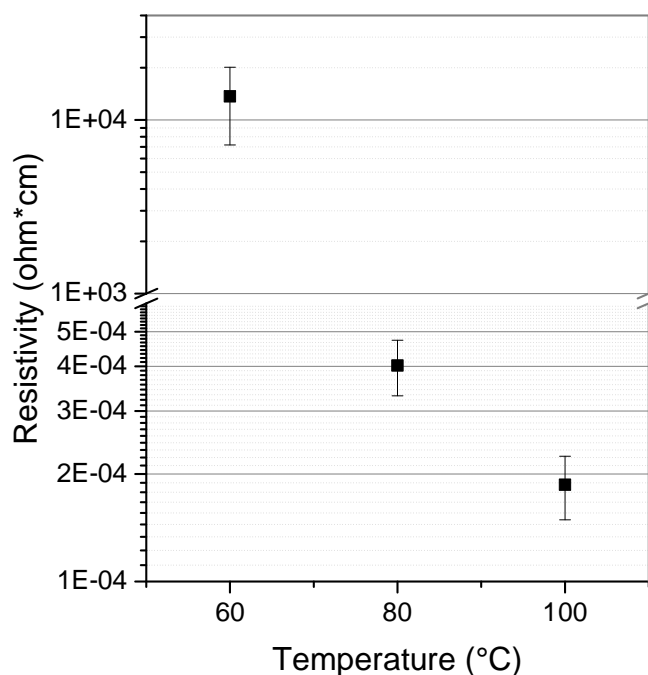
Fig. 10 Annealing temperature dependence of the inkjetted silver film.

The annealing at low temperature does not allow a perfect sintering of the nanoparticles, as a consequence the resistivity of the resulting film is increased. However, limiting the temperature is necessary to avoid substrate shrinkage, besides it allows to develop a low temperature process compatible with many plastic substrates. Moreover, the gate annealing of OTFTs in top gate configuration requires a low temperature process in order to avoid damages at the OSC. The inkjetted film results to be suitable for the gate electrodes realization when annealed at a temperature $\geq 80°C$.

2.3. Source and drain contacts

The metallic S/D contacts of the fully printed OTFTs have been realized through the inkjet printing technique. This deposition method has been chosen since it ensures a high resolution and a fast prototyping procedure, allowing to change easily the printed pattern and the film thickness modifying the CAD layout without the necessity to realize a master.

Two different processes have been optimized in order to achieve two contact thicknesses.

2.3.1. Thick contacts

The procedure optimized to obtain thick contacts is detailed hereafter.

1. Substrate cleaning: US bath with acetone 2 min and IPA 3 min.

2. Silver inkjet printing with the following **process parameters**:

   - ejected drop volume: 1 pl

   - platen temperature: 45°C

   - cartridge temperature: 40°C

   - jetting frequency: 6.58 kHz

   - meniscus set point: 3.0 inches H_2O

   - drop space: 25 µm

   - cartridge cleaning cycles: during print *interstmp* every 200 bands or every 320 s

   - waveform: *AgANP1pl*

3. Annealing 100°C overnight in oven.

The ink used for these samples is the ANP DGP40 LT-15C. As substrate has been chosen a heat-stabilized, low roughness PEN foil, Teonex® Q65HA, by DuPont, 100 µm thick.

The drop diameter is ≈ 40 µm.

The Ag line widths after the annealing are for the large ones, with multiple drops, 120 µm, for the little ones, obtained with a single drop, 60 µm (Fig. 11). A variability of some microns has been observed among different samples, it depends on the substrate effective wettability and temperature during the printing, due to the external ambient conditions.
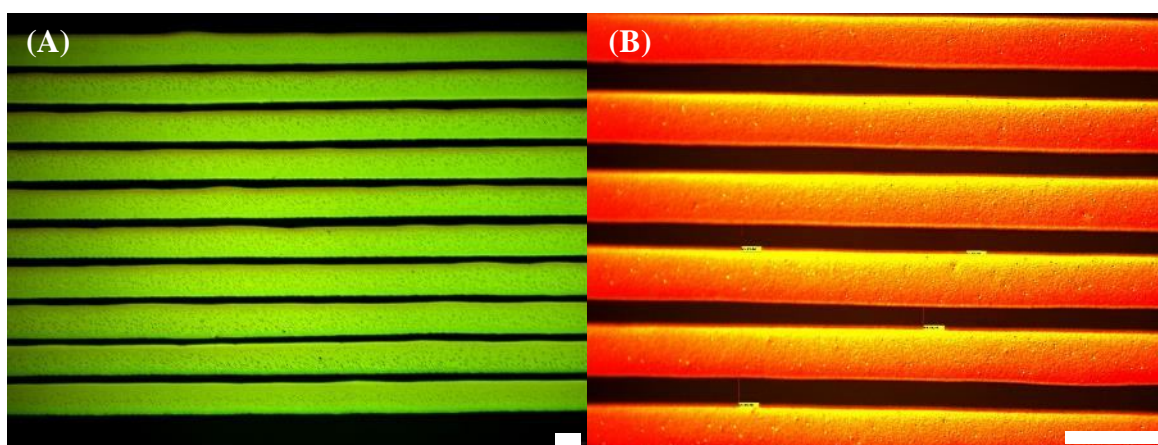
Fig. 11 Optical microscopy pictures of silver inkjet printed thick contacts with the minimum *L* achieved, A) contact width 120 µm, *L* ≈ 30 µm; B) contact width 60 µm, *L* ≈ 20 µm. Scale bar 100 µm.

The *contact profile* has been measured, the typical results are reported in Fig. 12 for both electrode width.
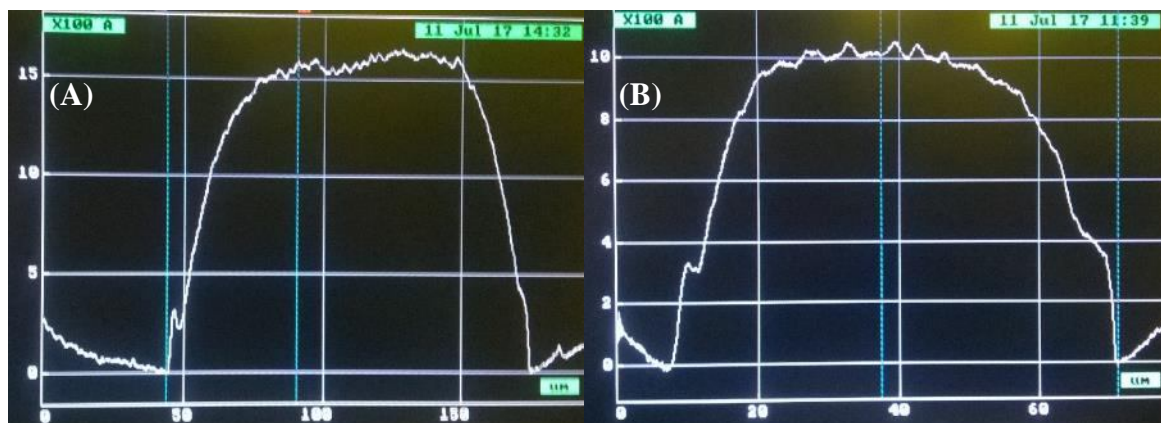
Fig. 12 Profile of the silver inkjet printed thick contacts, A) contact width ≈ 120 µm, contact thickness ≈ 160 nm; B) contact width ≈ 60 µm, contact thickness ≈ 100 nm.

Since the contact height is high compared to the semiconductor ideal thickness (around few tens of nanometres), the *contact edge profiles* have been verified as follows.
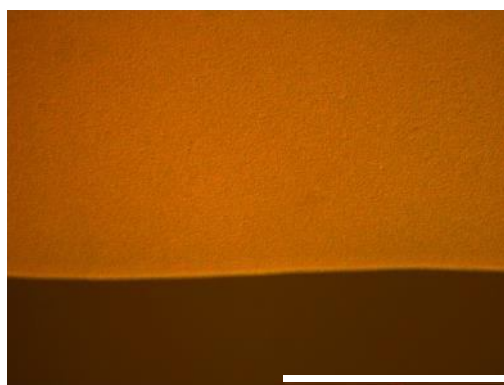
Fig. 13 Optical microscopy picture of the thick silver contact edge morphology. Scale bar 100 µm.

The larger contacts show a good morphology of the silver film, also on the edge (Fig. 13). It results in a smoother edge profile, the film thickness increases gradually for around 30 µm length to achieve the final height (Fig. 14 A). Moreover, the coffee ring effect is negligible, under 20 nm, and the final roughness is around 10 nm (Fig. 14 B). These features should allow a continuous distribution of the semiconductor when deposited by gravure printing.
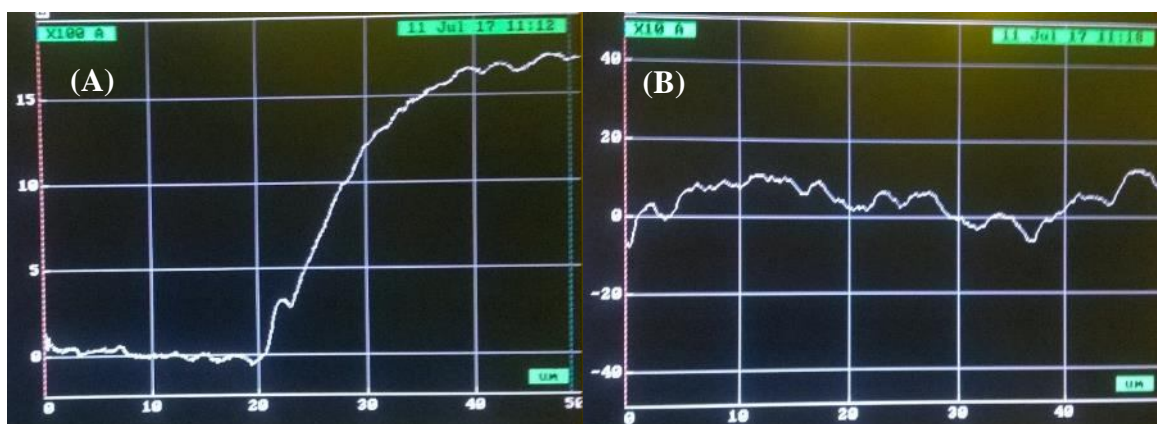
Fig. 14 Profile of the larger silver inkjet printed thick contacts, A) edge; B) roughness.

Several **resistors** have been realized to measure the electrical characteristics of the printed silver contacts, to verify if they are suitable as source and drain of OTFTs. The printing procedure is the same above exposed, the pattern is the same as a finger of an interdigitated contact of the OTFTs. **Electrical characterization** has been performed using the Suss PM5HF Analytical Probe Station equipped with a Hewlett Packard HP 4145B semiconductor parameter analyser.

The I-V characteristics are reported in Fig. 15.
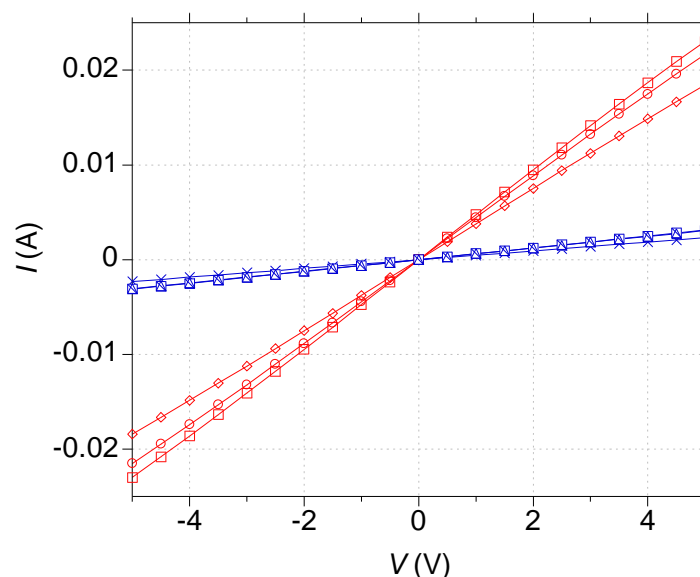
Fig. 15 I-V characteristics of the S/D contacts in silver inkjet printed.
In red the larger contacts, in blue the little ones.

The resistance of a large finger is $\approx 240\ \Omega$, while for a small one is $\approx 1800\ \Omega$. The resistivities calculated from these curves, in the order of $10^{-4}\ \Omega$cm, are in agreement with those obtained with the other ink in similar printing conditions and with the same annealing temperature (Fig. 10), as

expected. The electrical characterization confirms the suitability of the large width contacts for the application.

2.3.2. Thin contacts

Since the substrate is highly hydrophobic, it is not possible for the ink to spread properly and so it is not possible to achieve low thickness films. To improve the PEN substrate wettability, the surface has been treated with a plasma oxygen, in the RIE system, with the following receipt:

- 90% O_2 (64.8 sccm)

- 150 W

- bias under 200 V

- pressure ~ 300 mTorr

- etching time 5 s.

The PEN contact angle has been measured in different conditions, as it is treated during the process, the results are schematized in Tab. 3. The contact angle measurements have been performed analysing the USB microscope (DigiMicro Prof, dnt) pictures with the support of a plugin of ImageJ, Drop analysis – LB – ADSA.

Substrate treatment	Θ_C (°)
PEN treated side	81
PEN non treated side	88
PEN non treated side + acetone 2 min + IPA 3 min	70
PEN non treated side + acetone 2 min + IPA 3 min + RIE	26
PEN non treated side + acetone 2 min + IPA 3 min + RIE + oven 100°C overnight	40÷57

Tab. 3 PEN contact angles, water.

The procedure is effective to reduce the contact angle. The drop diameter after this surface treatment, using a 1 pl drop volume, is ≈ 80 μm. The substrate does not completely recover its original hydrophobicity after the usual annealing step of the silver layer, showing a variable contact angle on its surface.

To obtain a contact as thin as possible, the space between two inkjetted drops has been varied in order to define the maximum one still appropriate to define continuous and homogeneous lines (Fig. 16). The most suitable has resulted to be the 60 μm, which corresponds to a 25% overlap between two drops.

drop space = 50 μm   **drop space = 60 μm**

drop space = 65 μm   **drop space = 70 μm**
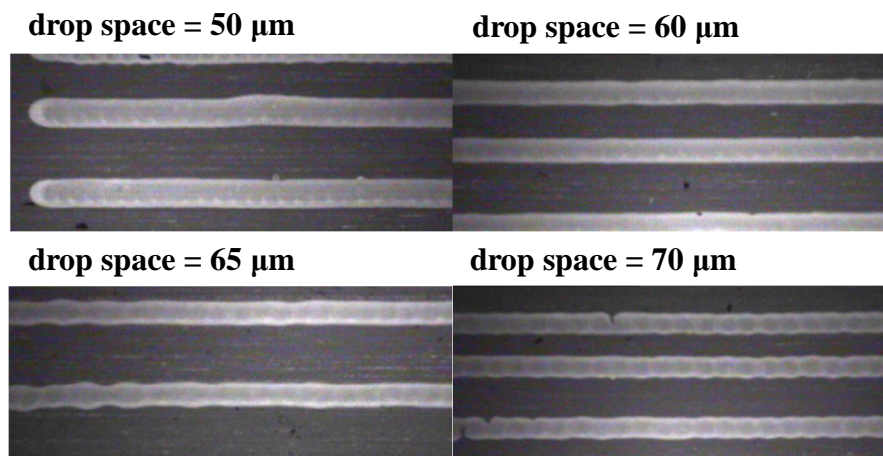
Fig. 16 Drop space variation effects. Under 60 μm some bulging effects are visible, while for larger values the lines follow the single drops undulations, the line continuity is compromised for 70 μm.

In the optical microscopy picture in Fig. 17 A the resulting S/D contacts are shown. The fingers are straight even at the end of the finger, without bulging or break points. The continuity is ensured also for the vertical elements, as verified in transmission mode for the junction between the horizontal and vertical lines (Fig. 17 B).
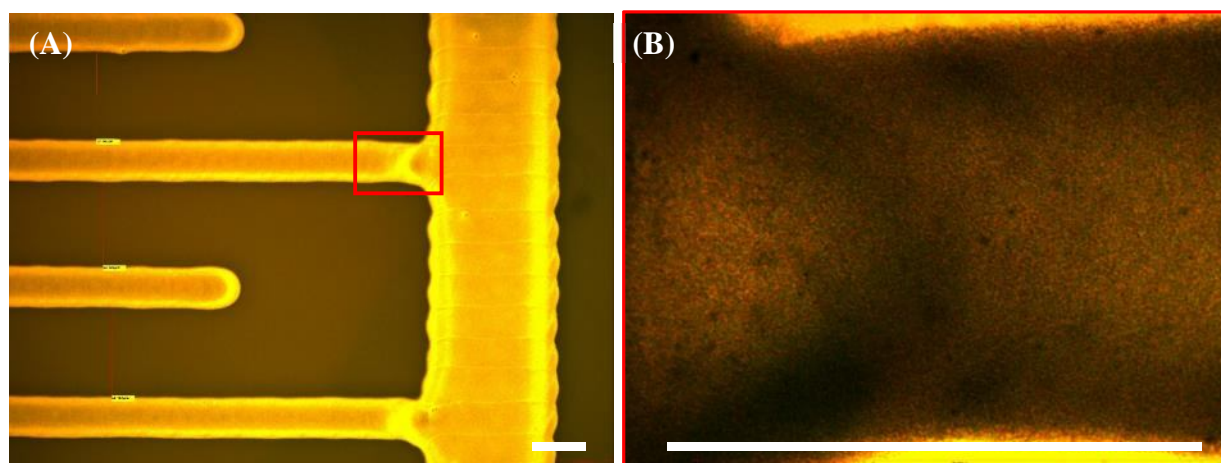
Fig. 17 (A) Optical image of thin interdigitated S/D contacts. (B) Magnification in transmission of the red rectangle area. Scale bar 100 μm.

The process optimized to obtain thin contacts is detailed hereafter.

1. Substrate cleaning: US bath with acetone 2 min and IPA 3 min.

2. Substrate treatment with RIE as exposed above.

3. Silver inkjet printing with the following **process parameters**:

   - ejected drop volume: 1 pl

   - platen temperature: 50°C

- cartridge temperature: 40°C

- jetting frequency: 2.74 kHz

- meniscus set point: 3.0 inches H_2O

- drop space: 60 µm

- cartridge cleaning cycles: during print *interstmp* every 200 bands or every 320 s

- waveform: *AgANP1pl*

4. Annealing 100°C overnight in oven.

The ink used for these samples is the ANP DGP40 LT-15C. As substrate has been chosen a heat-stabilized, low roughness PEN foil, Teonex® Q65HA, by DuPont, 100 µm thick.

The contacts have been obtained with single drop lines, their width after the annealing is ≈ 85 µm (Fig. 18). The contact thickness is ≈ 60 nm, well comparable with the semiconductor ideal thickness. The *contact edge profile* is smooth, the film increases gradually for around 10 µm length to achieve the final height. The coffee ring effect is more marked compared to the thick contacts, around 10÷20 nm. These features should allow a continuous distribution of the semiconductor when deposited by gravure printing.
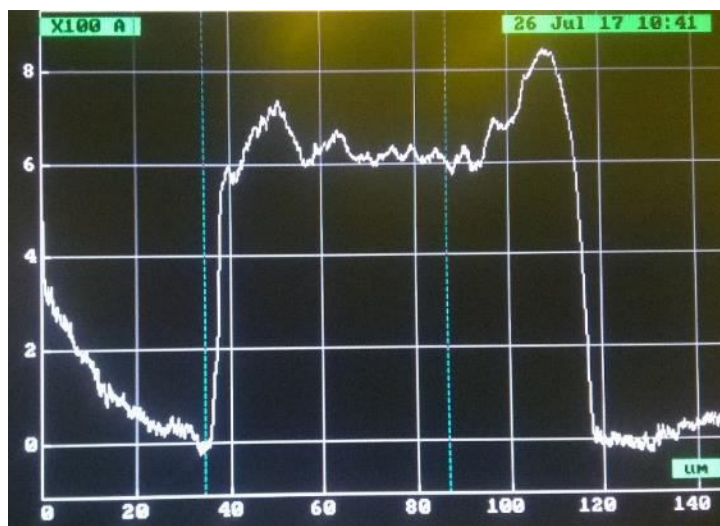
Fig. 18 Profile of the silver inkjet printed thin contacts, contact width ≈ 85 µm, contact thickness ≈ 60 nm.

2.3.3. Registration accuracy

The substrate alignment procedure has been studied to ensure a suitable registration accuracy when the gravure printing system is combined with the inkjet one. This optimization avoids the necessity of using wide tolerances in the layout definition, enabling the device scaling. For this thesis

work, this optimization has been carried out in order to improve the reproducibility among different printing processes and to avoid some issues due to misalignments.

The *inkjet printer alignment system* is optical, the position of the printing origin is defined by the user on the substrate. In this thesis, for the OTFTs realization the reference has been the upper left angle of the substrate. The substrate rotation can be modified, again through an optical control. The reproducibility is ± 25 µm, the camera field of view has a resolution of 2.54 µm per pixel.

The *alignment system of the gravure printer* used for this thesis work is mechanical, through the substrate clamping on the right side of the substrate. Accuracy and reproducibility is ensured to be < 100 µm. The PEN substrate used has not shown stretching in the printing direction, considering a maximum substrate length of 21 cm, the pressure dial used for this thesis work and avoiding excessive blade loads. Two registration errors introduced by the gravure printer have been observed, a translation and a rotation (Fig. 19).
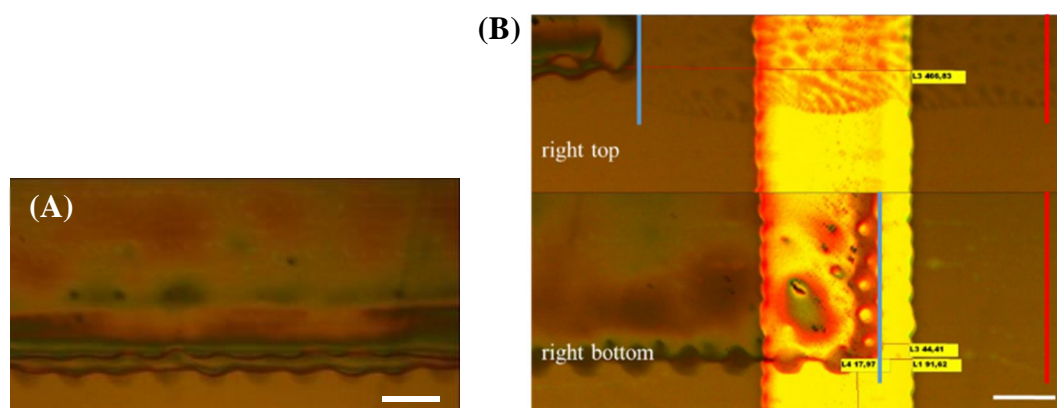
Fig. 19 A) Optical microscopy of misalignments among three layers subsequently printed. B) Registration error in rotation, the measurements at the sample edges are shown. The red bar is the ideal position of the gravure printed layer, the blue bar is the effective one. Scale bar 100 µm.

The first is an error in the printed pattern positioning, a **rigid translation** around tens of microns, both in the printing direction and in its perpendicular (Fig. 19 A). This error can be overcome only considering the proper tolerance during layout definition for the gravure cliché.

The second is a **rotation in the substrate**, the error is fixed and repeated precisely at each printing process. This error is most critical for the OTFTs process developed during this thesis work, since it requires the mechanical alignment of gravure printed layers on the inkjet printed bottom contacts. As shown in the optical microscopy pictures (Fig. 19 B), the misalignment effects partially exposes the electrodes, which is not desirable for electrical performance stability in time. The error

in positioning in the horizontal direction is -680÷-260 μm, widely out of the maximum pattern tolerance, ± 215 μm. The measured rotation angle is ≈ -0.35°.

To reduce as much as possible the registration errors, a rotation has been imposed to the substrate before inkjet printing (Fig. 20).
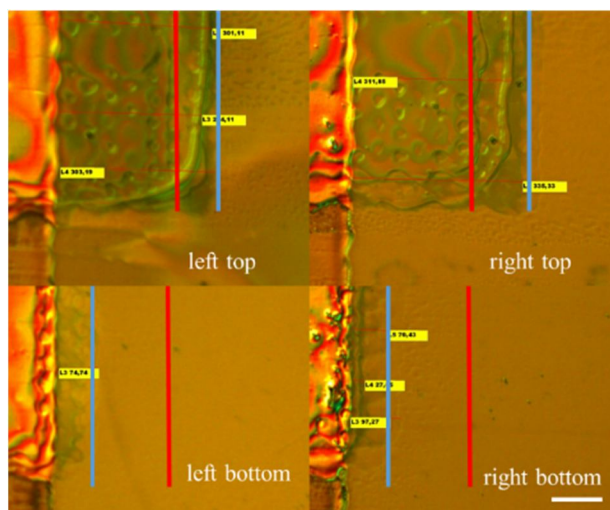
Fig. 20 Effect of the registration improvement on the printed samples, the measurements at the sample edges are shown. The red bar is the ideal position of the gravure printed layer, the blue bar is the effective one. Scale bar 100 μm.

The maximum error in positioning has been measured as -145÷85 μm, in the range of tolerance. This optimization has ensured a registration accuracy ±150 μm, avoiding issues due to misalignments between the layers deposited with different printing systems.

3. Pedot ink

The ink used for this thesis work has been the Clevios™ P Jet 700, a high conductivity (700 S/cm) water based PEDOT:PSS solution.

Before filling the cartridge, the material has been sonicated in an US bath for 1 h, left for 1 h, procedure repeated 3 times, then filtered with a 0.22 μm PVDF filter (Millex®-HV, Merck Millipore Ltd.).

The **process parameters** have been optimized and defined as follows.

- ejected drop volume: 10 pl
- platen temperature: disabled
- cartridge temperature: disabled
- jetting frequency: 10 kHz

- meniscus set point: 5.0 inches H_2O

- drop space: 30 μm

- cartridge cleaning cycles: before print *interstmp*; idle *start* every 240 s

- waveform: *pedot*

The annealing has been conducted at 80°C overnight in oven.

This procedure has been mainly used for the devices defined by lithography, to fill the via hole gap in order to ensure the electrical conductivity of the electrodes (Fig. 21 B). The precision in positioning and the required resolution is quite high, as the ink should not cross the S/D electrodes (in orange in Fig. 21 B). The metal is thermally evaporated aluminium, while the polymeric encapsulation is a teflon-like material. It has not been observed a significant difference in the ink-substrate interaction between these two materials. The drop diameter is ≈ 50÷60 μm. Two layers have been printed subsequently with a delay of 10 s.
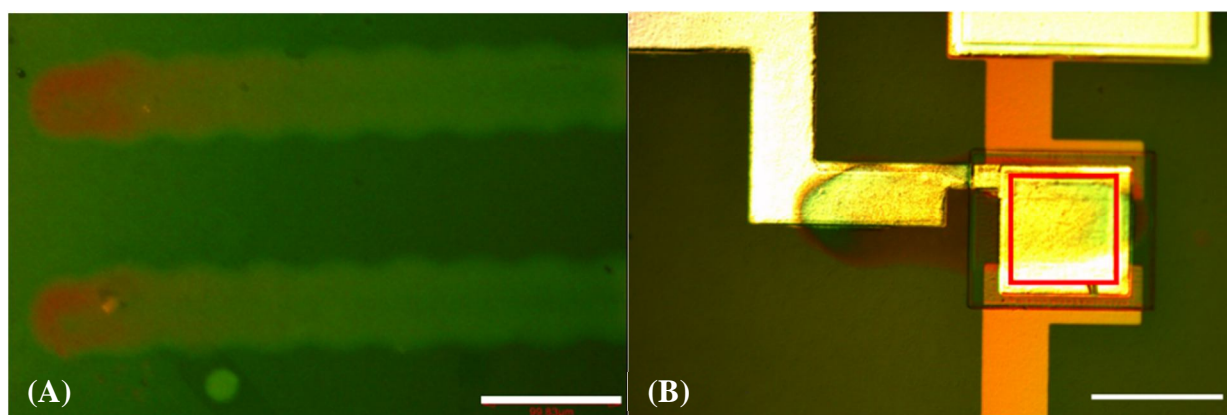
Fig. 21 PEDOT:PSS inkjet printing outcomes. (A) Lines on the teflon-like material. (B) The final application, in red the via hole perimeter. Scale bar 100 m.

4. Carbon ink

Possible applications for the OTFTs are the realization of pressure sensors, coupling a transistor with a capacitor and two proper resistances, or integrated circuits, such as inverters with resistive load. The development of **resistors** realized with printing techniques has been implemented for these particular applications. The requirement for pressure sensors has been to obtain 2-8 MΩ in printable areas smaller than 2 mm^2, while for the inverters is around tens of MΩ in printable areas smaller than 1 mm^2.

The ink used for these tests is the 3804 Carbon Ink Composition, by Methode Electronics, Inc. The nominal resistivity for this material is 3000 Ω/sq.

Before filling the cartridge, the material has been sonicated in an US bath for 1 h, left for 1 h, procedure repeated 3 times, then filtered with a 0.45 µm PVDF filter (Millex®-HV, Merck Millipore Ltd.).

The printing conditions have been optimized and the **process parameters** have been chosen as follows:

- ejected drop volume: 10 pl

- platen temperature: disabled

- cartridge temperature: disabled

- jetting frequency: 5 kHz

- meniscus set point: 4.0 inches H_2O

- drop space: 20 µm

- cartridge cleaning cycles: before print *start*; during print *interstmp* every 200 bands or 180 s

- waveform: *Cink1*

The annealing has been conducted at 80°C for 2 h 30 min in oven. The drop diameter is ≈ 50 µm on the substrate, a spin-coated PVDF.

The pattern is schematized in Fig. 22 A, while the printing outcomes are shown in Fig. 22 B.
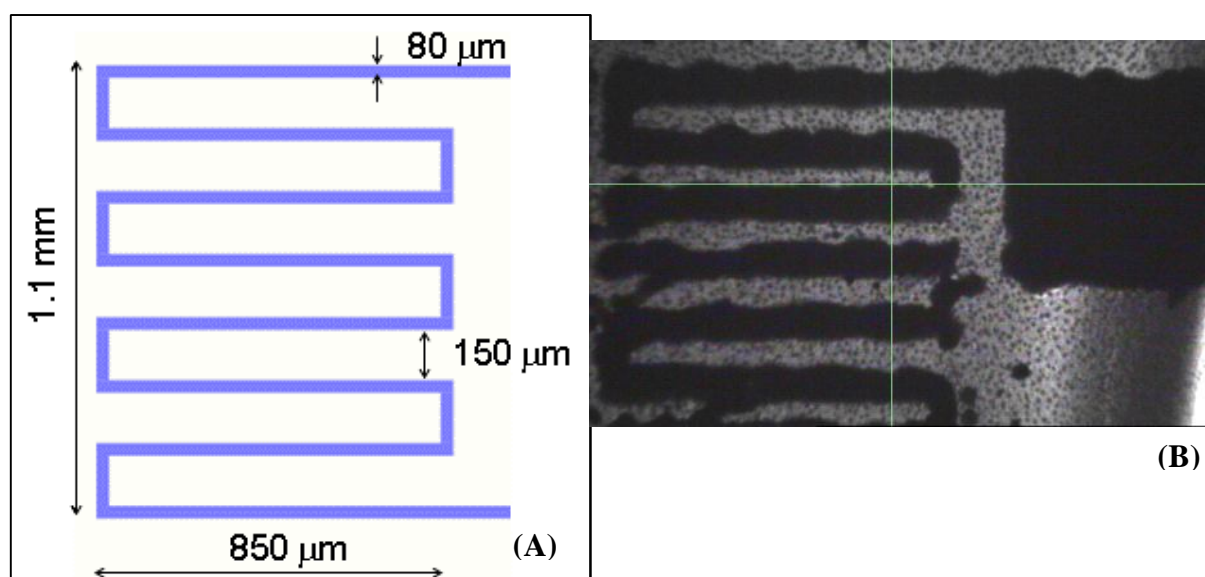
Fig. 22 (A) Layout of the resistors deposited with the 10 pl drop volume.
(B) Picture of the resulting printing outcome.

The final thickness of the resistor realized is ≈ 1.3 µm and the resolution is quite poor, as a consequence of the ink spreading on the substrate. This reduces the achievable resistance, as shown by the **electrical characterization** (Fig. 23), performed using the Suss PM5HF Analytical Probe Station equipped with a Hewlett Packard HP 4145B semiconductor parameter analyser.
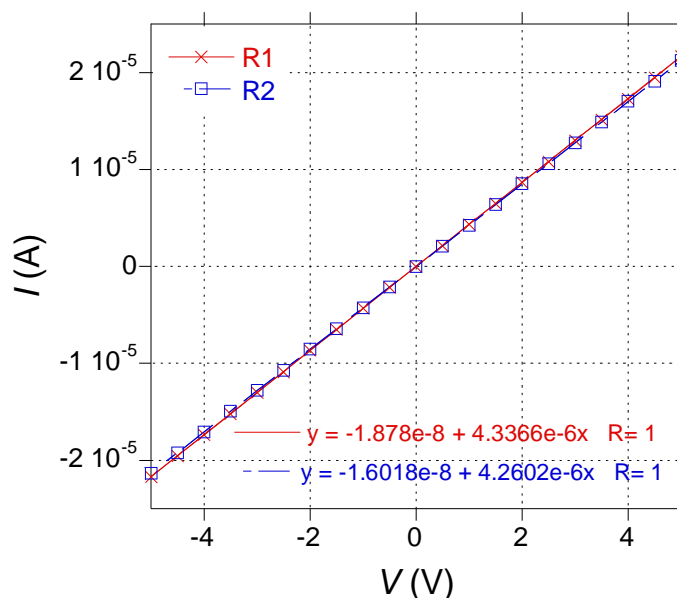
Fig. 23 I-V characteristics of two inkjet printed resistors, drop volume 10 pl.

The resistance achieved is ≈ 0.2 MΩ, resistivity ≈ 1600 Ω/sq, one order magnitude lower than the required value for the application.

To increase the resistance, a procedure with the 1 pl drop volume has been developed, in order to print longer and thinner serpentine patterns without interconnections and covering the same area. On the other hand, due to the high PVDF roughness, it is not possible to realize too thin resistors, as it would generate discontinuities.

The main issue has been to avoid nozzle clogging. The ink has been stirred 4 h before the US bath, the filled cartridge has been left in a bowl with water and saturated with humidity for 1 day before printing.

The **process parameters** have been optimized and defined as follows:

- ejected drop volume: 1 pl
- platen temperature: disabled
- cartridge temperature: disabled
- jetting frequency: 4 kHz
- meniscus set point: 4.0 inches H_2O

- drop space: 15 µm

- cartridge cleaning cycles: before print clog

- waveform: *Cink2*

The annealing has been conducted at 80°C for 2 h 30 min in oven. The drop diameter is ≈ 25 µm on the substrate, the spin-coated PVDF.

In Fig. 24 A the optical microscopy image of the resulting resistor, printed area 1 mm^2. The length is 7.85 mm, the width ≈ 30 µm. Fig. 24 B shows the **electrical characterization** for two different thicknesses, obtained printing one or two layers sequentially, resulting respectively R1 ≈ 700 nm and R2 ≈ 1.4 µm. The resistances have been measured as 5.3 and 2.4 MΩ respectively, compatible with the expected values for the sensor application, while the resistivity was ≈ 1.36 Ωcm.

(A) **(B)**
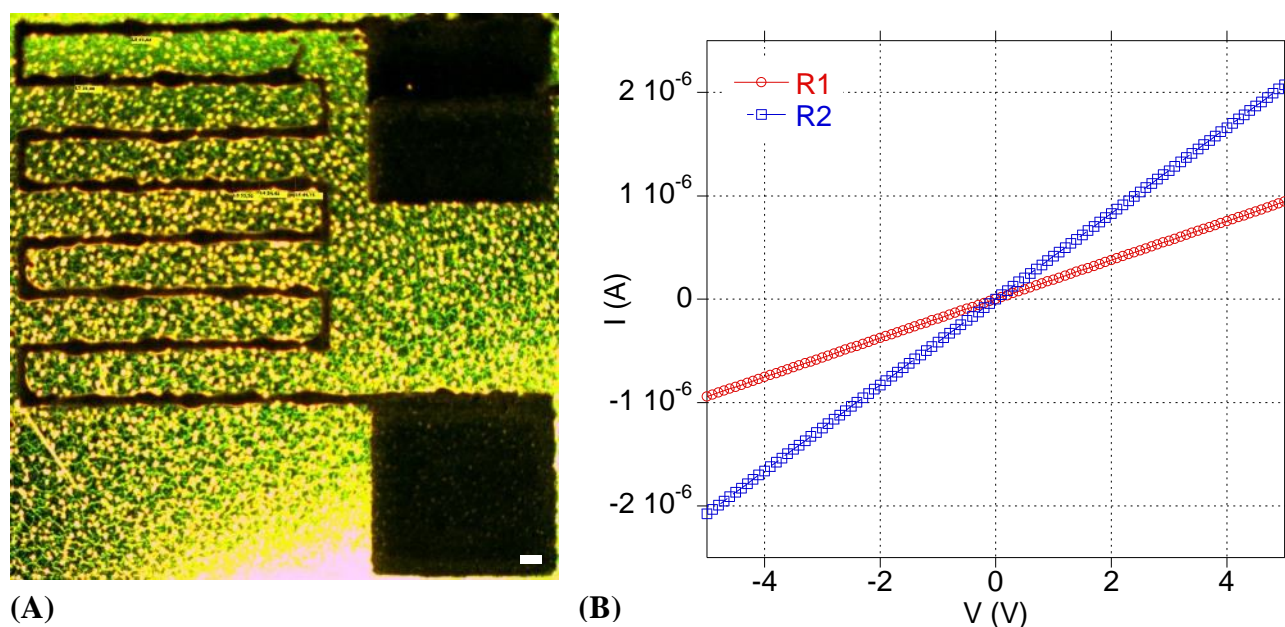
Fig. 24 A) Inkjet printed resistor with 1 pl drop volume. Scale bar 50 µm. B) I-V characteristics of two different thickness resistors: R1 ≈ 700 nm, R2 ≈ 1.4 µm.

The resistance is still quite low for inverters, as the ink has some bulging effect due to the substrate inhomogeneity. To further increase the resistance value, the PVDF deposition has been optimized in order to obtain a more uniform film. The **process parameters** have been modified to fit these new conditions as follows.

- ejected drop volume: 1 pl

- platen temperature: disabled

- cartridge temperature: disabled

- jetting frequency: 5 kHz

- meniscus set point: 4.0 inches H_2O

- drop space: 15 μm

- cartridge cleaning cycles: before print *start*; during print *interstmp* every 200 bands or 180 s

- waveform: *Cink1*

The annealing has been conducted at 80°C for 2 h 30 min in oven. The drop diameter is ≈ 25 μm on the substrate, the spin-coated PVDF.

Fig. 25 A shows the optical microscopy image of the resulting resistor, printed area 1 mm^2. The resistor length is 7.96 mm, the width ≈ 25 μm, the height ≈ 300 nm. Fig. 25 B shows the **electrical characterization** of the resistor. The measured resistance has been ≈ 17 MΩ, while the calculated resistivity has been ≈ 1.58 Ωcm.

(A)   **(B)**
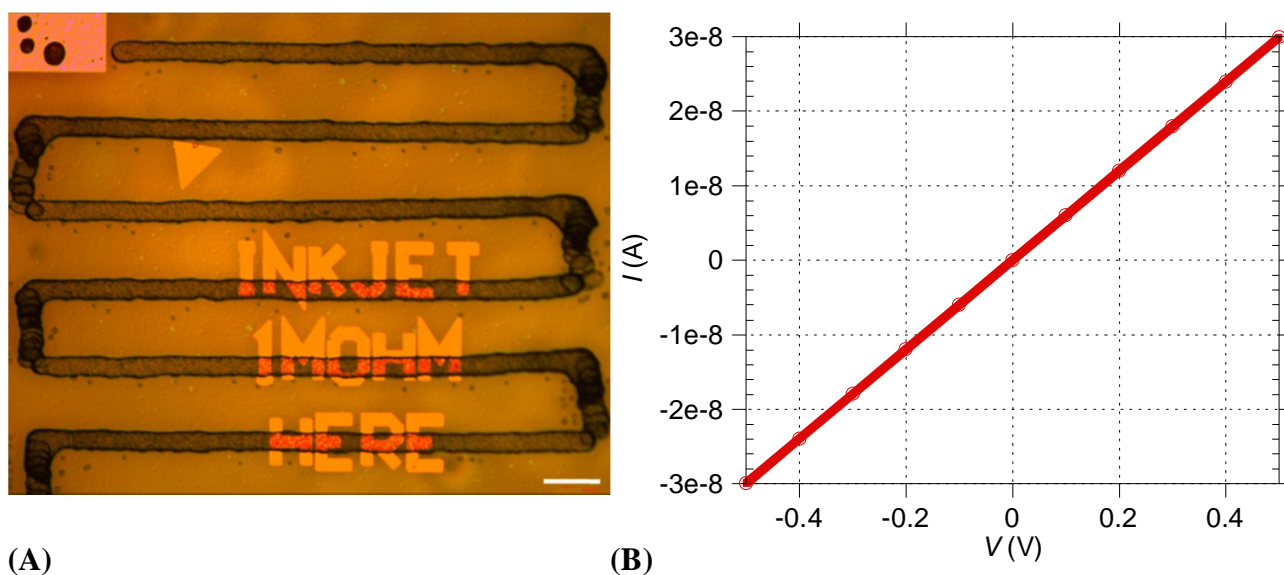
Fig. 25 A) Inkjet printed thin resistor, with 1 pl drop volume. Scale bar 100 μm. B) I-V characteristics.

The resistances obtained using the last two procedures, with drop volume 1 pl, have shown controlled values of resistances in the correct range for the applications, with low area waste, in total 1 mm^2.

References

(1)   Fukuda, K.; Someya, T. Recent Progress in the Development of Printed Thin-Film Transistors and Circuits with High-Resolution Printing Technology. *Adv. Mater.* **2016**.

(2)   Khan, S.; Lorenzelli, L.; Dahiya, R. S. Technologies for Printing Sensors and Electronics Over Large Flexible Substrates: A Review. *IEEE Sens. J.* **2015**, *15* (6), 3164–3185.

(3)   *DMP User Manual*, Rev.15 Ver. 1.6.0.1.; © FUJIFILM Dimatix, Inc. 2230 Martin Avenue · Santa Clara, CA 95050 · USA Technical Support Phone: (408) 565-7474, 2007.

(4)   Kahn, B. E. Patterning Processes for Flexible Electronics. *Proc. IEEE* **2015**, *103* (4), 497–517.

Chapter 5
Fully printed thin film transistors

1. Layout definition and fabrication procedure remarks

By using the modified gravure printer and the refined inks both deposited by gravure and inkjet technique, partially or fully printed OTFTs in staggered BCTG configuration have been realized. The layout for the definition of OTFTs has been settled as reported in Fig. 1.
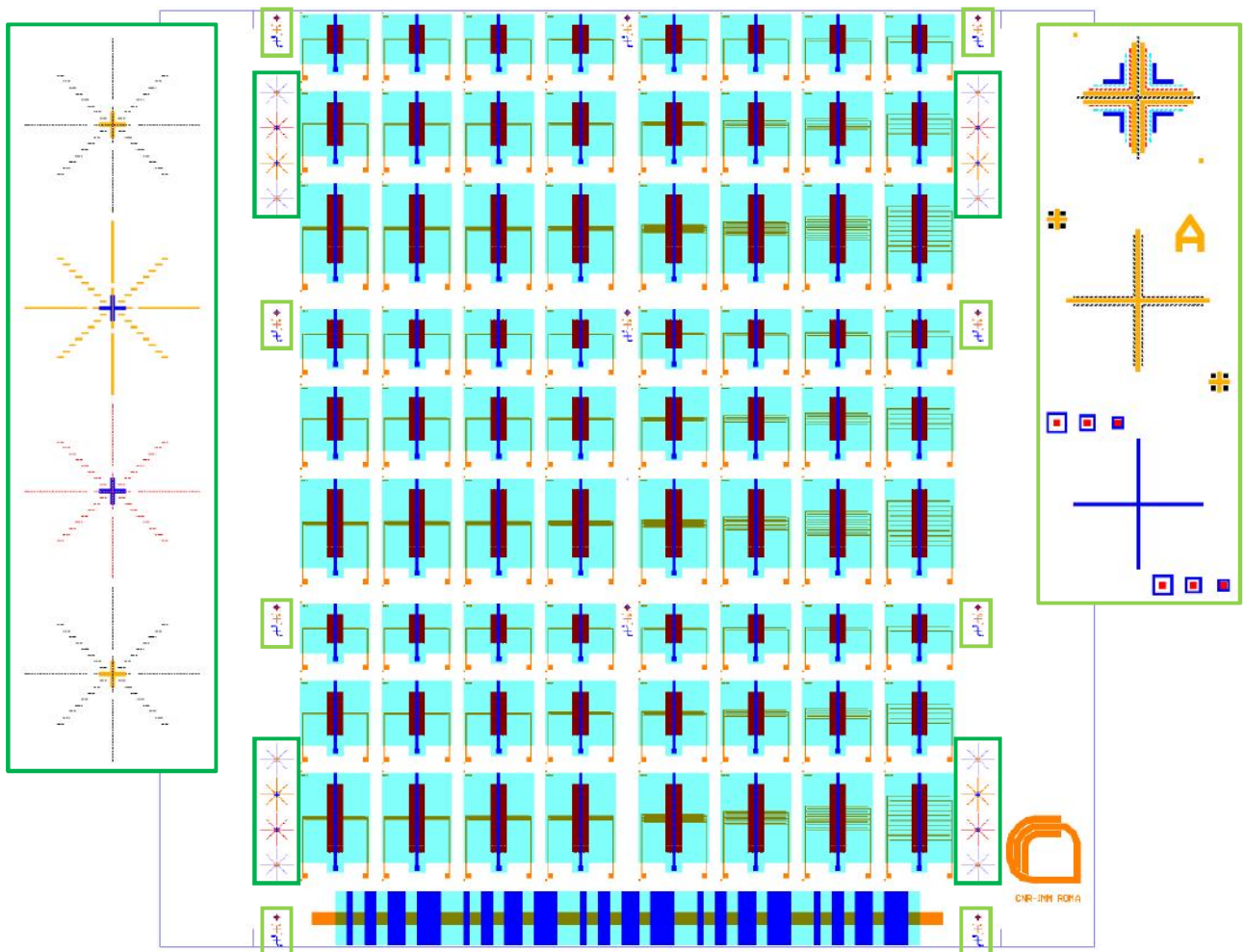
Fig. 1 Layout of the OTFTs cliché set. Black: pre-align – orange: S/D – red: OSC – light blue: dielectric – blue: gate. The alignment markers are highlighted in the green rectangles.

The substrate dimensions are 10x10 cm. The layout consists of 9 lines of transistors and one line for MIM devices testing, to evaluate the quality of the dielectric layer for each sample.

The **pre-alignment** layer pattern has been designed for a cliché realization, as reported in Paragraph 2.1.1.1.

The **S/D** layer is patterned on the substrate by laser lithography for the gold contacts thermally evaporated or reproduced on the Dimatix CAD software to realize the inkjetted contacts. For the organic contacts a cliché has been realized, refer to Chapter 3, Paragraph 3 for further details.

The **OSC** and **dielectric** layers have been always deposited by gravure, so this pattern has been designed for the realization of the clichés.

The **gate** electrode pattern has been reproduced on the Dimatix software to realize the inkjetted contacts. The gate contacts have been always realized with inkjet printing technique instead of gravure, since it allows fast prototyping, while obtaining high resolutions, and, as known, this deposition technique can be integrated into roll-to-roll processes.[1]
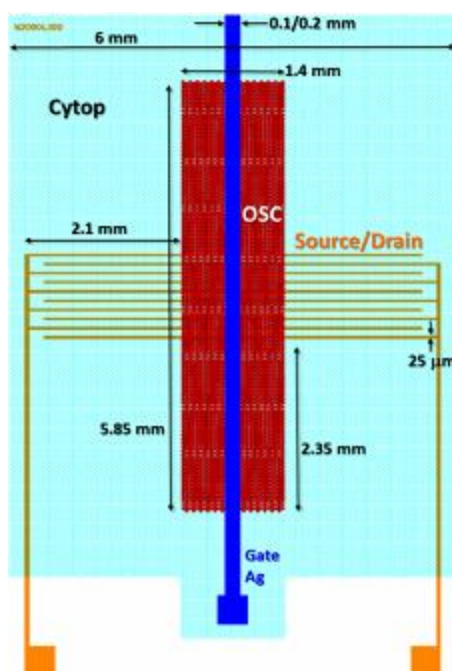
Fig. 2 Scheme of an OTFT.

The device dimensions (Fig. 2 B) have been decided evaluating the registration accuracy achievable with the gravure technique and the compatibility with the others deposition techniques used, considering still not corrected the error in rotation. Further details have been exposed in Chapter 4, Paragraph 2.3.3. The cell dimensions and shapes have been reported as the most performing ones during the ink printing procedure refinement (Chapter 3).

All steps of the **process** have been conducted in clean room. As substrate has been chosen a heat-stabilized, low roughness, 100 μm thick polyethylene-naphthalate (PEN) foil, Teonex® Q65HA, by DuPont. Before the process, each substrate has been cleaned with the usual procedure: cleaning in ultrasound bath, 2 min in acetone and 3 min in IPA. All curing temperatures have been kept below 120°C to avoid any substrate shrinkage.

For the optimized *gravure system configuration* the reference is to Chapter 2.

The *inks* and their *optimized deposition process* have been yet described in the previous chapters. Refer to Chapter 3 for the printing procedure of the gravure printed semiconductor, dielectric and organic conductive layers. The procedures for the inkjet printed layers have been described in Chapter 4.
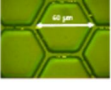
2. P-type transistors

Concerning the p-type devices, three different kind of S/D contacts have been tested, varying the material and the deposition technique:

- gold, thermally evaporated and patterned by laser lithography;
- silver, inkjetted;
- organic (PEDOT:PSS), gravure printed.

2.1. Gold source and drain

2.1.1. Fabrication procedure

SCHEME	Step	Deposition technique	Material	Annealing	Thickness
	Pre-align *	GRAVURE printing	CyAg	100°C oven	≈ 40 nm
	Source/Drain	thermal evaporation laser lithography wet etching **	Ti+Au	-	≈ 2+20 nm
	SAM	spin-coating	Merck	100°C hot plate	-
OSC plate typical cell	OSC	GRAVURE printing	Merck SP400	100°C hot plate	≈ 50 nm
OGI plate typical cell	OGI	GRAVURE printing	Cytop_A	100°C oven	≈ 400 nm
	Gate	INKJET printing	Ag ANP DGP40 LT-15C	80°C oven	≈ 200 nm

Fig. 3 Scheme of the fabrication procedure of OTFTs with thermally deposited S/D contacts. (*) Pre-align: the layer is deposited as defined in Paragraph 2.1.1.1. (**) As resist Microposit™ S1805™ G2 has been used, developed with the Microposit™ MF-319, both by DOW®. Wet etching for Au: 4 g KI, 1 g I_2, both by Carlo Erba, 40 ml H_2O, etch rate 2 nm/s; for Ti: deep in HF diluted in H_2O 1:20.

The OTFT channel length L ranges from 2 to 400 μm and their channel width W can be 100, 400 or 900 μm (Fig. 4).
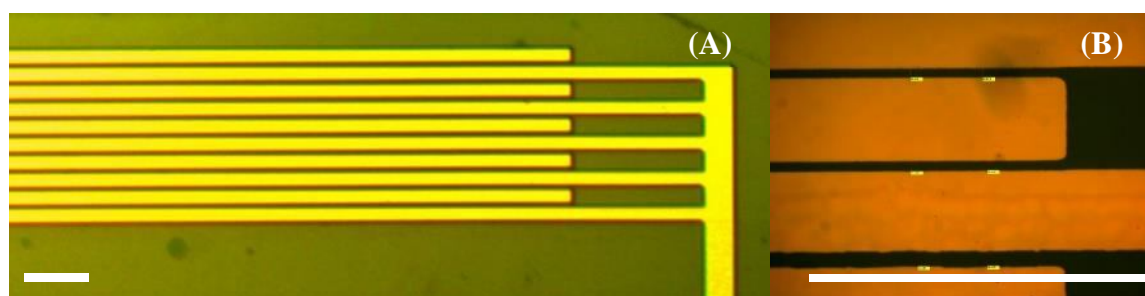
Fig. 4 Au S/D contacts defined by laser lithography. (A) Interdigitated configuration. (B) Minimum L device. Scale bar 100 μm.

2.1.1.1. Pre-alignment

A pre-alignment layer has to be gravure printed as reference for the laser lithography process in order to align the subsequent gravure printed patterns, OSC and dielectric, with the S/D contacts, defined by lithography. As alignment layer, it is required:

- to have a high registration accuracy;

- to be insulating, in order to ensure that short circuits between the S/D contacts will be avoided;

- to ensure a low lubrication layer, not to interfere with the morphology of the overlaying OSC;

- to be highly visible in black/white optical microscopy, in order to be clearly visible with the optical system of the laser lithography.

As initial formulation it has been chosen a CYTOP_B mixed with a silver nanoparticles based ink 20:1, ANP DGP40 LT-15C. The solution has been kept under magnetic stirring for 3 h. The printing procedure has been defined as follows:

- printing speed 0.3 m/s;

- pressure dial 5.98;

- pre-treatment on the cliché exposed at HMDS vapours for 15 min after a pre-heating at 120°C;

- blade E700/25/ST with step lamella profile (Esterlam Blades);

- annealing 1 h at 100°C in oven.

The printing outcomes are shown in Fig. 5.
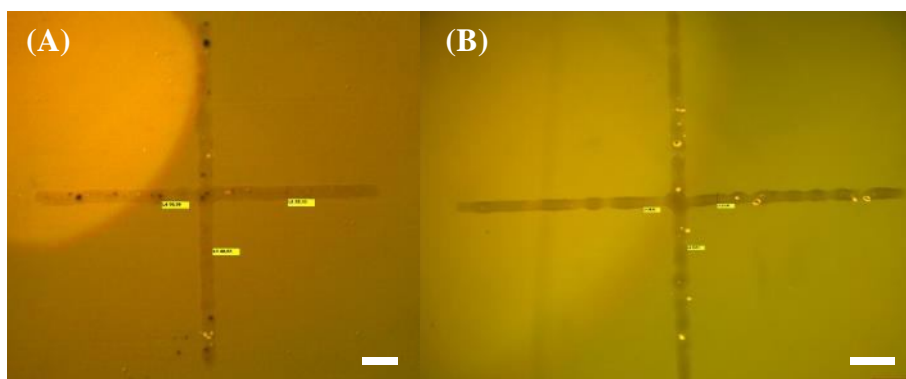
Fig. 5 Optical microscopy picture of the alignment marker, not optimized procedure. A) Before and B) after annealing. Scale bar 100 μm.

The printed film has not shown a homogeneous distribution of the silver, with some areas completely opaque.

The formulation has been modified, charging the CYTOP_B 5:1 with silver and stirring it overnight. The printing outcomes are shown in Fig. 6. The printing procedure followed has been the same as detailed above.
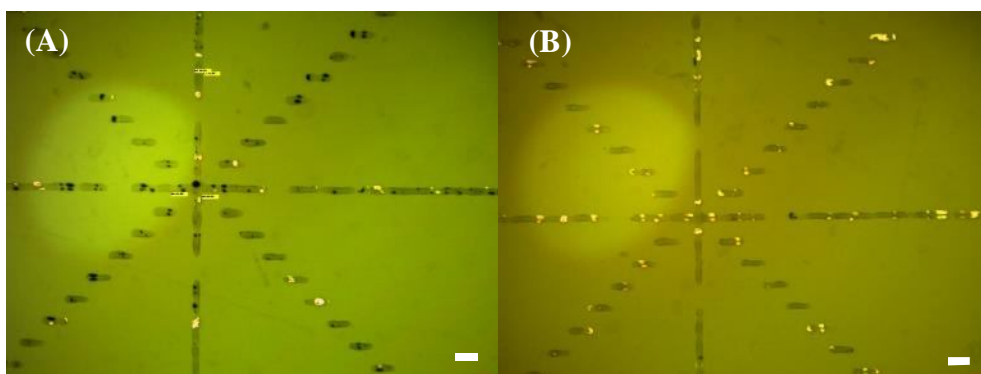
Fig. 6 Optical microscopy picture of the alignment marker, optimized procedure. (A) Before and (B) after annealing. Scale bar 100 µm.

The resulting film has shown to be suitable for the application. The layer height is ≈ 40 nm and it is not conductive. The lubrication layer has been reduced as the OSC layer morphology has not been damaged, as shown by the optical microscopy picture in Fig. 7.
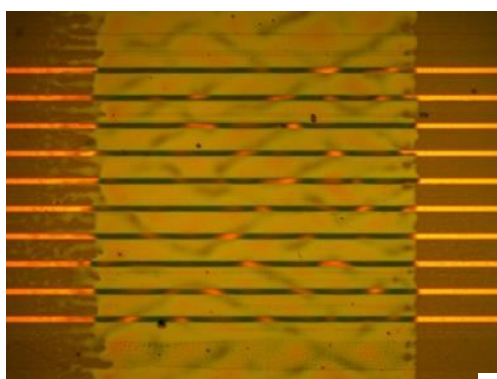
Fig. 7 OSC morphology. Scale bar 100 µm.

The cell shape and dimension, which have been chosen as the most appropriate, are shown in Fig. 8.
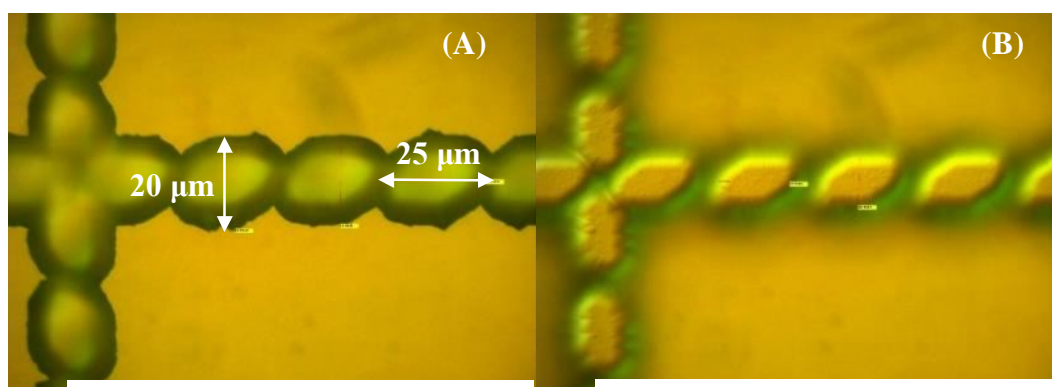
Fig. 8 Alignment marker in the centre of the mask (A) top and (B) bottom. Cell depth ≈ 6.7 µm. Scale bar 100 µm.

The registration accuracy obtained using these markers is shown in Fig. 9, it is widely under 20 µm in both directions.
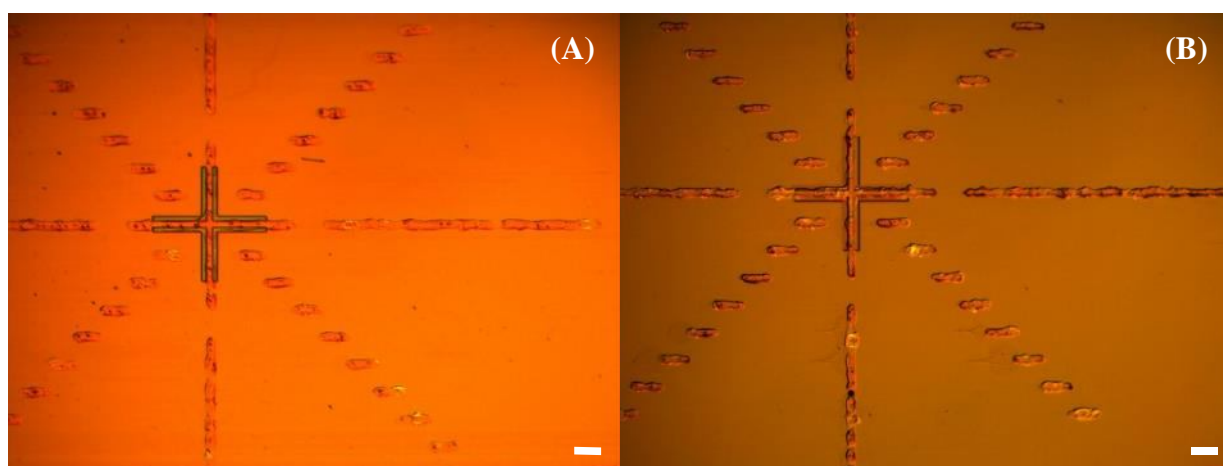
Fig. 9 Registration accuracy achieved between the pre-alignment layer and the S/D contact lithographically defined. Marker position on the sample: (A) top left and (B) top right. Lines width 20 µm. Scale bar 100 µm.

2.1.2. Electrical characterization
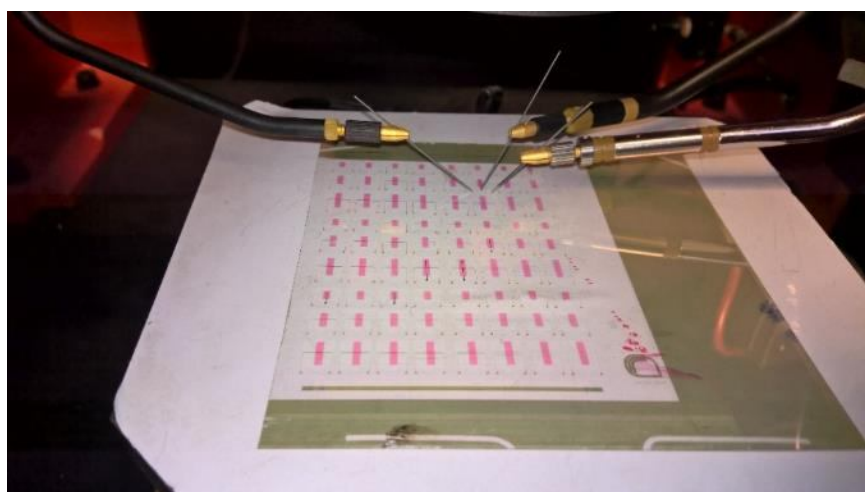
Fig. 10 Sample of OTFTs with gold S/D contacts under electrical characterization.

Representative up-down transfer characteristics, in linear and logarithmic scale, are shown in Fig. 11 A, while the transconductance and leakage current through the gate are reported in Fig. 11 B. The device considered is an $L = 100$ µm, $W = 400$ µm.
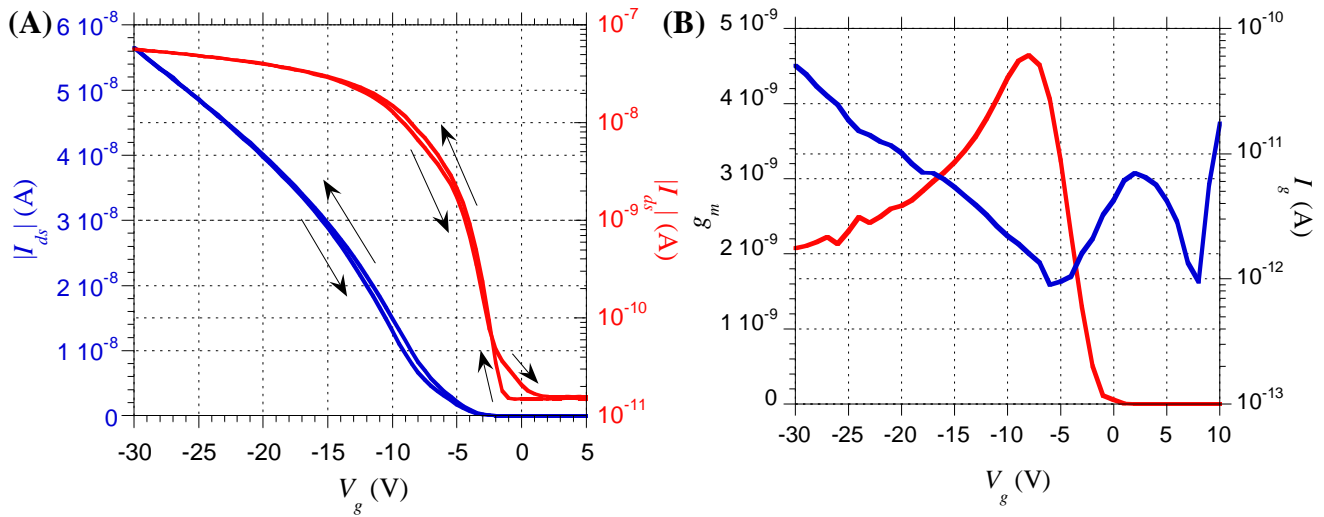
Fig. 11 (A) Representative up-down transfer curves of an OTFT with gold S/D contacts, V_{ds} = -1 V. (B) Transconductance and leakage current. L = 100 µm, W = 400 µm.

The main electrical parameters of the transistors have been calculated from the transfer characteristics measured at low V_{ds} (Fig. 11). The up-down curves show small hysteresis, with a V_{TH} shift around 0.8 V. The mobility μ_{LIN} is up to 0.22 cm²V⁻¹s⁻¹. A non perfect linearity has been observed in the ON-region, even for large channel lengths, suggesting a strong influence of the parasitic contact resistance. The devices show low threshold voltage, around -3 V, the I_{ON}/I_{OFF} is quite high, around $10^3 \div 10^4$. Gate leakage current is $I_{gs} < 100$ pA at $V_g = -30$ V, while the subthreshold slope is around 4600 mV/dec. These values of I_{gs} and SS suggest a not perfect quality of the printed dielectric layer and of the semiconductor/dielectric interface.
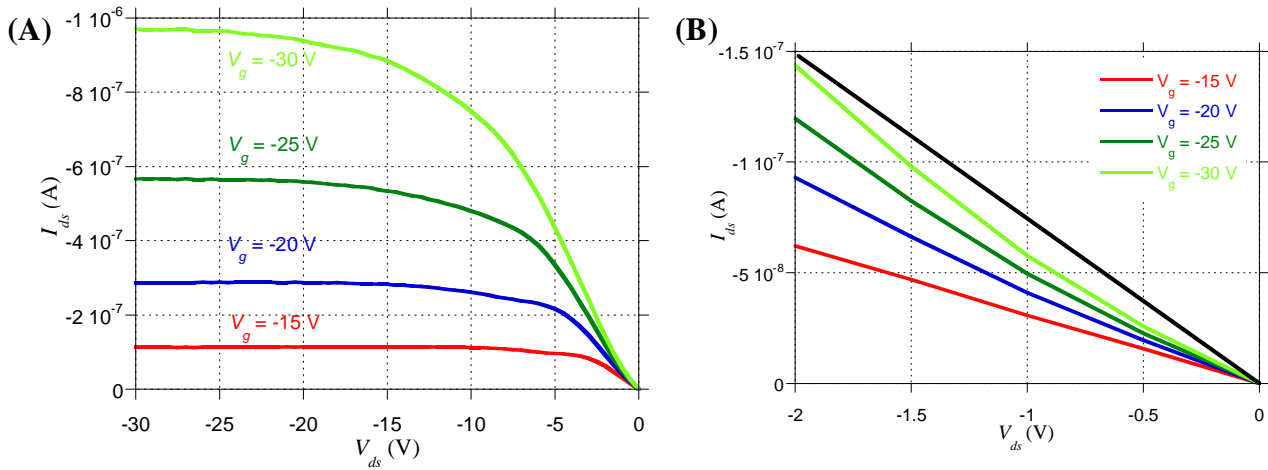
Fig. 12 (A) Representative output curves at different V_g of an OTFT with gold S/D contacts. (B) Magnification of the low V_{ds} area. Black line as guide for the eye. $L = 100$ µm, $W = 400$ µm.

Output characteristics (Fig. 12) do not show good linearity at low V_{ds} (Fig. 12 B), confirming the presence of parasitic contact resistance. This reveals that a significant energy barrier between the gold S/D contacts and the OSC is still present, even using the SAM functionalization.

2.1.2.1. Stability under bias stress

The stability of the devices when subjected to a negative **bias stress**, $V_{g,stress} = -30$ V, has been investigated. The **recovery** in dark and without applied bias has been evaluated at different times. The measurements for an OTFT with $L = 100$ µm, $W = 400$ µm are shown in Fig. 13.
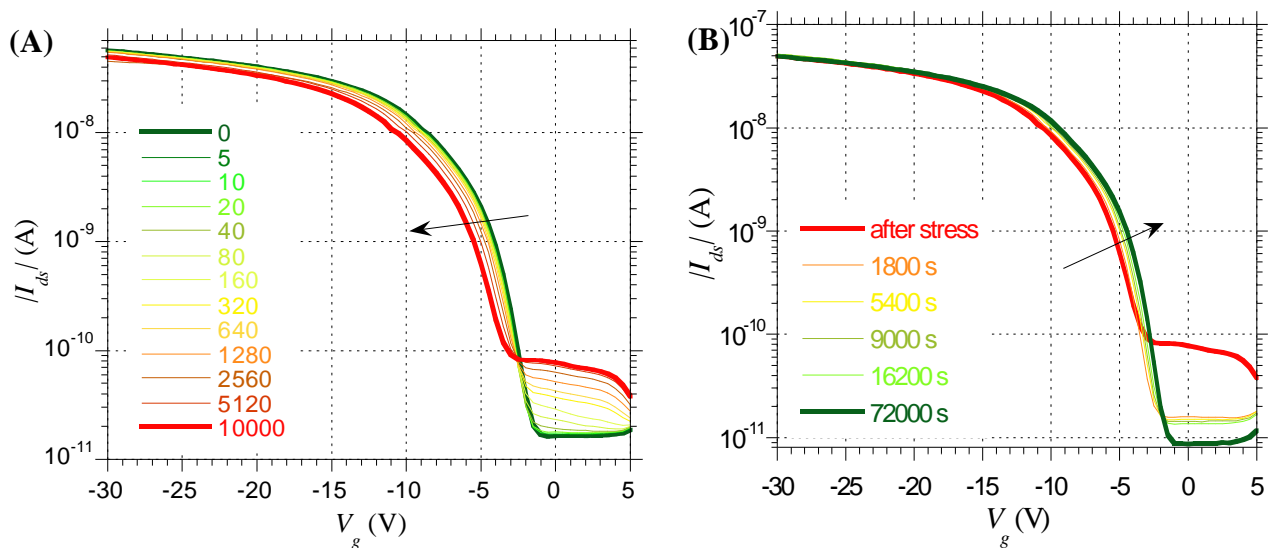
Fig. 13 Transfer characteristics of the OTFT under stress at different times (A) and stress recovery (B). $V_{g,stress} = -30$ V, $V_{ds} = -1$ V, $L = 100$ µm, $W = 400$ µm.

As a consequence of the applied bias, the characteristics show a shift of about 1.5 V towards more negative V_g, in the subthreshold region. An increase of the I_{OFF} can be also observed. The sensitivity of these devices to bias stress can explain the hysteresis measured in the transfer up-down curves (Fig. 11). On the contrary, the recovery shift toward right the curves and strongly lower the I_{OFF}, around one order magnitude.

The shift ΔV_g of the characteristics has been quantified evaluating the V_g variations in the subthreshold region as a function of time, both for the bias stress and recovery processes (Fig. 14).
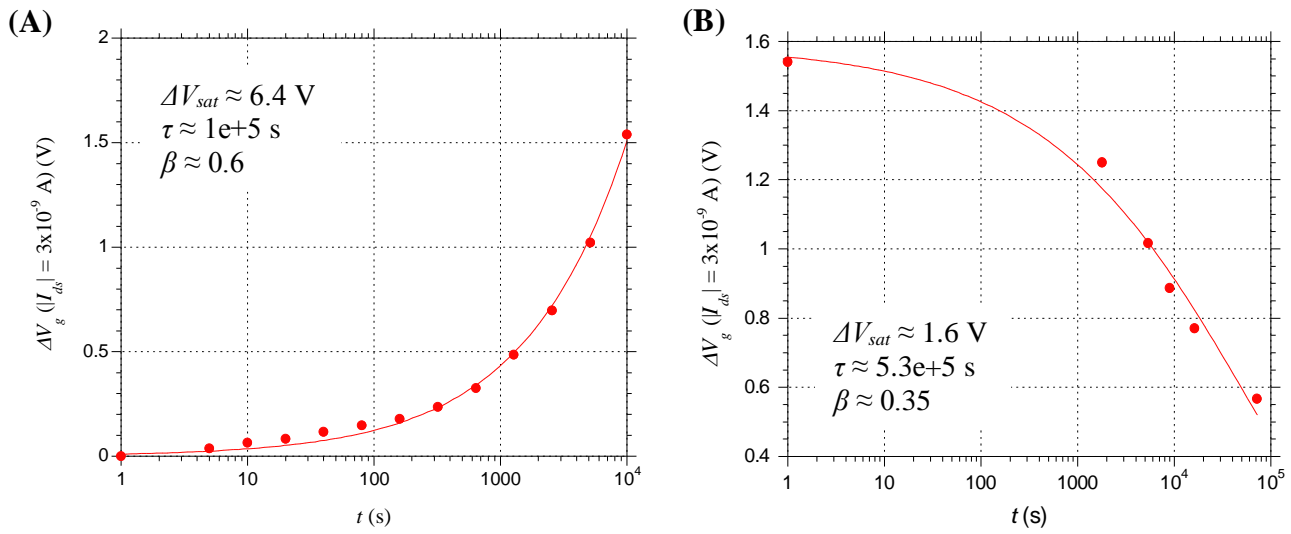
Fig. 14 Shifts of V_g subthreshold during the bias stress (A) and the recovery (B). $V_{g,stress}$ = -30 V, V_{ds} = -1 V, L = 100 µm, W = 400 µm.

Concerning both the bias stress and recovery ΔV_g, the process characteristic time is $\tau \approx 10^5$ s. However, even if the shift in the ON-region can be completely recovered, some instabilities in the OFF-region still affect the characteristics after 10^5 s.

2.1.2.2. Sensitivity to light

The device has been kept in dark to measure how the characteristics **recover** after a light exposure (5 min, low light), the measurements are shown in Fig. 15.
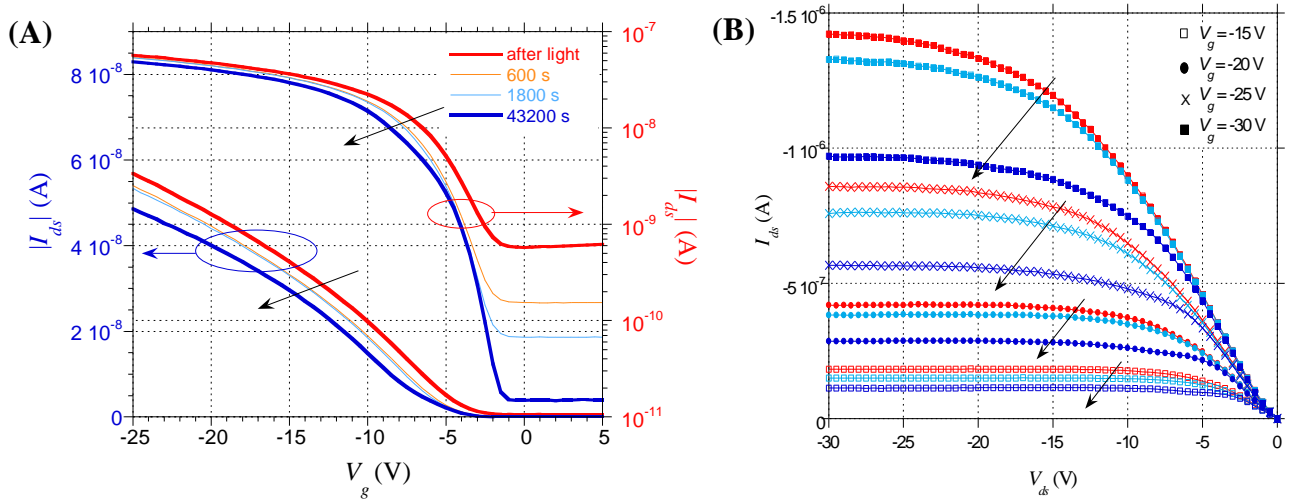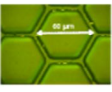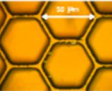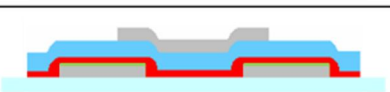
Fig. 15 Transfer, V_{ds} = -1 V, (A) and output (B) characteristics during the recovery from light exposure. Colour legend for recovery timing is the same for both graphs, as detailed in (A). L = 100 µm, W = 400 µm.

It has been observed a left shift of the transfer characteristics, around ≈ 2.2 V, and a significant decrease in the I_{ON}/I_{OFF}. The output characteristics shift in saturation, as $|V_g$-$V_{TH}|$ is lowered. No differences in the curve shape at low V_{ds} have been observed, maybe due to the contact effect. The recovery of the shift in the OFF-region is quite fast, as a shift ≈ 10^2 has been reached in 10^3 s.

2.2. Silver source and drain

2.2.1. Fabrication procedure

SCHEME	Step	Deposition technique	Material	Annealing	Thickness
	Source/Drain	INKJET printing	Ag ANP DGP40 LT-15C	100°C oven	≈ 160÷100 nm
	SAM	spin-coating	Merck	100°C hot plate	-
OSC plate typical cell	OSC	GRAVURE printing	Merck SP400	100°C hot plate	≈ 50 nm
OGI plate typical cell	OGI	GRAVURE printing	Cytop_A	100°C oven	≈ 400 nm
	Gate	INKJET printing	Ag ANP DGP40 LT-15C	80°C oven	≈ 200 nm

Fig. 16 Scheme of the fabrication procedure of OTFTs with silver inkjetted S/D contacts.

Devices channel length, L, and width, W, ranged from 30 to 400 µm and from 100 to 900 µm, respectively. A representative device is reported in Fig. 17 A.
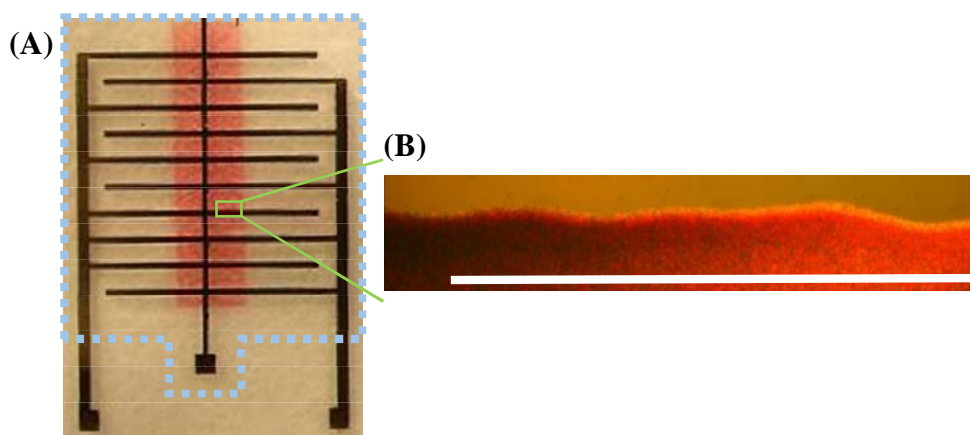
Fig. 17 (A) Fully printed OTFT with silver S/D contacts. The light blue dotted square indicates the dielectric. (B) Magnification of the OSC distribution over the contact edge. Scale bar 100 µm.

The OSC distribution over the edge on the S/D contact has been verified through optical microscopy (Fig. 17 B). It results to be continuous and conforming to the underlying layers.

2.2.2. Electrical characterization

Representative transfer curve of OTFT with silver S/D contacts, $V_{ds} = -1$ V, is reported in Fig. 18 A, the transconductance and leakage current calculated from this characteristic are plotted in Fig. 18 B. The device is an $L = 100$ μm, $W = 400$ μm.
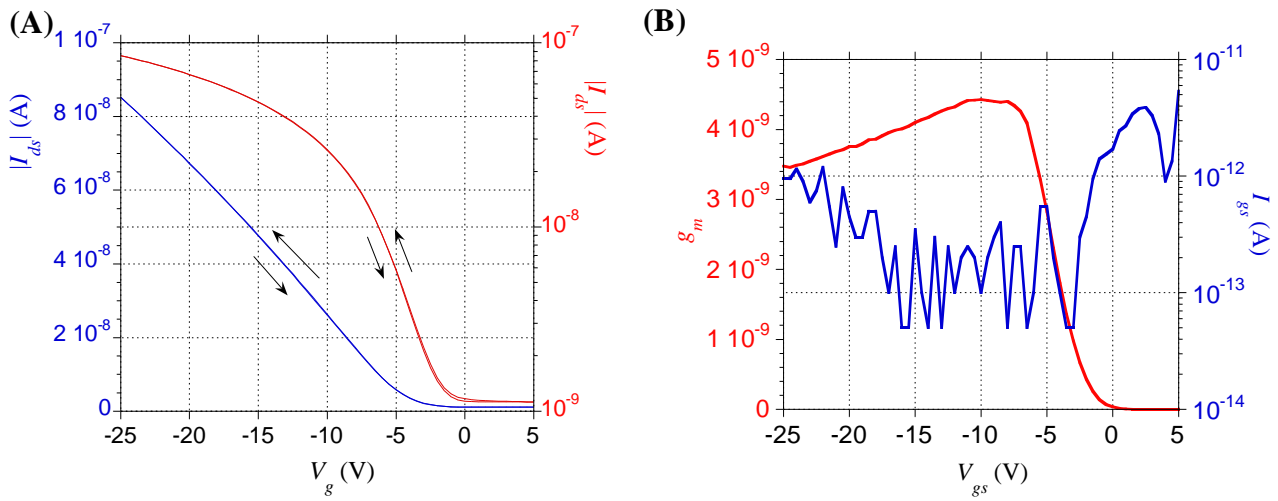
Fig. 18 (A) Representative transfer curves of a fully printed OTFT with silver S/D contacts, $V_{ds} = -1$ V. (B) Transconductance and leakage current. $L = 100$ μm, $W = 400$ μm.

The main electrical parameters of the transistors have been calculated from the transfer characteristics measured at low V_{ds}. The mobility μ_{LIN} is up to 0.24 cm^{2}V^{-1}s^{-1}, good linearity has been observed in the ON-region, even for shorter channel lengths, suggesting small parasitic contact resistance. The devices show low threshold voltage, around -4 V. Gate leakage current is very low, $I_{gs} < 2$ pA at $V_g = -20$ V, thanks to the high quality of the printed dielectric layer. The subthreshold slope is around 4500 mV/dec. The I_{ON}/I_{OFF} is quite low, around 10^2, however, as it will be explained in Paragraph 2.2.2.3, this issue can be completely attributed to the light effects. No hysteresis has been observed in the transfer characteristics.
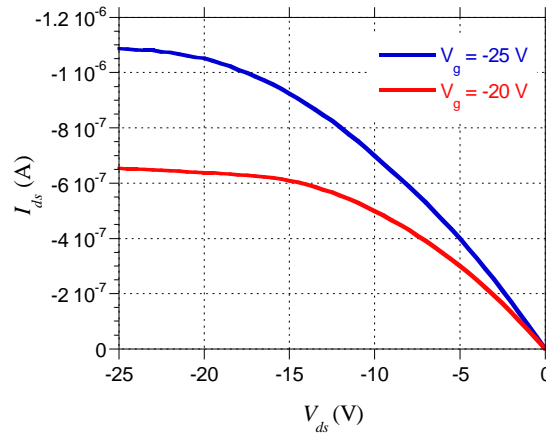
Fig. 19 Representative output curves of a fully printed OTFT with silver S/D contacts, $L = 100$ µm, $W = 400$ µm.

Output characteristics (Fig. 19) show good linearity at low V_{ds}, confirming a low parasitic contact resistance.

2.2.2.1. Contact effects

In Fig. 20 the measures to calculate the contact resistance with the TLM (refer to cap. 1 paragraph 3.2.1) are reported.
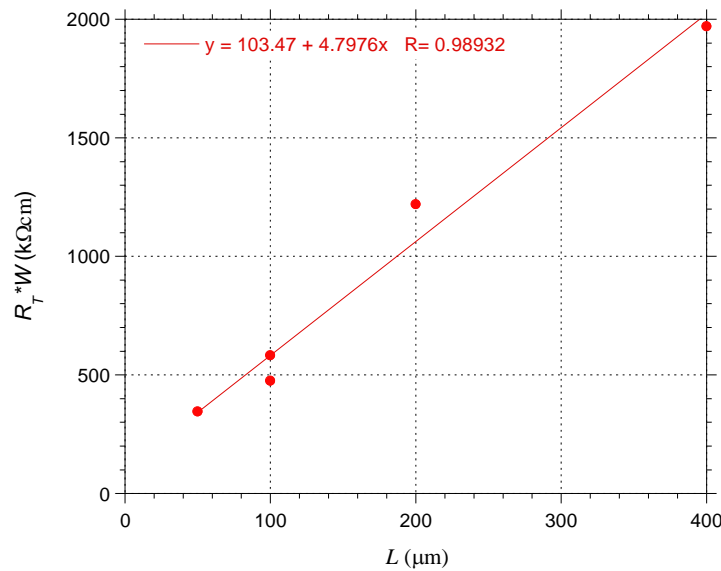
Fig. 20 Total resistance normalized with the channel width as a function of the channel length.

Although the devices show good linearity in the transfer and output characteristic, the R_c results to be around 100 kΩcm. This value suggests that these device performances could be then further improved optimizing the interface between OSC and S/D contacts.

2.2.2.2. Stability under bias stress

The OTFT stability under **bias stress** has been evaluated applying a $V_{g,stress}$ = -25 V, the transfer characteristics measured for a device L = 100 µm, W = 400 µm are reported in Fig. 21.
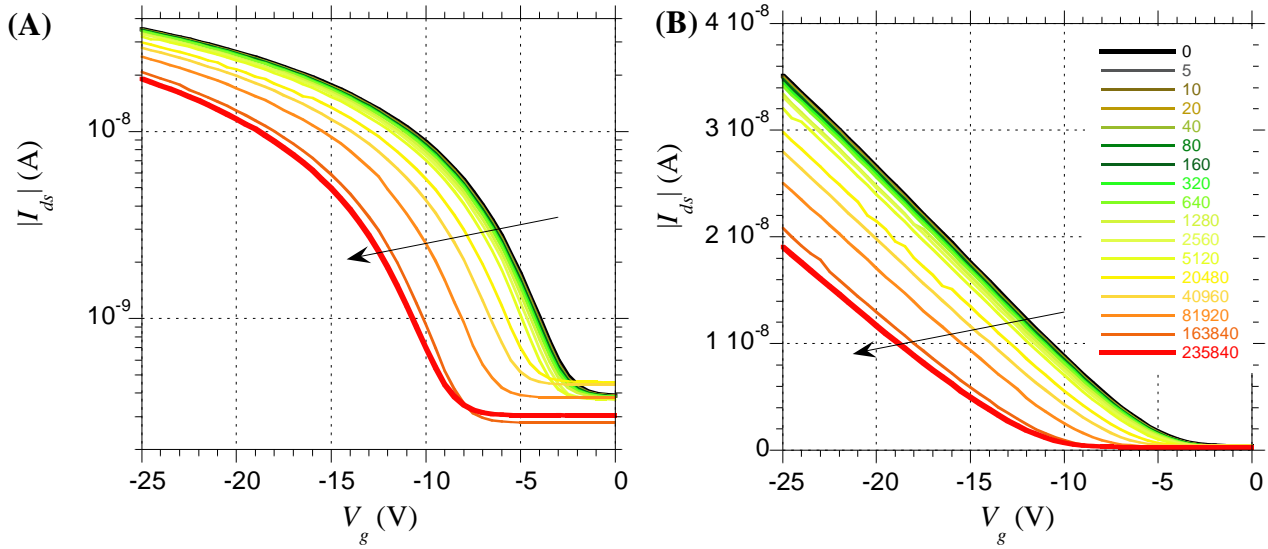
Fig. 21 Transfer characteristics of the OTFT under bias stress in logarithmic (A) and linear scale (B). $V_{g,stress}$ = -25 V, V_{ds} = -1 V, L = 100 µm, W = 400 µm.

The characteristics shift towards left, as a consequence of hole trapping in the dielectric or at the OSC interface due to the bias stress. The bias effect is also evident in the I_{OFF} fluctuations.

The V_g shift in the subthreshold region has been measured as a function of the stress time, the data have been then fitted as reported in Fig. 22.
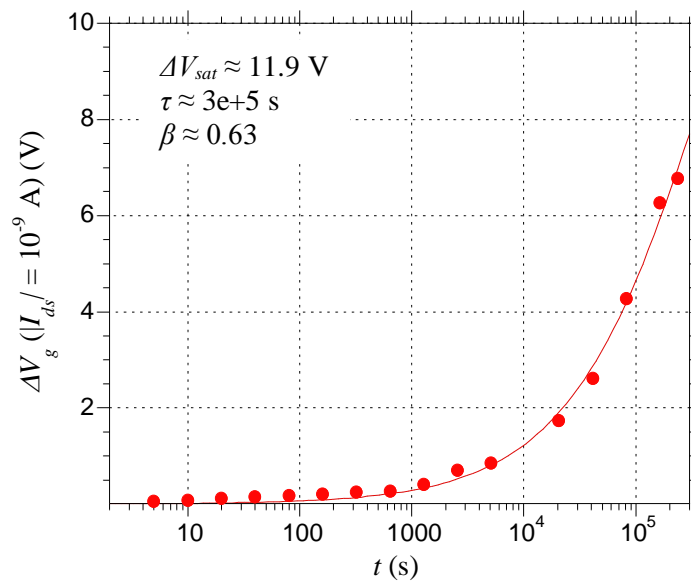
Fig. 22 Shifts of V_g subthreshold during the bias stress. $V_{g,stress}$ = -25 V, V_{ds} = -1 V, L = 100 µm, W = 400 µm.

The V_g shift is comparable to those of gold S/D and the characteristic time is slightly longer than 10^5 s.

The **recovery** of the device has been followed in time and the transfer characteristics are reported in Fig. 23.
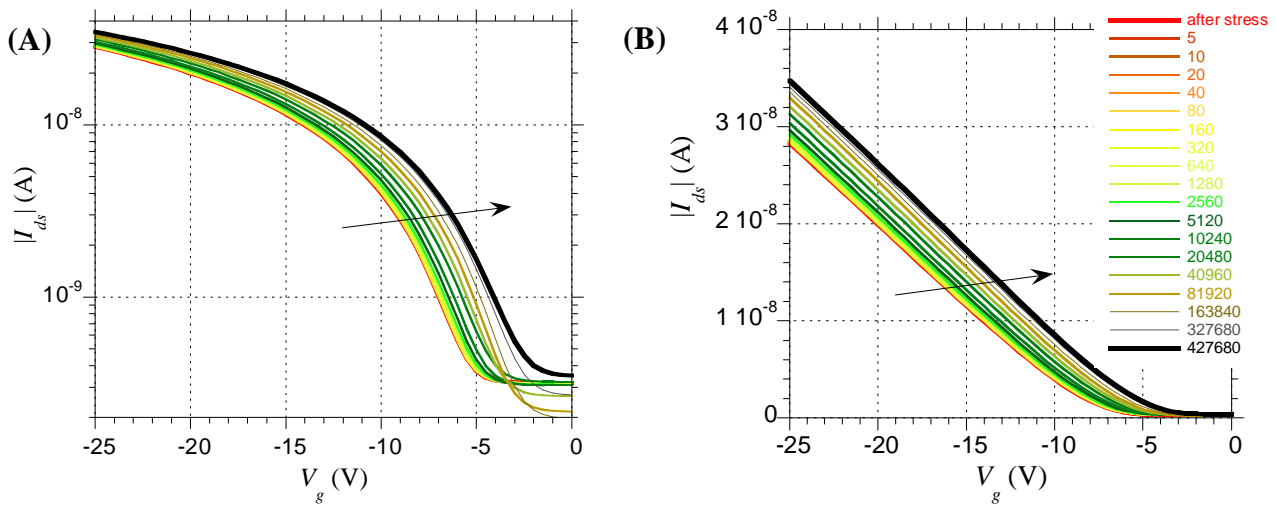
Fig. 23 Transfer characteristics of the OTFT under bias stress recovery in logarithmic (A) and linear scale (B). V_{ds} = -1 V, L = 100 µm, W = 400 µm.

The characteristics shift towards right and, as during the bias stress, the I_{OFF} shows some instabilities. Both effects have been completely recovered after $t \approx 10^6$ s.

The recovery trend is reported in Fig. 24.
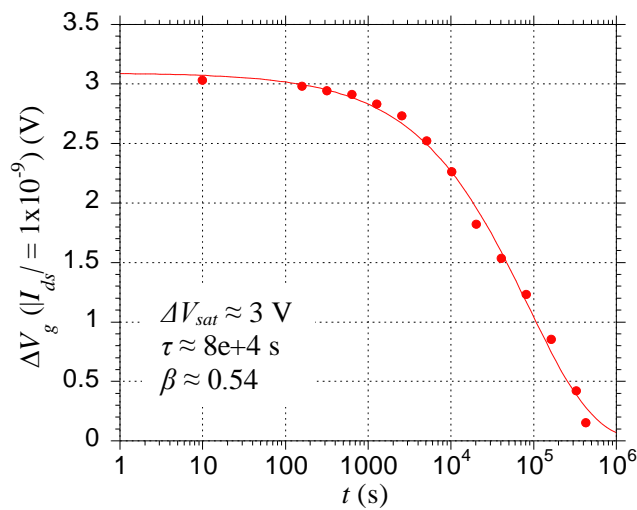
Fig. 24 Shifts of V_g subthreshold during the bias stress recovery. V_{ds} = -1 V, L = 100 µm, W = 400 µm.

The data have been fitted with the stretched exponential, the relaxation time results to be $\tau \approx 8 \cdot 10^4$ s, the dispersion parameter $\beta \approx 0.5$.

2.2.2.3. Sensitivity to light

Since the devices are sensible to bias stress, the **light stability** measurements have been conducted without applying a gate bias. The measurements are shown in Fig. 25.
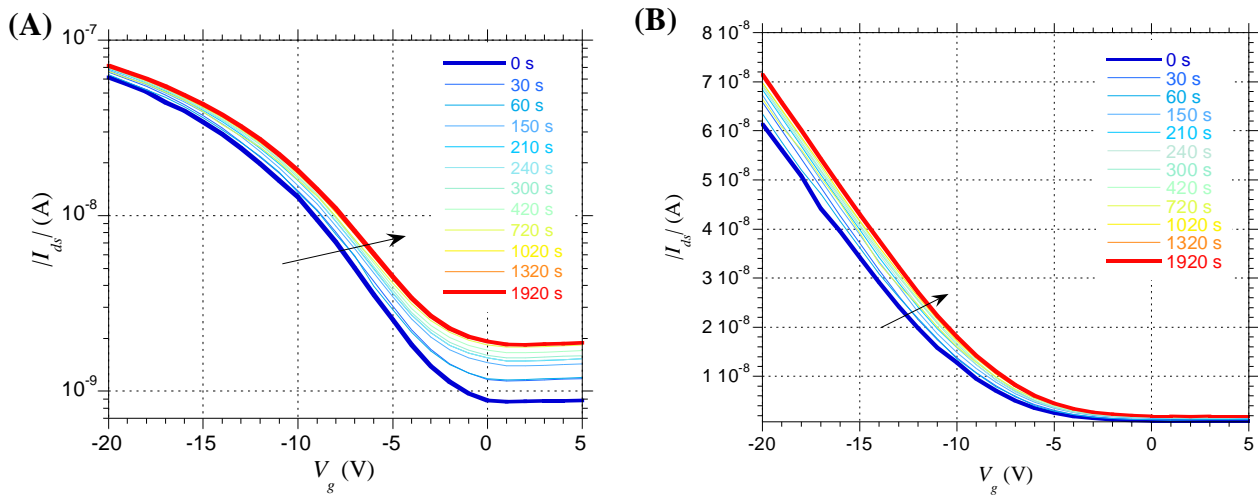
Fig. 25 Transfer characteristics in logarithmic (A) and linear scale (B) during the light stress, low intensity. $V_{ds} = -1$ V, $L = 400$ μm, $W = 400$ μm.

It has been observed a right shift of the transfer characteristics, around ≈ 1.2 V, and a significant decrease in the I_{ON}/I_{OFF}, mainly due to the I_{OFF} increase, with a stabilization of the characteristics after $\approx 10^3$ s of light exposure.

To evaluate the shift, the variations of the I_{ds} in the OFF-region and of the V_g for a fixed subthreshold I_{ds} have been calculated as a function of the exposure time and fitted, the results are reported in Fig. 26.

(A)

$\Delta I_{OFF,sat} \approx 1e\text{-}9$ A
$\tau \approx 237$ s
$\beta \approx 0.67$

(B)

$\Delta V_{sat} \approx 1.9$ V
$\tau \approx 421$ s
$\beta \approx 0.56$
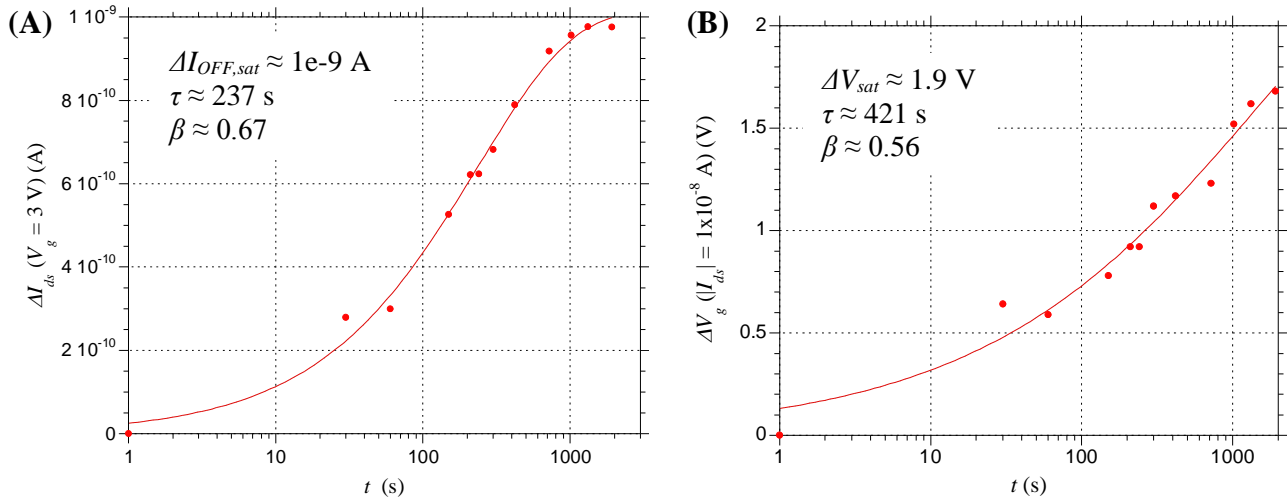
Fig. 26 Shifts of the I_{ds} in the OFF-region (A) and the V_g subthreshold (B) during the light stress, low intensity. L = 400 µm, W = 400 µm.

The curves can be fitted with a stretched exponential, as usual. The relaxation time results to be in the order of hundreds of seconds both for the I_{OFF} and for the subthreshold region.

The transfer characteristics measured during the stress **recovery** in dark are reported in Fig. 27.
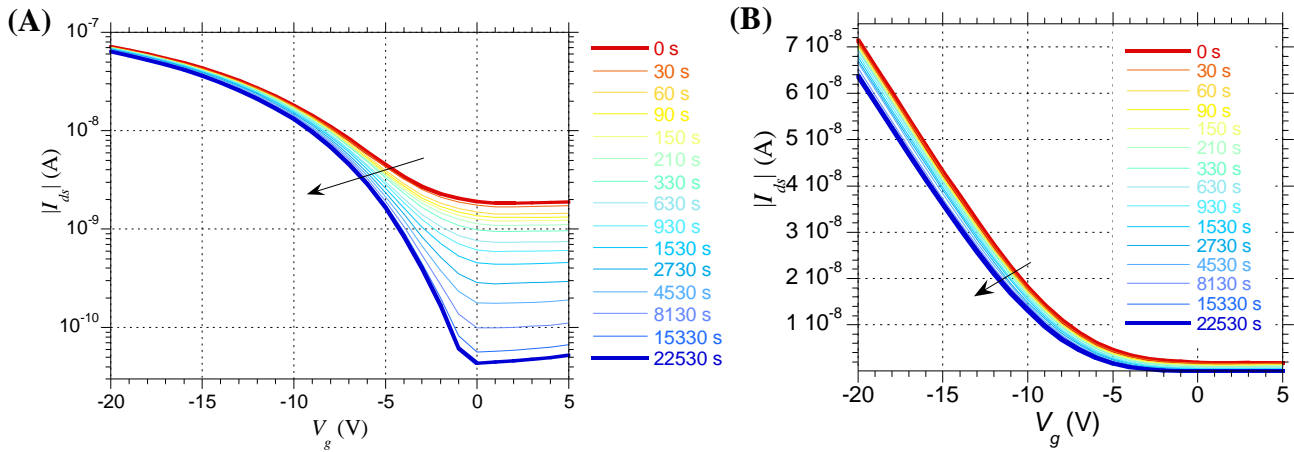
Fig. 27 Transfer characteristics in logarithmic (A) and linear scale (B) during the recovery. V_{ds} = -1 V, L = 400 µm, W = 400 µm.

It has been observed a shift towards the left in the characteristics, and a strong decrease in the I_{OFF}, for long times in the order of $\approx 10^4$ s.

The recovery trend curve has been obtained from the measurements and fitted, both for the variation in the I_{ds} in the OFF-region and the V_g for a fixed subthreshold I_{ds}, as a function of the recovery time.
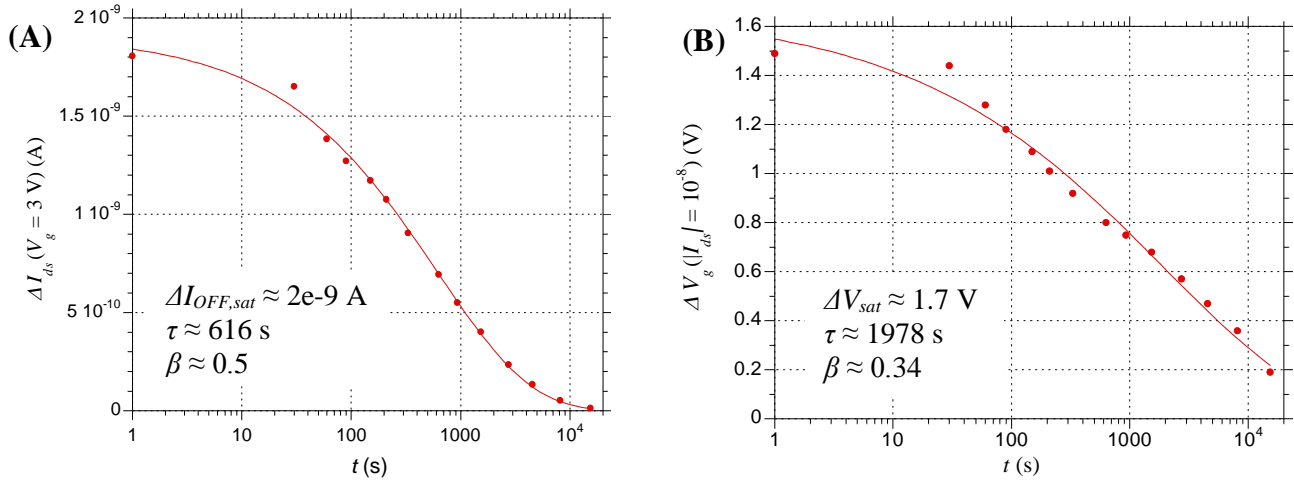
Fig. 28 Shifts of the I_{ds} in the OFF-region (A) and the V_g subthreshold (B) during the recovery. $L = 400$ µm, $W = 400$ µm.

The shift subthreshold is recovered in $\approx 2{\cdot}10^3$ s, one order magnitude higher than the value obtained during the light stress. Instead, the main recovery in the OFF-region is in a thousand of seconds, even if the complete recovery can be achieved only after $\approx 2{\cdot}10^4$ s. The recovery mechanism for the I_{OFF} is slow, justifying the low I_{ON}/I_{OFF} reported while measuring them after the exposure to light for needle probe adjustment on the electrodes.

2.2.2.4. Mechanical reliability

For these devices, considering that the substrate thickness is 100 µm, the strain ε_s results to be for the minimum bending radius 1%, for the maximum 2%. In Fig. 29 the resulting transfer and output curves are reported. The device considered is the same tested for the light stress, an $L = 400$ µm, $W = 400$ µm.
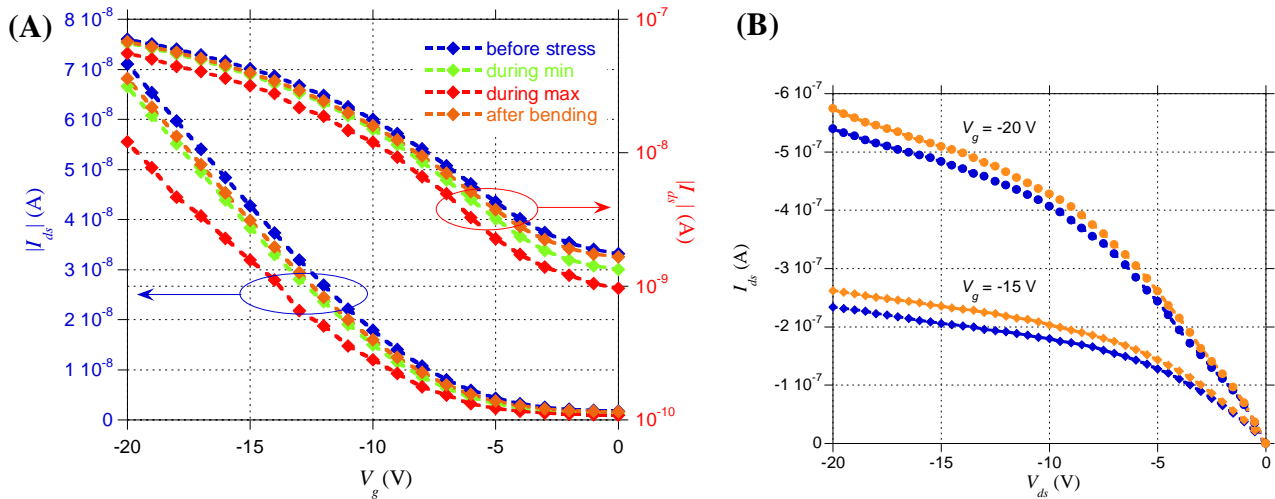
Fig. 29 The OTFT transfer (A) and output (B) curves under bending stress procedure. The colours legend is for both as in (A). L = 400 µm, W = 400 µm.

It has to be taken into account that these measurements are also affected by the light effects. The needles positioning on the electrodes has been conducted under light, the same intensity considered for the light stress measurements, while the positioning on the curved support has been carried on in dark, so this time interval is a recovery time for the device. To take into account these effects, a data analysis has been carried out as shown in Fig. 30.
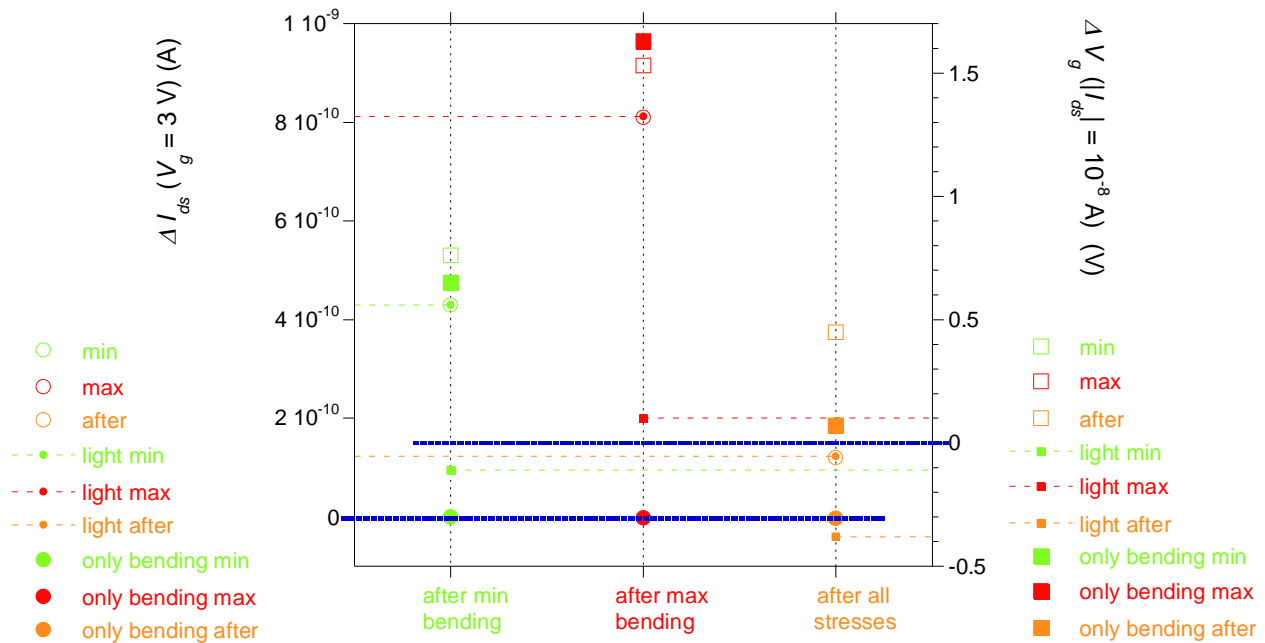
Fig. 30 Evaluation of the light influence on the bending measurements. In particular, the ΔI_{ds} in the OFF-region and the ΔV_g before the pinch-off are considered, dots on the left and squares on the right of the graph respectively. The values for the minimum bending are in green, for the maximum in red, for the after bending in orange. In blue the starting level. The dotted lines indicate the point at which the values are expected to be considering only the light exposure and recovery. L = 400 µm, W = 400 µm.

The time intervals considered for this approximation has been a fixed light exposure time of 1 min, which corresponds to the time to contact the electrodes with the needle probes, and a variable recovery time during the sample bonding/debonding on the curved surfaces. The latter has been considered for the minimum bending ≈ 210 s, for the maximum ≈ 630 s, for the measure after the test ≈ 60 s.
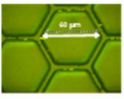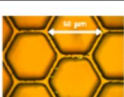
It has been highlighted that the light mainly influences the OFF-region of the characteristics, whose shift can be considered completely due to this effect (circles in Fig. 30). The variations in the characteristics at higher V_g, instead, can be also attributed to the bending (full squares in Fig. 30). As highlighted by the graph, the shift in V_g due to the only bending effect can be almost completely recovered after the stresses.

The device μ_{lin} decreases from 0.14 to 0.11 $cm^2V^{-1}s^{-1}$ at the highest strain, while it has not shown significant variations during the minimum bending and after the stress.

2.3. Organic source and drain

The organic conductor for the S/D contacts has been tested as it should provide a good charge injection even without the use of SAM functionalizations.[2,3]

2.3.1. Fabrication procedure

SCHEME	Step	Deposition technique	Material	Annealing	Thickness
S/D plate typical cell	Source/Drain	GRAVURE printing	PEDOT_A	120°C oven	≈ 70 nm
	Contact finishing	INKJET printing	Ag ANP DGP40 LT-15C	120°C oven	≈ 200 nm
OSC plate typical cell	OSC	GRAVURE printing	Merck SP400	100°C hot plate	≈ 50 nm
OGI plate typical cell	OGI	GRAVURE printing	Cytop_A	100°C oven	≈ 400 nm
	Gate	INKJET printing	Ag ANP DGP40 LT-15C	80°C oven	≈ 200 nm

Fig. 31 Scheme of the fabrication procedure of OTFTs with PEDOT:PSS gravure printed S/D contacts.

The fabrication process has been carried out at low temperature and without S/D contact functionalizations. Devices channel length, *L*, and width, *W*, ranged from 30 to 400 µm and from 100 to 500 µm, respectively. In Fig. 32 the device is shown, highlighting the OSC layer homogeneity and the distribution over the organic contacts.
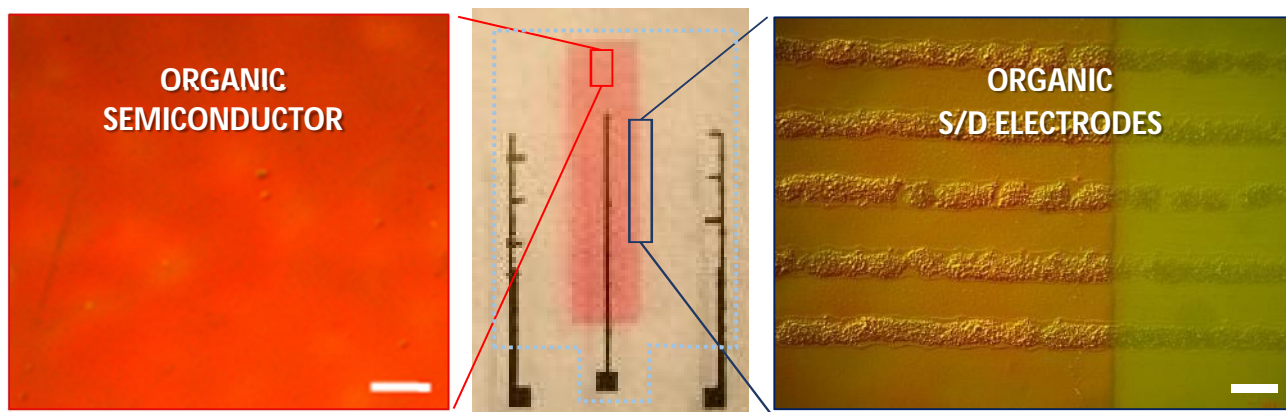
Fig. 32 Fully printed OTFT with organic S/D contacts: structure (centre) and optical microscopy magnifications of the OSC (left) and the contacts (right). Dotted light blue square indicates the dielectric. Scale bar 100 μm.

It can be observed that the OSC film shows a good morphology and it is highly homogeneous. Also, its distribution over the PEDOT:PSS contacts is uniform. The edges of the printed area are straight and well defined.

2.3.2. Electrical characterization

Representative transfer characteristics of the fully printed devices are shown in Fig. 33 for an OTFT with $L = 30$ μm, $W = 500$ μm, at $V_{ds} = -1$ V.
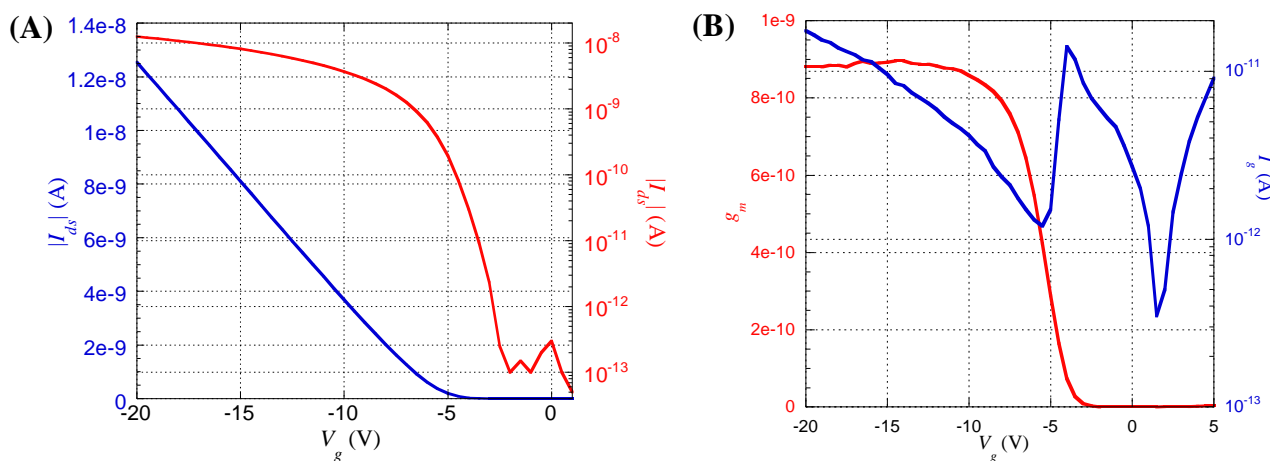
Fig. 33 (A) Representative transfer characteristics of a fully printed OTFT with organic S/D contacts, $V_{ds} = -1$ V. (B) Transconductance and leakage current. $L = 30$ μm, $W = 500$ μm.

The main electrical parameters of the transistors have been calculated from the transfer characteristics measured at low V_{ds}. The mobility μ_{LIN} is up to 0.06 cm^{2}V^{-1}s^{-1}, good linearity has been observed in the ON-region, even for shorter channel lengths, suggesting small parasitic contact resistance. The devices show low threshold voltage, ranging from -4 V to -8 V. Gate leakage current

is low, $I_{gs} < 20$ pA at $V_g = $ -20 V, due to the high quality of the printed dielectric layer. The subthreshold slope is low, down to 842 mV/dec, suggesting a good quality of the semiconductor/dielectric interface and low defect density in the semiconductor layer. The I_{ON}/I_{OFF} is quite high, around 10^5.
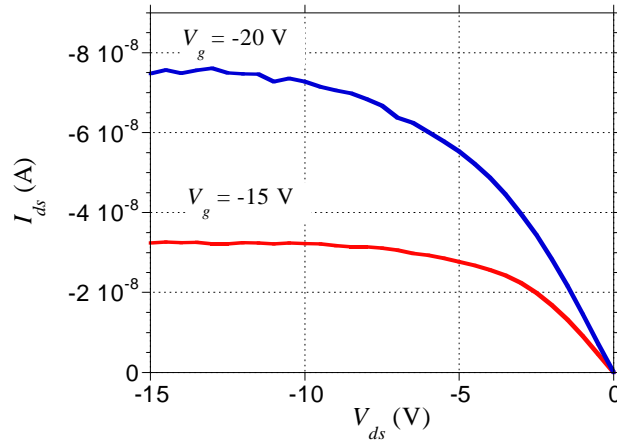

Fig. 34 Output curves of the fully printed OTFTs. L = 30 µm, W = 500 µm

Output characteristics (Fig. 34) show good linearity at low V_{ds} indicating a low parasitic contact resistance, as a consequence of a low energy barrier and a high carrier injection between the PEDOT:PSS contacts and the OSC.

At the best of the author knowledge, considering the current state of the art these devices are the best performing fully printed p-channel OTFTs with organic S/D realized with roll to roll techniques and are well comparable with the best ones obtained with inkjet printing techniques.[4–8]

2.3.2.1. Stability under bias stress

A device L = 30 µm, W = 500 µm has been tested under **bias stress**, $V_{g,stress}$ = -10 V and followed during the **recovery**. The transfer characteristics before and after the stress, after the recovery are reported in Fig. 35.
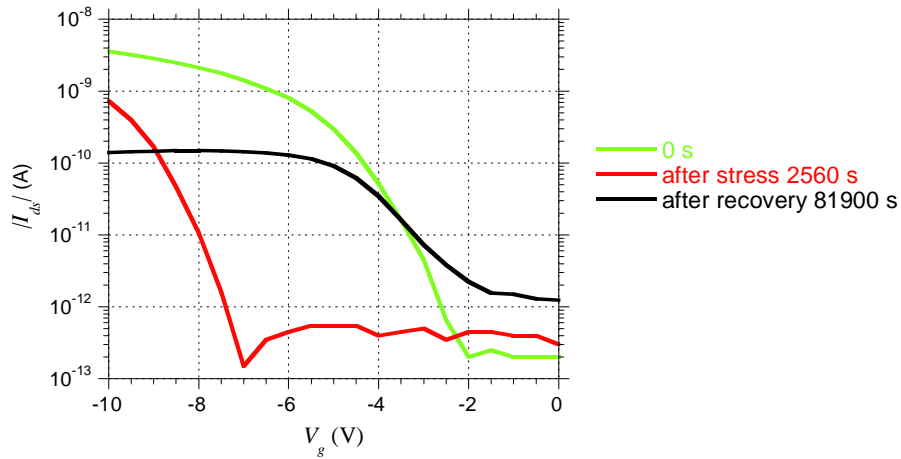
Fig. 35 Transfer characteristics of the OTFT under bias stress, after the stress, after the recovery. $V_{g,stress}$ = -10 V, V_{ds} = -1 V, L = 30 µm, W = 500 µm.

The device shows a strong instability under bias stress, which shifts the characteristics towards left and is not completely recovered after $\approx 10^5$ s. It is evident that these devices are not suitable for applications that require stability over long times, but more appropriate for disposable devices.

2.3.2.2. Sensitivity to light

The **recovery** of a device after light exposure (5 min, low light) is shown in Fig. 36.
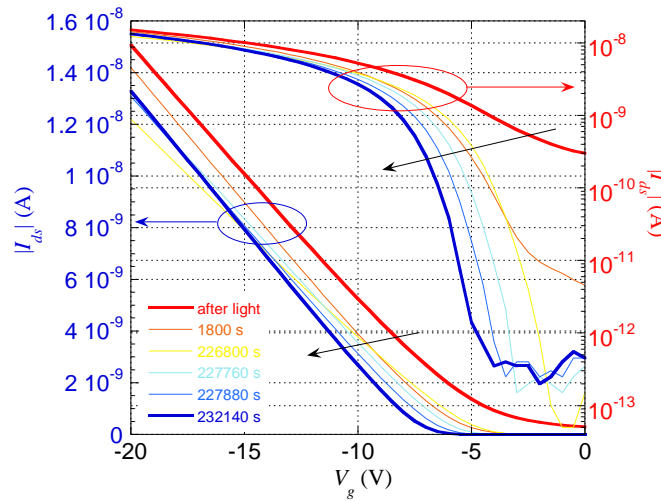
Fig. 36 Transfer characteristics during the recovery from light exposure. V_{ds} = -1 V, L = 30 µm, W = 500 µm.

The light exposure causes a shift of the characteristics towards right, around 3 V subthreshold, and an increase in the I_{OFF} value $\approx 10^3$. Hence, also for these devices, the I_{ON}/I_{OFF} is strongly affected by the light exposure. The μ_{lin} is almost constant, it slightly increases from 0.013 to 0.015 cm^{2}V^{-1}s^{-1} after $\approx 10^6$ s recovery.

3. N-type transistors

3.1. Fabrication procedure by solution techniques

The fabrication procedure has followed the scheme explained in Chapter 1, Paragraph 2.2.

As substrate has been chosen a heat-stabilized, low roughness, 100 μm thick polyethylene-naphthalate (PEN) foil, Teonex® Q65HA, by DuPont, as for the printed devices.

The semiconductor is the same used for the gravure printing, without any modification or filtering. A device and the OSC morphology when spin-coated on the Au are shown in Fig. 37.
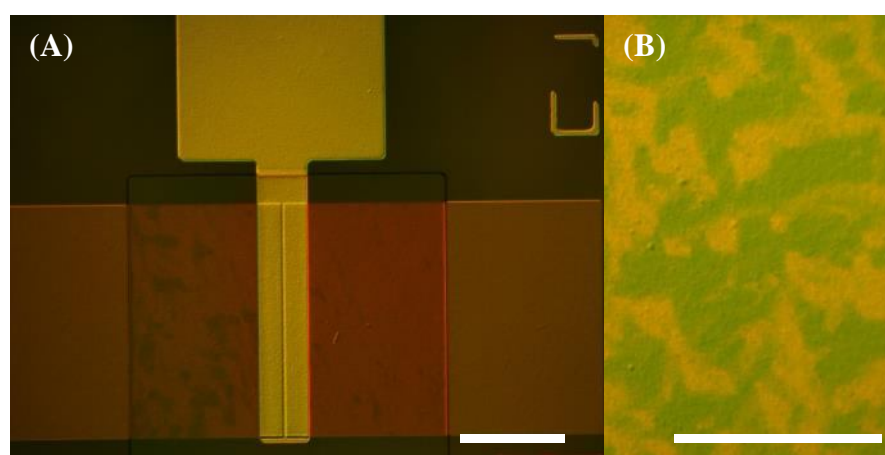

Fig. 37 (A) Optical microscopy picture of an n-type OTFTs fabricated by solution techniques. (B) Morphology of the spin-coated OSC over the gold S/D contacts. Scale bar 100 μm.

3.1.1. Electrical characterization

The transfer and output characteristics measured for these devices are reported in Fig. 38.
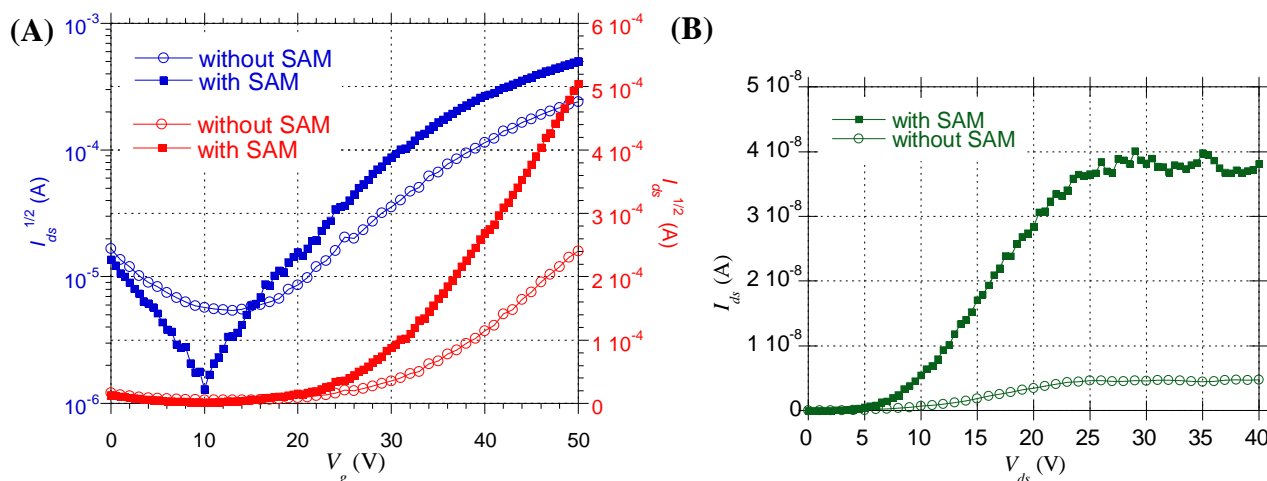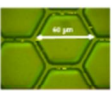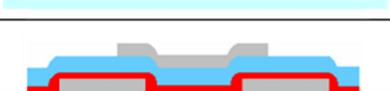
Fig. 38 (A) Representative transfer curves of the n-type OTFTs fabricated by solution techniques, V_{ds} = 50 or 40 V, for the device without or with the SAM, respectively. (B) Output characteristics of the same devices, V_g = 40 V. L = 100 μm, W = 245 μm.

The main electrical parameters of the transistors have been calculated from the transfer characteristics. Good linearity has been observed in the ON-region, the devices show an high threshold voltage, around 30 V, while gate leakage current is low, $I_{gs} \approx 30$ pA at V_g = 50 V and the I_{ON}/I_{OFF} is around 10^3.

The S/D contacts have been realized in Au, to avoid the oxidizing phenomena typical of the low φ metals. The OSC LUMO level and the metal φ do not correspond, generating a barrier to the charge carriers, as already discussed in the first Chapter. This effect is evident in the output characteristic at low V_{ds} (Fig. 38 B), which shows a strong non linearity. Hence, the S/D contacts have been functionalized with a strong electron acceptor SAM. The so treated devices still show high contact resistances, as evident again in their output characteristics. On the other hand, the mobility increases from around 0.04 up to 0.2 cm^{2}V^{-1}s^{-1} functionalising the S/D contacts, suggesting that an accurate optimization of the OSC interface with the S/D contacts could lead to improved performances.

These measurements are well comparable with the data reported in literature.[9] Hence, this OSC has been chosen due to its good performances.

3.2. Fabrication procedure by printing techniques

SCHEME	Step	Deposition technique	Material	Annealing	Thickness
	Source/Drain	INKJET printing	Ag ANP DGP40 LT-15C	100°C oven	≈ 160÷100 nm or ≈ 60 nm
OSC plate typical cell	OSC	GRAVURE printing	Polyera N2200	110°C vacuum oven overnight	≈ 50 nm
OGI plate typical cell	OGI	GRAVURE printing	Cytop_A	100°C oven	≈ 300÷800 nm
	Gate	INKJET printing	Ag ANP DGP40 LT-15C	80°C oven	≈ 200 nm

Fig. 39 Scheme of the fabrication procedure of n-type OTFTs.

The fabrication process has been carried out at low temperature and without the use of S/D contact functionalizations. Devices channel length, *L*, and width, *W*, ranged from 30 to 400 µm and from 100 to 900 µm, respectively.

The *S/D contacts* have been realised both thick and thin, as described in Chapter 4, Paragraph 2.3.1-2.3.2.

The devices realized with thinner contacts have not shown field effect. This condition could be due to the fact that the substrate surface is compromised after the RIE procedure. As shown in Chapter 4, Paragraph 2.3.2, the wettability of the PEN is increased 3 times after the RIE. Then, PEN hydrophobicity is not homogeneously recovered and just around 55%. Most likely the OSC cannot adjust correctly its morphology on such a hydrophilic surface, probably leading to the non-functioning OTFTs. Further substrate functionalizations to decrease its wettability have not been tested. Since the contact angle measurements performed have shown a lack of uniformity over the PEN, the surface has appeared to be not suitable for further treatments.

Different *dielectric* thicknesses, gravure printing methods and functionalizations have been tested. In particular, the following dielectric have been taken into account:

- 1 layer, 350 nm high;

- 4 layers, 400 nm high;

- 8 layers, 800 nm high.

The interface between the OSC and the dielectric either has been functionalized or not in HMDS, as explained in Chapter 2, Paragraph 2.2.4.

The dielectric deposited with a unique printing process has resulted in film inhomogeneities, visible at the optical microscope (Fig. 40). In particular, it has thinned significantly over the contact edges, down to less than 100 nm.
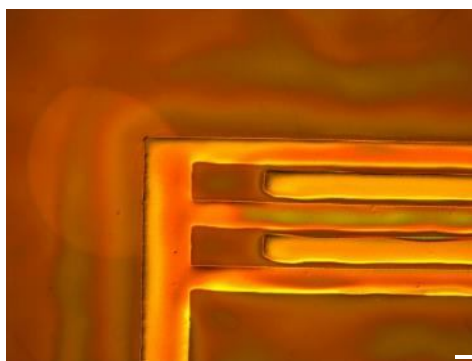

Fig. 40 Dielectric inhomogeneities when printed as a unique layer.

This effect has reduced the dielectric breakdown voltage around some volts, widely lower than the expected value of 35 V. The use of multi-layers has resulted in a uniform morphology over the edges. Four layers, each $\approx$ 100 nm, have resulted as the minimum to avoid leakage currents, while too much layers have damaged the underlying OSC.

The interface between the OSC and the dielectric has been significantly improved by the HMDS functionalization, as previously reported in literature for SiO_2 dielectric.[10,11] Also for the organic materials, it can be assumed that the hydroxylic groups at the OSC/dielectric interface act as irreversible trapping states for the electrons. The HMDS passivates some of these groups, operating as a tunnelling barrier for the electrons.

The most performing devices have been obtained using the thick S/D contacts, a dielectric deposition method composed of four subsequent gravure printed layers, each $\approx$ 100 nm thick, and the OSC/dielectric interface functionalised with HMDS. In Fig. 41 a device is shown, with an optical microscopy magnification of its morphology.
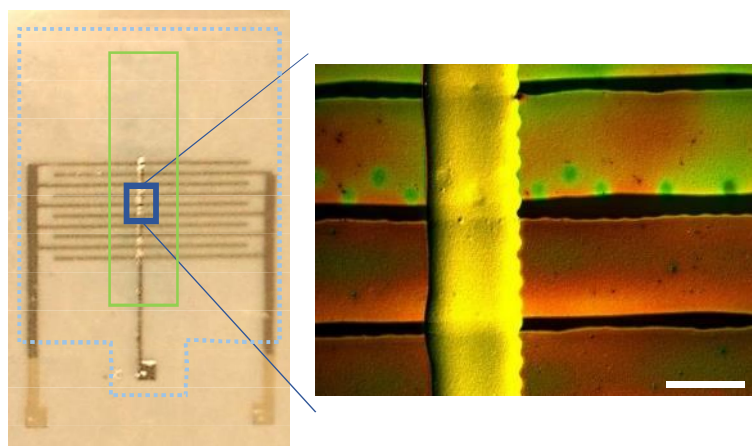
Fig. 41 Fully printed n-type OTFT structure (left) and optical microscopy magnification of its morphology (right). Dotted light blue square indicates the dielectric, in green the OSC. Scale bar 100 μm.

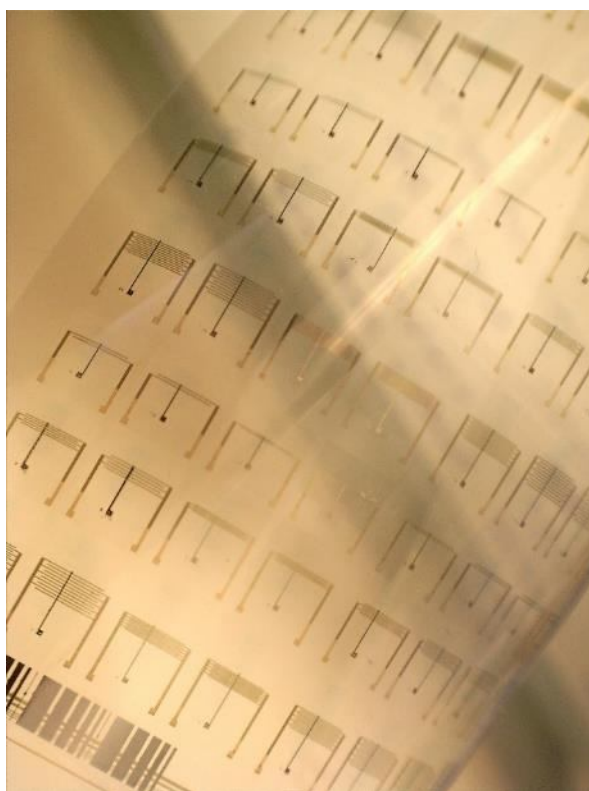In the following image a picture of a full sample (Fig. 42).

Fig. 42 Sample of fully printed n-type OTFTs. At the bottom of the sample the MIM devices to verify the dielectric performances.

3.2.1. Electrical characterization

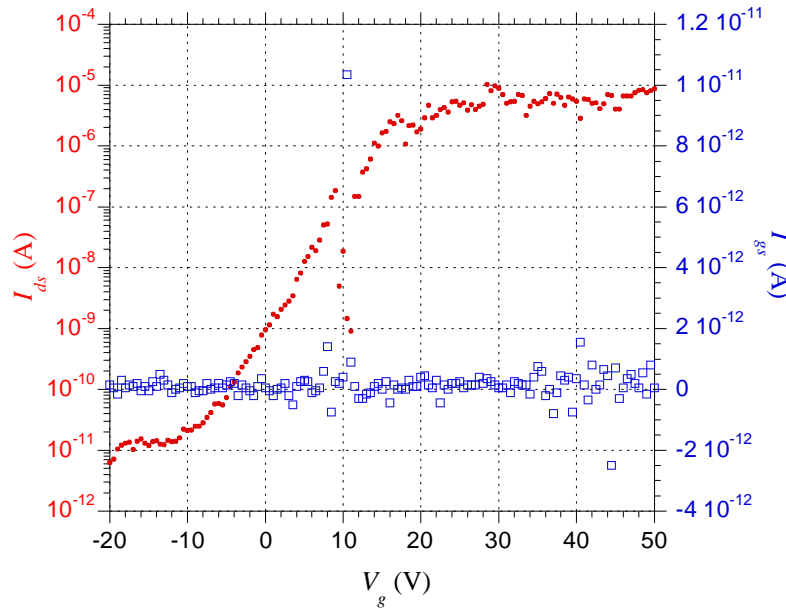Representative transfer characteristic of the n-type OTFT is shown in Fig. 43, for an $L = 100$ μm, $W = 400$ μm, $V_{ds} = 10$ V.

Fig. 43 Transfer characteristic and leakage current of a fully printed n-type OTFT with L = 100 µm, W = 400 µm OTFT, V_{ds} = 10 V.

While calculating the main electrical parameters of the transistors from the transfer characteristics, it has to be taken into account that these values are qualitative for these devices, as they are affected by errors due to the instability of the measurements. The device shows a strong field effect even at lower V_{ds} compared to the devices fabricated by solution techniques. The threshold voltage is $\approx$ 13 V, the subthreshold slope $\approx$ 4600 mV/dec, while the I_{ON}/I_{OFF} is very high, around 10^6. Gate leakage current is very low, I_{gs} < 3 pA, with a peak of $\approx$ 10 pA around V_g = 10.5 V, which causes an instability in the I_{ds}. These data show that these n-type devices are very sensitive to I_{gs} increase.

The devices have shown a strong instability at bias stress, not allowing a more complete characterization in bias and light.

The device characteristics are promising, but their stability and reproducibility among different devices have not been yet reached. The main issue can be identified in the optimization of the interface between OSC and dielectric.

References

(1)   Kang, H.; Kitsomboonloha, R.; Jang, J.; Subramanian, V. High-Performance Printed Transistors Realized Using Femtoliter Gravure-Printed Sub-10 Mm Metallic Nanoparticle Patterns and Highly Uniform Polymer Dielectric and Semiconductor Layers. *Adv. Mater.* **2012**, *24* (22), 3065–3069.

(2)   Prakash, S.; Karacor, M. B.; Banerjee, S. Surface Modification in Microsystems and Nanosystems. *Surf. Sci. Rep.* **2009**, *64* (7), 233–254.

(3)   Boudinet, D.; Benwadih, M.; Qi, Y.; Altazin, S.; Verilhac, J.-M.; Kroger, M.; Serbutoviez, C.; Gwoziecki, R.; Coppard, R.; Le Blevennec, G.; Kahn, A.; Horowitz, G. Modification of Gold Source and Drain Electrodes by Self-Assembled Monolayer in Staggered N- and P-Channel Organic Thin Film Transistors. *Org. Electron.* **2010**, *11* (2), 227–237.

(4)   Huebler, A. C.; Doetz, F.; Kempa, H.; Katz, H. E.; Bartzsch, M.; Brandt, N.; Hennig, I.; Fuegmann, U.; Vaidyanathan, S.; Granstrom, J.; Liu, S.; Sydorenko, A.; Zillger, T.; Schmidt, G.; Preissler, K.; Reichmanis, E.; Eckerle, P.; Richter, F.; Fischer, T.; Hahn, U. Ring Oscillator Fabricated Completely by Means of Mass-Printing Technologies. *Org. Electron.* **2007**, *8* (5), 480–486.

(5)   Kempa, H.; Hambsch, M.; Reuter, K.; Stanel, M.; Schmidt, G. C.; Meier, B.; Hubler, A. C. Complementary Ring Oscillator Exclusively Prepared by Means of Gravure and Flexographic Printing. *IEEE Trans. Electron Devices* **2011**, *58* (8), 2765–2769.

(6)   Barret, M.; Sanaur, S.; Collot, P. Inkjet-Printed Low-Voltage Organic Thin-Film Transistors: Towards Low-Cost Flexible Electronics. In *Mater. Res. Soc. Symp. Proc. 1003*; 2007.

(7)   Søndergaard, R. R.; Hösel, M.; Krebs, F. C. Roll-to-Roll Fabrication of Large Area Functional Organic Materials. *J. Polym. Sci. Part B Polym. Phys.* **2013**, *51* (1), 16–34.

(8)   Mandal, S.; Dell'Erba, G.; Luzio, A.; Bucella, S. G.; Perinot, A.; Calloni, A.; Berti, G.; Bussetti, G.; Duò, L.; Facchetti, A.; Noh, Y.-Y.; Caironi, M. Fully-Printed, All-Polymer, Bendable and Highly Transparent Complementary Logic Circuits. *Org. Electron.* **2015**, *20*, 132–141.

(9)   Yan, H.; Chen, Z.; Zheng, Y.; Newman, C.; Quinn, J. R.; Dötz, F.; Kastler, M.; Facchetti, A. A High-Mobility Electron-Transporting Polymer for Printed Transistors. *Nature* **2009**, *457* (7230), 679–686.

(10)   Yoo, B.; Jung, T.; Basu, D.; Dodabalapur, A.; Jones, B. A.; Facchetti, A.; Wasielewski, M. R.; Marks, T. J. High-Mobility Bottom-Contact N-Channel Organic Transistors and Their Use in Complementary Ring Oscillators. *Appl. Phys. Lett.* **2006**, *88* (8), 082104.

(11)   Zaumseil, J.; Sirringhaus, H. Electron and Ambipolar Transport in Organic Field-Effect Transistors. *Chem. Rev.* **2007**, *107* (4), 1296–1323.

Chapter 6
Fully printed p-mos inverters

1. Introduction

Considering any integrated circuit technology used in digital circuit design, the basic circuit element is the logic inverter. The operation mode and the characteristics of this element has to be thoroughly understood in order to design more complex circuits.

Digitally encoded information are represented using two logic levels, a Logic 0 and a Logic 1. Logic operations are performed using logic gates, the simplest operation is the inversion, as defined in the following truth table:

IN	OUT
1	0
0	1

The **static** working mode of an inverter can be described by the *transfer characteristic*, which defines the output voltage, V_{OUT}, as a function of the input voltage, V_{IN}, as schematized in Fig. 1.
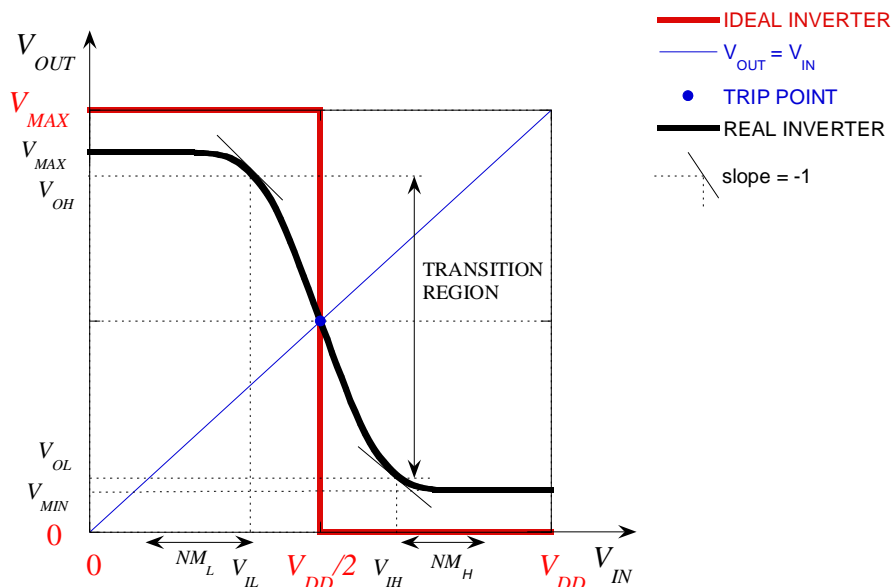

Fig. 1 Transfer characteristic of the inverter. In the scheme are reported the maximum and the minimum output voltage, V_{MAX} and V_{MIN}, the high and low output voltage, V_{OH} and V_{OL}, the high and low input voltage, V_{IH} and V_{IL}, the supply voltage V_{DD}, the noise margin high and low, NM_H and NM_L.

In a real inverter, the logic levels are defined by the values comprised in the following ranges:

- Logic 0: $V_{MIN} \div V_{OL}$

where V_{MIN} is the V_{OUT} when $V_{IN} = V_{DD}$, V_{OL} is the smallest V_{OUT} where slope = -1

- Logic 1: $V_{OH} \div V_{MAX}$

where V_{OH} is the largest V_{OUT} where slope = -1, V_{MAX} is the V_{OUT} when $V_{IN} = 0$

Considering that the voltage signals are always contaminated by noise, it is critical for a logic gate to define its immunity to the noise. The most important figure of merit to evaluate this condition is the noise margin, NM, defined as the maximum allowable spurious signal that can be accepted by a device when used in a system while still giving correct operation.[1]

For an inverter, the values of V_{IN} that produce a valid logic value are defined by the ranges:

- $V_{IH} \div V_{DD}$ → Logic 0

where V_{IH} is the minimum V_{IN} which produces a $V_{OUT} = V_{MIN}$;

- $0 \div V_{IL}$ → Logic 1

where V_{IL} is the maximum V_{IN} which produces a $V_{OUT} = V_{MAX}$.

The V_{IL} and V_{IH} values can be calculated as the V_{IN} values where the transfer curve has a slope = -1. They define the areas in which the inverter *gain A_V* is lower or higher than 1. The A_V value is defined in Eq. 1:

$$A_V = \frac{\Delta V_{OUT}}{\Delta V_{IN}} = \frac{V_{OH} - V_{OL}}{V_{IH} - V_{IL}} > 1 \qquad \textbf{Eq. 1}$$

where ΔV_{OUT} is the input logic swing, ΔV_{IN} is the input logic swing. The logic swing is defined as the lowest. The noise is attenuated when V_{IN} is lower than V_{IL} or higher than V_{IH}, so still producing the correct logic level, while is amplified when $V_{IL} < V_{IN} < V_{IH}$. The gain can be practically measured as the maximum of the derivative of the transfer characteristic.

Hence, to quantify the noise immunity of an inverter, *noise margins* of the low, NM_L, and high, NM_H, level can be defined as in the following equations:

$$NM_H = V_{OH} - V_{IH} \qquad \textbf{Eq. 2}$$
$$NM_L = V_{IL} - V_{OL} \qquad \textbf{Eq. 3}$$

They have to be as higher as possible, but at least ≥ 1 to ensure the inverter *regenerative property*, the ability to repair a noisy signal in a chain of logic gates. The noise margin of the inverter is considered to be as the lowest between these two values.[1]

Considering the **dynamic** response of an inverter, usually a square signal is given as V_{IN} and the oscillating V_{OUT} waveform is recorded as a function of time.

As the device is not ideal, it requires some time to switch at the correct logic level. Two significant time intervals are hence used to describe the inverter characteristics, defined as follows and schematized in Fig. 2:

- *rise time*, t_r: time required for the transition from the 10% to the 90% of the V_{OUT}.

- *fall time*, t_f: time required for the transition from the 90% to the 10% of the V_{OUT}.
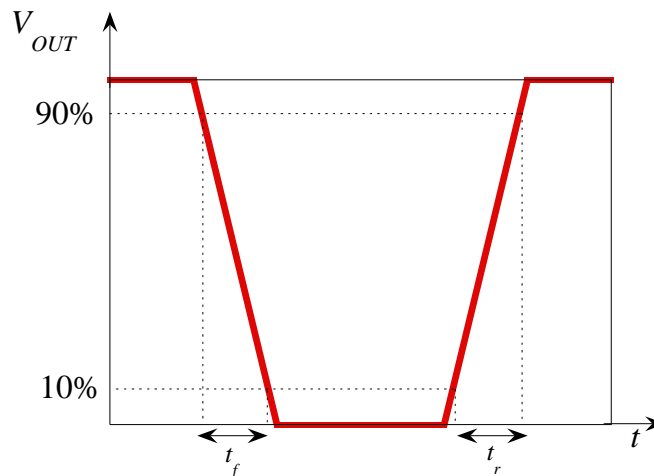

Fig. 2 Schematized dynamic response of an inverter.

An inverter is composed of a drive and a load. Two different configuration of inverter has been taken into account during this thesis work, using as load either a resistor or a transistor (Fig. 3 A-B).
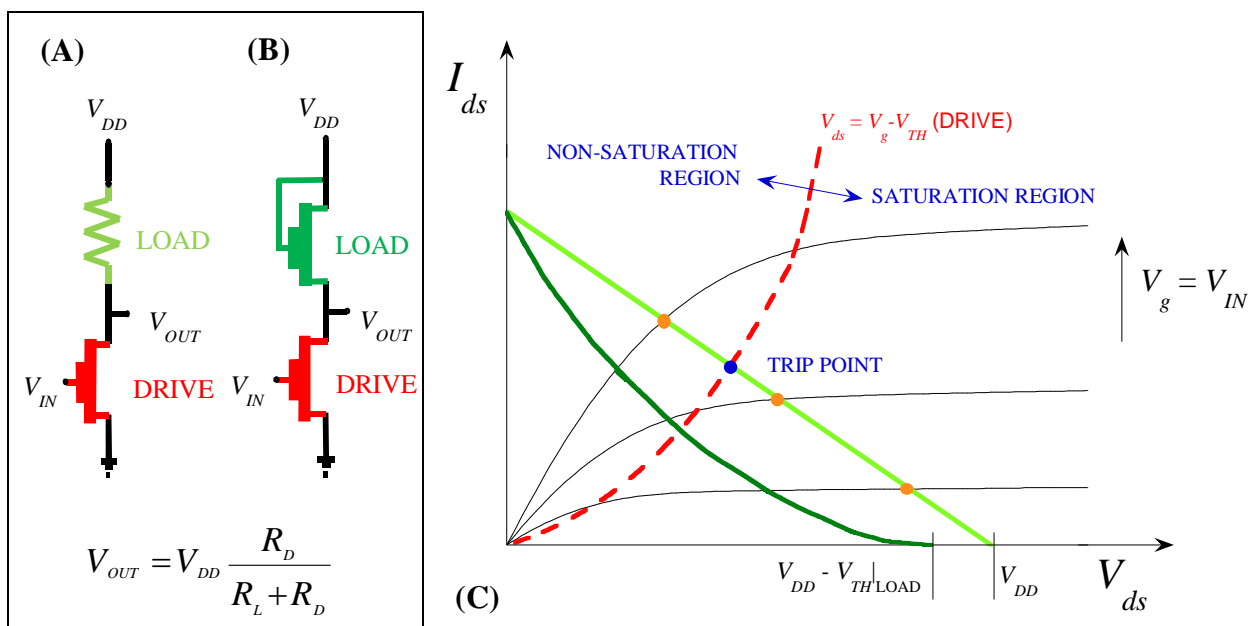
Fig. 3 Scheme of the two main inverter configuration considered for this thesis work: with resistive load (A) or active load (B). In the equation it is expressed the partition of the V_{DD} between the two components. R_D drive resistance, R_L load resistance. (C) Working mode of the two inverters: in green the load lines of the load, in black the drive output curves.

Considering the **resistor** load (Fig. 3 A) and an ideal transistor, when $V_{IN} < V_{TH}$ the transistor is in the OFF-state, ideally an infinite resistance. So, all the V_{DD} is on the resistor, the $V_{OUT} = V_{DD}$, the Logic 1. While increasing the V_{IN}, the working point of the transistor moves up on the load curve, its resistance lowers towards zero. The V_{OUT} is partitioned between the transistor and the resistor, down to V_{DD}/R_L, the Logic 0. Hence, the resistor pull the V_{OUT} up towards the V_{DD}, while the transistor drive pull down the V_{OUT} towards the V_{OL}. The slope of the transition region and the Logic 0 increase as the R_L is increased. Since resistors usually require large areas on the chip, they are not widely used in integrated circuits design. The printed resistors developed during this thesis work, Chapter 4, Paragraph 4, require an area around 1 mm^2, thus they are promising for a future integration in a fully printed inverter.

Instead of a resistor, a transistor with the gate connected to the drain can be used as load (Fig. 3 B). The device operates in saturation, as the $V_g = V_{DD}$, acting as a non-linear resistor. In this configuration, when $V_{IN} = V_{DD}$, the V_g of both transistors are equal to V_{DD}. If the driver transistor has to be able to pull the V_{OUT} down, R_L must be higher than R_D, so usually $(W/L)_{drive} < 10\ (W/L)_{load}$. When the V_{IN} is lowered, the load transistor will easily pull the V_{OUT} down against the driver, which is almost in the OFF-state.[2] Since the load transistor stops conducting when its $V_g = V_{ds} = V_{DD}$ decreases to V_{TH}, for this inverter configuration $V_{OH} = V_{DD} - V_{TH/LOAD}$. This configuration should yield to a smaller logic swing compared to the resistive load inverter.[3]

2. Resistive load configuration

2.1. Fabrication procedure and measurement setup

The fully printed OTFT with silver S/D electrodes, as detailed in Chapter 5, Paragrah 2.2, have been used as driver transistors. To obtain the inverters an external resistance has been linked using the needle probes.

The measurement setup has been the following:

- a pulse generator to supply the V_{IN}, connected to an amplifier, based on an LF412C in inverting configuration, has allowed to reach 30 V;
- a resistor of 30 MΩ has been connected to the OTFT drain electrode;
- a buffer has been used to decouple the signal impedance and the oscilloscope, again an inverting amplificatory based on an LF412C;
- two power supply have been used for the V_{DD} and the amplification stages supply.

The V_{DD} applied to the OTFT source ranges between $+V_{DD} \div 0$, so that the V_g of the drive ranges between $0 \div -V_{DD}$. The V_{OUT} of the inverter would be then positive.

2.2. Dynamic characteristics

In Fig. 4 some measurements of the dynamic characterization of the inverters with resistive load are shown, for different driver transistor channel length, $L = 30 - 100 - 400$ μm, and width $W = 400$ μm.
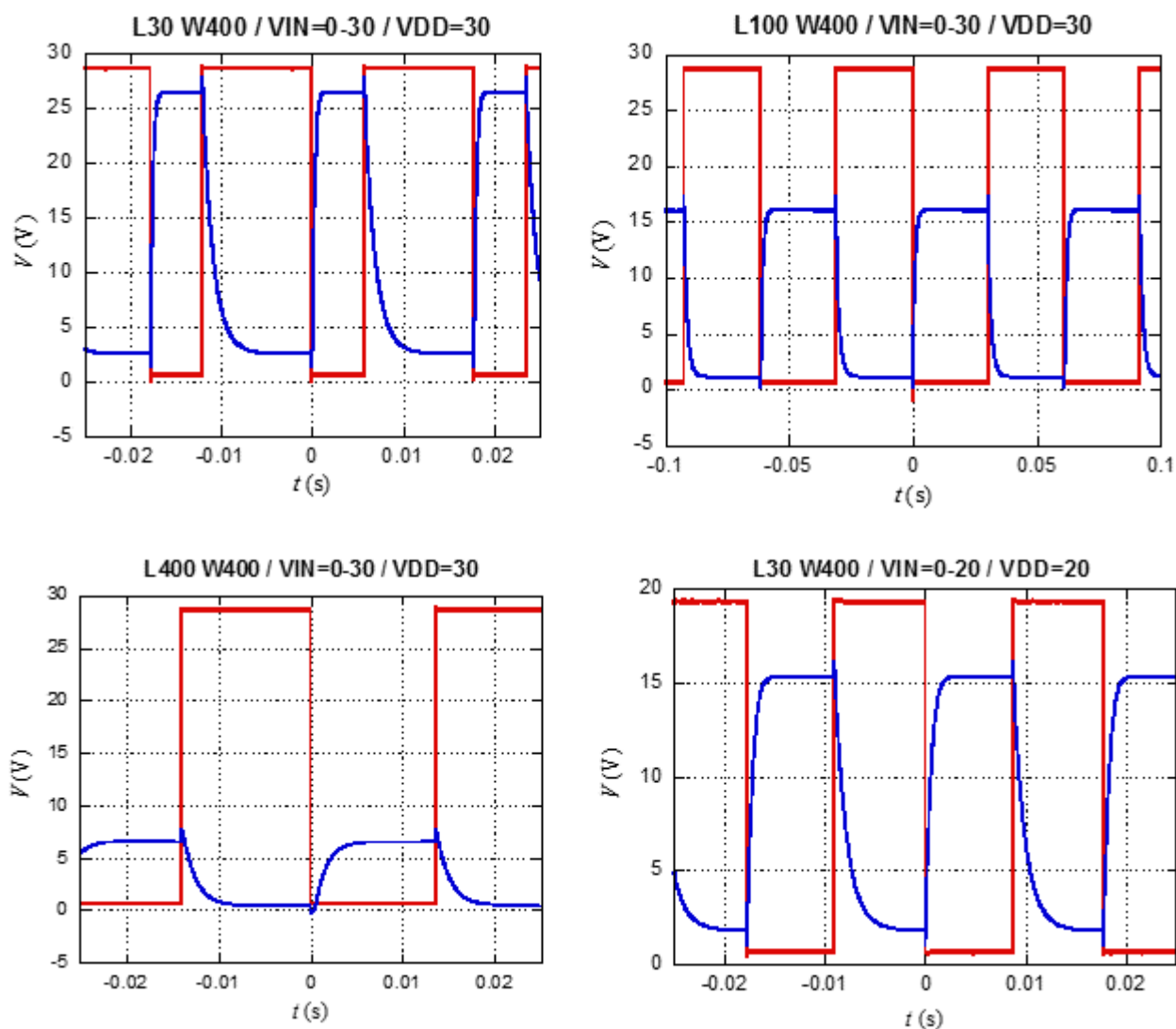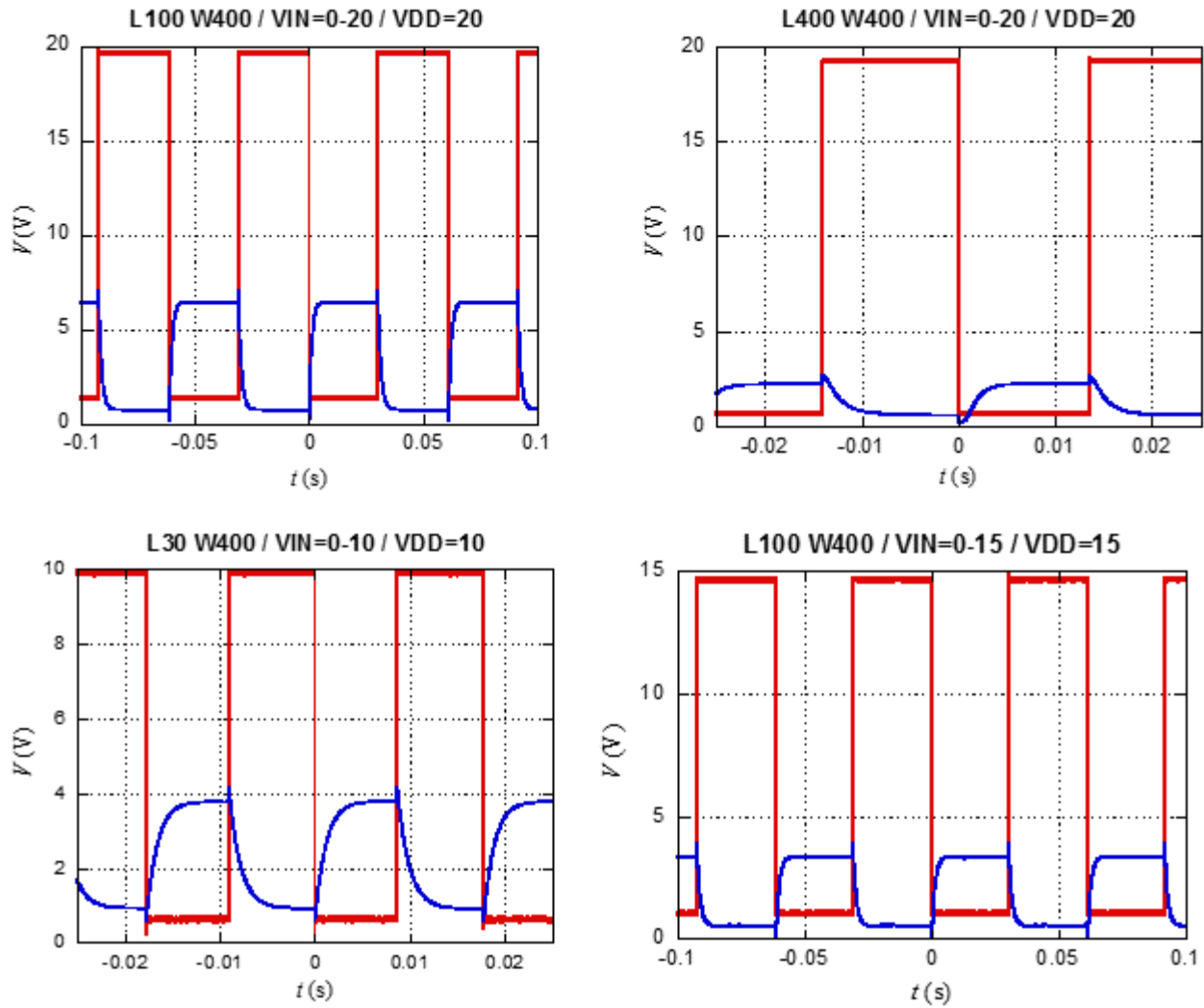
Fig. 4 Dynamic characterization of inverters, resistive load R_L = 10 MΩ, with different *W/L* and applied voltages. The red signal is the input, the blue the output. Channel length and width (L = *L*, W = *W*) are expressed in micrometers, while voltages are in Volts (VIN = V_{IN}, VDD = V_{DD}).

The maximum frequency that has been tested, still achieving a good output waveform, has been 1 kHz, for the device with L = 30 μm, W = 400 μm, V_{DD} = 10 V.

Increasing the L of the drive transistor, its resistance increases, so reducing the V_{MAX} achievable by the device. Moreover, the device becomes increasingly slow, as shown by the t_r and t_f values calculated from these curves (Fig. 5).
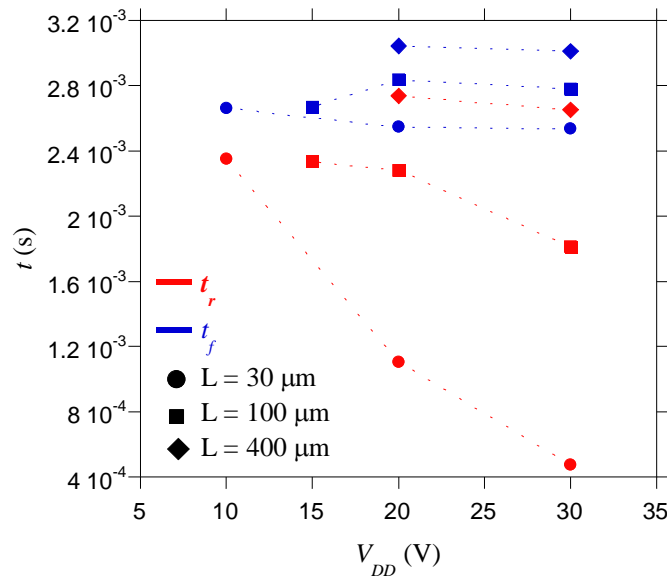
Fig. 5 Rise and fall time for the resistive load inverters as a function of the V_{DD}.

For a given L, the fall time is always higher than the rise time, limiting the operating frequency. This effect could be attributed to the load transistor, more resistive than the drive.

3. Active load configuration

3.1. Fabrication procedure and measurement setup

The fully printed OTFT with silver S/D electrodes, as detailed in Chapter 5, Paragraph 2.2, have been used for both transistors. The fully printed inverters have been realized in the active load configuration by properly linking two OTFTs with the inkjetted silver. The inkjet printing procedure has been the same described for gate deposition in Chapter 3, Paragraph 2.2.

The measurements have been carried out by using two Keithley K236 Source Measure Units, to generate the V_{IN} and the V_{DD}, and a multimeter Kethley K2440, to measure the V_{OUT}.

For the dynamic characterization, it has been used an amplifier based on the THS4631.
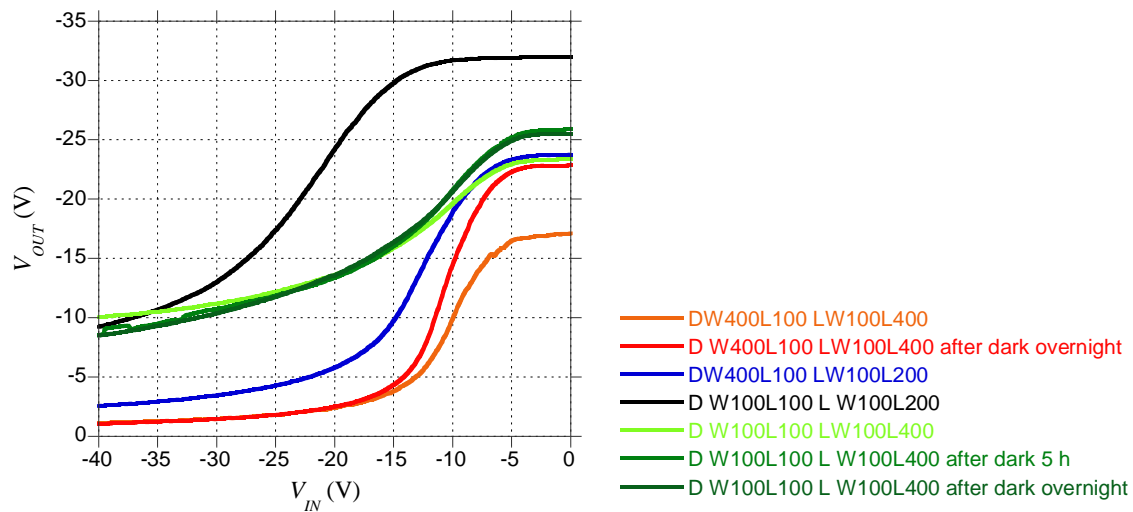
3.2. Static characteristics

Fig. 6 Several transfer characteristics of active load inverters, with different load (L) and drive (D) coupling. The influence of light exposure is shown for two devices. V_{DD} = -40 V.

After the preliminary measurements, some of which reported in Fig. 6, the most promising device has been chosen coupling as load an $W = 100$ µm, $L = 400$ µm, as drive an $L = 100$ µm, $W = 300$ µm.
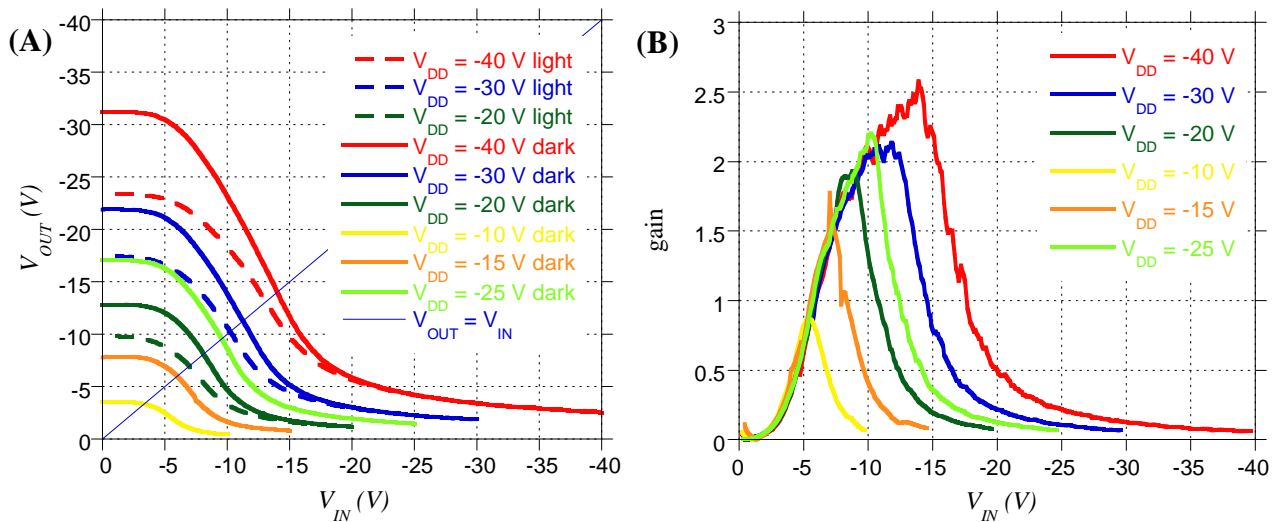
Fig. 7 (A) Transfer characteristics of the inverter with active load at different V_{DD}, effect of the light exposure. (B) Gain of the inverter as function of the input, characteristics in dark. Drive: $W = 300$ µm, $L = 100$ µm; Load $W=100$ µm, $L = 400$ µm.

At first, the Logic 0 level that has been measured was found to be high, due to the high drive I_{OFF}, which decreases the R_D, preventing the load to pull up the V_{OUT}. Since the light effect has to be considered for these devices, as explained in Chapter 5, Paragraph 2.2.2.3, the measurements have

been repeated after recovery in dark. As shown in Fig. 7 A this measurement procedure has allowed to obtain high V_{OUT} voltages for $V_{IN} = 0$ V.

The inverter gain has been calculated as the derivative of the transfer characteristics. Decreasing the supply voltage the signal swing is decreased, so the device would be less sensitive to crosstalk internal of the system, while more sensitive to the external noise. The highest gain achieved has been ≈ 2.6. The trip voltage (indicated as the peak of the gain shown in Fig. 7 B) approaches $V_{DD}/2$ for decreasing V_{DD}. The main parameters are summed up in Tab. 1.

	$V_{DD} = $ -10 V	$V_{DD} = $ -15 V	$V_{DD} = $ -20 V	$V_{DD} = $ -25 V	$V_{DD} = $ -30 V	$V_{DD} = $ -40 V
NM_H	-	2.7	1.89	1.1	0.45	-1.52
NM_L	-	-1.8	0.7	3.3	5.7	12
A_V	-	1.3	1.5	1.7	1.7	1.9
gain	0.9	1.5	1.9	2.2	2.1	2.6
trip voltage	5.4	7	8.8	10.2	11.2	13.9

Tab. 1 Fully printed inverter main parameters. Drive: $W = 300$ μm, $L = 100$ μm; Load $W=100$ μm, $L = 400$ μm.

As shown in Tab. 1, the best performance has been obtained applying a $V_{DD} = $ -25 V. For this polarization, the noise margins are both positive and higher than one, ensuring the regenerative property of the device.

3.3. Dynamic characteristics

In Fig. 8 the output waveform for a square input are reported for the inverter previously characterized in static.

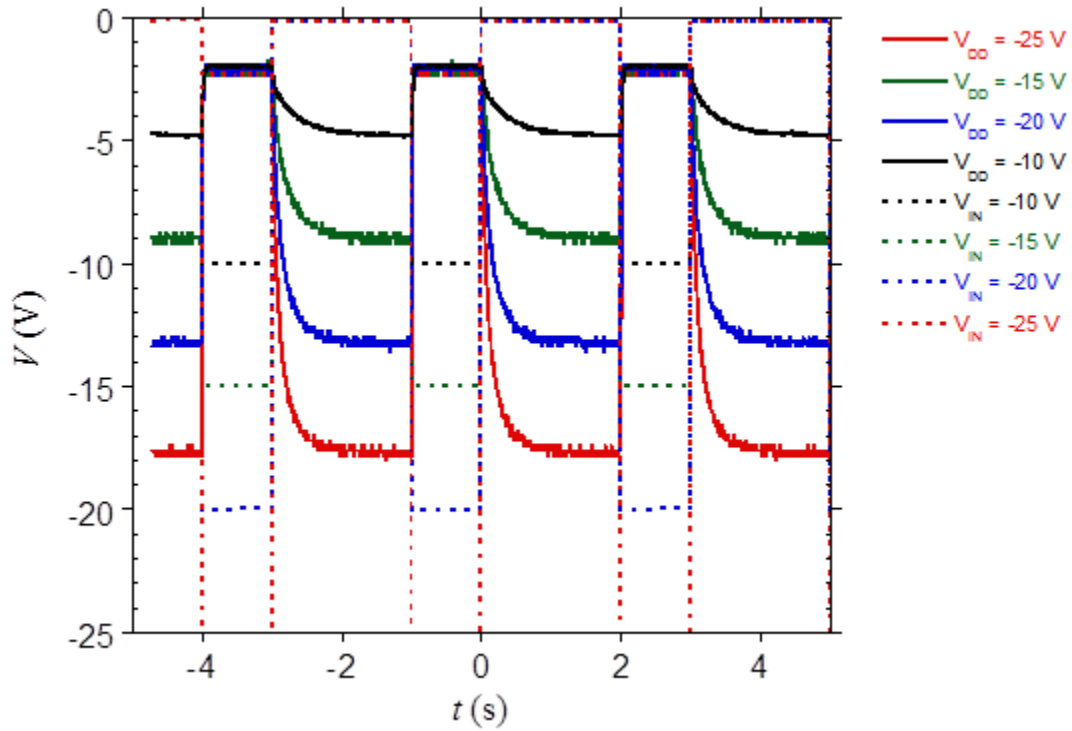**Fig. 8 Dynamic characteristics of the inverter at different V_{DD}. Drive: $W = 300$ μm, $L = 100$ μm; Load $W = 100$ μm, $L = 400$ μm.**

The t_r and t_f values calculated from these curves are reported in Fig. 9.
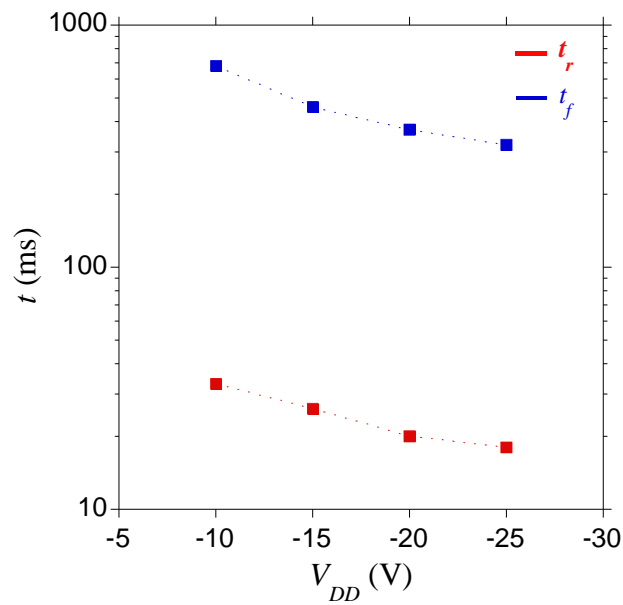

Fig. 9 Rise and fall time for the active load inverters as a function of the V_{DD}.

Both characteristic times are affected by OTFT parasitic capacitance. Fall time is higher than rise time also for this configuration.

An improvement of the inverter characteristics can be obtained by the optimization of the OTFT layout, in order to reduce the parasitic capacitance, and by a more suitable coupling of the drive and load, through the OTFTs channel length and width variation.

References

(1)   De Vusser, S.; Genoe, J.; Heremans, P. Influence of Transistor Parameters on the Noise Margin of Organic Digital Circuits. *IEEE Trans. Electron Devices* **2006**, *53* (4), 601–610.

(2)   Klauk, H. *Organic Electronics, Materials, Manufacturing and Applications*; WILEY-VCH Verlag GmbH & Co. KGaA, Weinheim, 2006.

(3)   Whitaker, J. C. *The Electronics Handbook*, 2nd ed.; The Electrical Engineering Handbook Series; Taylor & Francis Group, 2005.

Conclusions

During this thesis work resistors, MIMs, OTFTs and inverters have been realized with printing techniques and characterized, optimizing the gravure and inkjet printing processes and refining several high performance electronic organic inks.

At first, the gravure printing process has been studied to overcome some of the current issues of the technique. The **gravure printing system** has been modified and improved, in particular through the realization of a suitable *glass cliché* (Fig. 1).
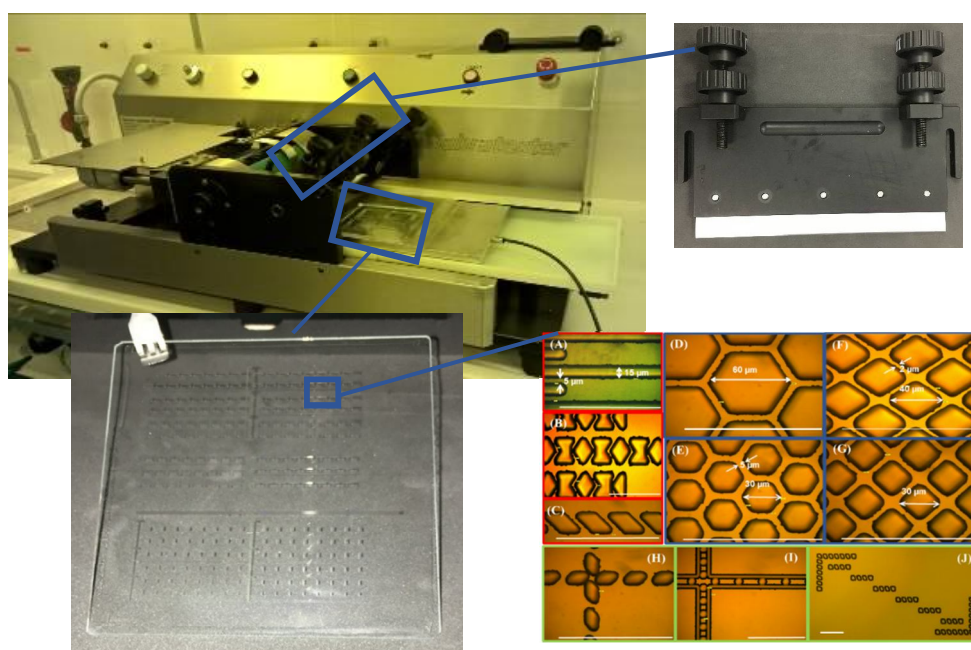

Fig. 1 Modified gravure printer with the optimized glass cliché.

The procedure to define the cells on the cliché has been optimized, allowing to achieve the following technical features:

- etch control down to 0.5 μm;
- lateral etch compensation;
- homogeneous etch over the cliché area;
- resolutions down to 2 μm;
- cell edge structure improved;
- bottom cell roughness down to 10 nm;
- control of surface wettability by optimized functionalization.

Moreover, the developed glass cliché has allowed to overcome the limit of standard silicon and metal cliché, in particular the limited dimensions and the possible metallic particles contamination.

Secondly, **high performance electronic ink** formulations have been assessed with this system, in particular an *organic dielectric* and an *organic conductive* formulation.

It has been evaluated the influence of the forces acting on the fluid during the printing process through the analysis of several significant *fluid dynamic parameters*. It has been defined a range of parameters suitable to obtain acceptable printing outcomes with the optimized printing system.

The *rheological analyses* have allowed to identify the presence of intrinsic instabilities in the ink formulations, such as thixotropic loops, which make the inks hardly manageable. The elastic behaviour of the inks has been studied through the variations of the *G'* and *G''* moduli, resulting in significant differences in the ink transferring on the substrate as a function of the cell geometry. Formulations with low yield point have shown an enhancing in the levelling step resulting in an improvement of the final film homogeneity and ensuring a good interface between the OSC and the dielectric in the OTFTs. It has been pointed out the possibility to use a Newtonian-like ink to achieve a highly uniform film over large areas, while it has been taken advantage of a pseudoplastic behaviour for highly scaled features.

The gravure printing process of two *polymeric OSCs*, a *p-type* and an *n-type*, has been optimized, by changing printing parameters, in order to get continuity and homogeneity of the layer.

The **inkjet printing technique** has been applied to electrode realization, in particular for OTFTs and MIM applications, and resistors definition.

Concerning the inkjet printing of *silver*, different procedures have been optimized depending on the application requirements. This process has allowed to achieve the following results:
- high resolution applications: arrays of printed areas down to 200x100µm;
- top contacts: low temperature process, down to 80°C, without damages to the dielectric layer, as confirmed by the electrical measurements;
- S/D contacts: two different layer thicknesses, reduction of the coffee ring effect and roughness, low resistivity.

Resistors have been realized using a carbon ink, achieving resistances from 0.2 MΩ up to 17 MΩ in an area of 1 mm^2. The devices have demonstrated to be suitable for future applications in mechanical sensors or as load for inverters.

Then, **p-type and n-type OTFTs** have been realised and electrically characterized, testing their stability under bias, light and bending stresses (Fig. 2).

The *p-type OTFTs with gold S/D contacts patterned by laser lithography* have shown a strong influence of the contact resistance and a not perfect dielectric layer. The field effect mobility μ_{LIN} has been measured up to 0.22 cm^{2}V^{-1}s^{-1}. They have shown instabilities under bias stress both in the ON- and OFF-regions, with a complete, but slow, recovery in the ON-region after bias removing. On the contrary, the instabilities induced by light exposure have been recovered quite fast, in particular in the OFF-region. Furthermore, the lower I_{OFF} measured after dark recovery has increased significantly the I_{ON}/I_{OFF} of these devices, up to $10^3 \div 10^4$.

The *fully printed p-type OTFTs with silver inkjetted S/D contacts* have shown very low $I_{gs} < 2$ pA at $V_g = -20$ V and small parasitic contact resistance. Mobility μ_{LIN} up to 0.24 cm^{2}V^{-1}s^{-1} and $I_{ON}/I_{OFF} \approx 10^3$ have been measured . The bias stress induced shifts in the transfer characteristics, both in the ON- and OFF-region, have been completely recovered in time. The light stress subthreshold has been recovered after time intervals comparable to the stress time, while the OFF-region recover was slow. The subthreshold voltage of these devices has shifted during bending up to $\Delta V_g \approx 1.6$ V for a 2% of strain. This instability has been completely recovered removing the mechanical stress. The sufficient reliability and reproducibility of these devices have suggested the possibility of implementing integrated circuits.

The *fully printed p-type OTFTs with organic S/D contacts* have provided a good charge injection in the OSC without the use of SAM functionalizations, resulting in improved contact characteristics. These devices have shown a mobility μ_{LIN} up to 0.06 cm^{2}V^{-1}s^{-1}, low $I_{gs} < 20$ pA at $V_g = -20$ V. The subthreshold slope has been measured to be down to 842 mV/dec, while the $I_{ON}/I_{OFF} \approx 10^5$. At the best of the author knowledge, considering the current state of the art, these devices are the best performing fully printed p-channel OTFTs with organic S/D realized with roll to roll compatible techniques and are well comparable with the best ones obtained with inkjet printing techniques. They have shown not yet satisfying stability under bias and light stress, suggesting disposable devices as suitable applications.

The *fully printed n-type OTFTs* realized have shown very low $I_{gs} < 10$ pA at $V_g = 50$ V, subthreshold slope ≈ 4600 mV/dec, $I_{ON}/I_{OFF} \approx 10^6$. These devices have not shown reliable characteristics and the main issue has been identified in the optimization of the OSC/dielectric interface.

With this thesis work it has been possible to obtain high performance fully printed p-type OTFTs, demonstrating the good electrical performances of the films obtained with the refined inks and printing techniques.
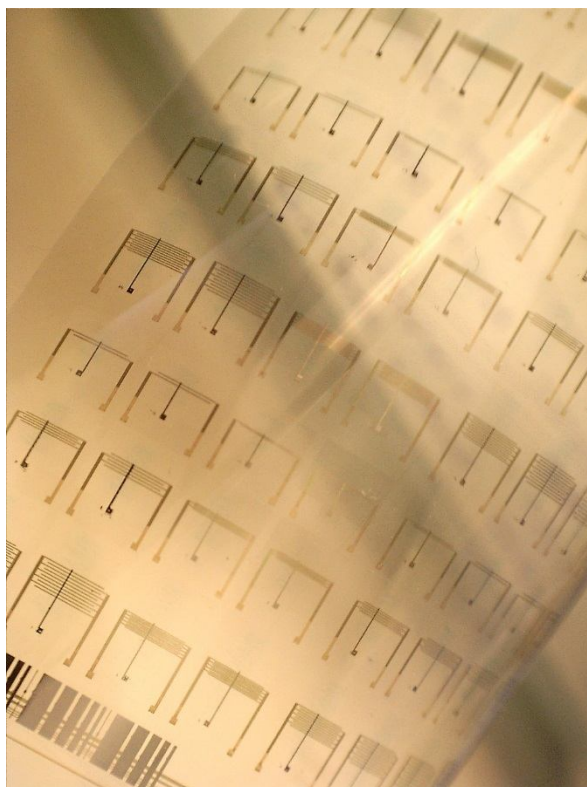
Fig. 2 Sample of fully printed OTFTs.

At last, **inverters** with resistive or active load configuration have been realized and their static and dynamic behaviours have been characterized. As transistors, the fully printed OTFTs with silver inkjetted S/D contacts have been used.

The devices with *external resistive load* have shown interesting features. They have been tested in dynamic until 1 kHz, with supply voltage down to 10 V, still showing a suitable logic swing and stable output waveforms. Future perspectives include the integration of a printed resistance on the same substrate, as the results previously obtained with the inkjet printed resistors are compatible with the implementation of this application.

The *fully printed active load* inverters have shown good performance, with regenerative property and gain around 2.2, while applying a supply voltage of -25 V. The fall time has resulted to be the limiting factor for scaling up the operating frequency of the device. Further improvements would be achieved reducing the parasitic capacitances of the OTFTs, optimizing the layout, and defining the most performing coupling of different *W*/*L* OTFTs as drive and load transistors.

Acknowledgments